Development of a High Voltage Top Cell for Silicon Thin-Film Solar Cells

Von der Fakultät für Mathematik und Naturwissenschaften
der Carl von Ossietzky Universität Oldenburg
zur Erlangung des Grades und Titels einer
Doktorin der Naturwissenschaften
(Dr. rer. nat.)
angenommene Dissertation

von
Cordula Walder
geboren am 03.07.1986
in Vechta

angefertigt am
EWE-Forschungszentrum für Energietechnologie e. V., NEXT ENERGY
Carl-von-Ossietzky-Straße 15, 26129 Oldenburg

Oldenburg, 2015

Gutachter:	Prof. Dr. Carsten Agert
Zweitgutachter:	Prof. Dr. Jürgen Parisi

Tag der Disputation: 24. November 2015

Abstract

The development of multijunction solar cells is a promising approach to increase the efficiency of silicon thin-film photovoltaics. Usually hydrogenated amorphous silicon (a-Si:H) is used as the high bandgap top cell absorber. However, there have been reports suggesting the benefit of even higher bandgaps of the top cell absorber than can be reached with a-Si:H.

The objective of this work is to investigate which steps have to be taken to optimise a high bandgap top cell. In order to answer this question, it shall be clarified which maximum top cell bandgap still leads to sufficient cell current. Moreover, the parameters of the deposition process leading to good material quality are investigated. Finally, the question which kind of amorphous silicon alloy is suited best for which layer type shall be answered.

The simulation results of this work predict that, for a triple cell with a maximum top cell absorber thickness of 300 nm, a top cell bandgap of 1.91 eV is required to absorb sufficient current. This bandgap can still be achieved with device-quality a-Si:H by increasing the hydrogen content. For a quadruple cell the maximum top cell bandgap is 2.08 eV according to the simulation. Therefore, the development of a high bandgap amorphous silicon absorber alloy only is of advantage for more than three cell junctions.

A good material quality of high bandgap amorphous silicon alloys is achieved with high hydrogen content and low impurity content of oxygen or carbon. To increase the hydrogen content of a compact material low substrate temperature, high hydrogen dilution, low pressure and low power are required as parameters in the deposition process.

Methane (CH_4), carbon dioxide (CO_2) and nitrous oxide (N_2O) are used as alloying source gases. Intrinsic amorphous silicon carbide layers (i-a-SiC:H) produced with CH_4 show better single layer and cell properties than intrinsic amorphous silicon oxide layers (i-a-SiO:H) produced with CO_2. N_2O leads to worse absorber layer quality than both CO_2 and CH_4. A gas mix with a high ratio of CH_4 and a low ratio of CO_2 does not improve the absorber layer quality compared to using only CH_4. Employing CH_4 in the i-layer, a single cell open circuit voltage of 1 V is achieved.

In order to increase the bandgap of the p-doped layer CO_2 or CH_4 is added to the process gases. Since the activation energy of p-layers produced with CO_2 is higher than when CH_4 is used at equivalent bandgaps, the single cell open circuit voltage is also enhanced in the former case. The fill factor is not negatively influenced by the higher activation

energy. Consequently, CO_2 leads to higher cell efficiency than CH_4 when used in the p-doped layer. Yet, CH_4 might outperform CO_2 if the p-layer bandgap can be raised further with a higher CH_4 flow ratio, so the activation energy as well as the transparency are enhanced.

In summary, the optimum top cell absorber for a quadruple stack should have a bandgap of 2.08 eV and be made of amorphous silicon carbide with high hydrogen and low carbon content. The amorphous p-layer leads to better cell results when produced with CO_2 but has a higher potential if the bandgap can be raised further using only CH_4.

Kurzfassung

Die Entwicklung von Mehrfachsolarzellen ist ein vielversprechender Ansatz, um die Effizienz von Silizium Dünnschichtsolarzellen zu erhöhen. Üblicherweise wird hydrogenisiertes amorphes Silizium (a-Si:H) als Absorber mit hoher Bandlücke in der obersten Zelle verwendet. Allerdings gibt es Veröffentlichungen, die den Einsatz höherer Bandlücken motivieren als sie mit a-Si:H erreicht werden können.

Die Fragestellung dieser Arbeit befasst sich mit den Maßnahmen, die zu einer optimierten obersten Teilzelle führen. Um dieses Problem zu lösen, soll geklärt werden, welche maximale Bandlücke der obersten Teilzelle noch genügend Zellstrom zulässt. Desweiteren wird untersucht, wie die Abscheidungsparameter angepasst werden müssen, um gute Materialqualität zu erhalten. Schließlich wird die Frage behandelt, welche amorphe Siliziumlegierung für welche funktionelle Schicht am besten geeignet ist.

Die Simulationsergebnisse dieser Arbeit besagen, dass, bei einer maximalen Absorberschichtdicke von 300 nm, die Bandlücke der obersten Teilzelle höchstens 1.91 eV betragen darf, um genügend Strom für eine Dreifachzelle zu generieren. Diese Bandlücke kann mit a-Si:H durch Erhöhung des Wasserstoffgehalts erreicht werden, ohne dass die Materialqualität zu stark abnimmt. Für eine Vierfachzelle ergibt sich aus der Simulation eine optimale Bandlücke der obersten Teilzelle von 2.08 eV. Die Entwicklung einer amorphen Silizium Legierung als Absorberschicht mit hoher Bandlücke ist daher erst ab einer Vierfachzelle von Vorteil.

Die Materialqualität von amorphen Siliziumlegierungen mit hoher Bandlücke wird durch einen hohen Wasserstoffgehalt und einen niedrigen Anteil an Sauerstoff oder Kohlenstoff begünstigt. Um den Wasserstoffgehalt ohne Verlust an Materialdichte zu erhöhen, müssen eine niedrige Substrattemperatur, ein hoher Wasserstofffluss, niedriger Druck und niedrige Leistung als Prozessparameter eingestellt werden.

Als Prozessgase für die Legierungen werden Methan (CH_4), Kohlenstoffdioxid (CO_2) und Lachgas (N_2O) verwendet. Intrinsische amorphe Siliziumkarbidschichten (i-a-SiC:H), die mit CH_4 hergestellt wurden, führen zu besseren Einzelschicht- und Zelleigenschaften als intrinsische amorphe Siliziumoxidschichten (i-a-SiO:H), die mit CO_2 prozessiert wurden. N_2O verschlechtert die Materialqualität der Absorberschichten im Vergleich zu CH_4 und CO_2. Ein Gasgemisch mit einem hohen Anteil an CH_4 und einem niedrigen Anteil an CO_2 verbessert die Materialqualität der intrinsischen Schichten nicht im Vergleich zu reinem CH_4. Durch die Legierung der intrinsischen Schicht mit CH_4 wird in dieser Arbeit eine

Leerlaufspannung der Einzelzelle von 1 V erzielt.

Um die Bandlücke der p-Schicht aufzuweiten, wird entweder CO_2 oder CH_4 den Prozessgasen hinzugefügt. Im Gegensatz zu CH_4 erhöht CO_2 die Aktivierungsenergie der p-Schicht. Das führt zu einer erhöhten Leerlaufspannung und Effizienz von Einfachzellen, die mit CO_2 in der p-Schicht prozessiert wurden, da die höhere Aktivierungsenergie den Füllfaktor nicht beeinflusst. Möglicherweise ließen sich mit CH_4 ähnliche oder sogar bessere Ergebnisse erzielen, wenn die Bandlücke der p-Schicht noch weiter erhöht und damit die Aktivierungsenergie sowie die Transparenz gesteigert würden.

Aus den obigen Ergebnissen lässt sich folgern, dass die optimale Absorberschicht der obersten Teilzelle einer Vierfachzelle eine Bandlücke von 2.08 eV haben sollte. Das beste Material für diese Absorberschicht ist amorphes Siliziumkarbid mit hohem Wasserstoffanteil und geringem Kohlenstoffanteil. Amorphes p-dotiertes Siliziumoxid führt zu den besseren Einzelzellergebnissen. Allerdings hat amorphes p-dotiertes Siliziumkarbid das Potential, durch weitere Bandlückenaufweitung diese Ergebnisse zu übertreffen.

List of Abbreviations

C_3^-	Threefold coordinated negatively charged carbon.
O_3^+	Threefold coordinated positively charged oxygen.
N_4^+	Fourfold coordinated positively charged nitrogen.
H_2	Hydrogen.
SiH_4	Silane.
CH_4	Methane.
CO_2	Carbon Dioxide.
N_2O	Nitrous Oxide.
B_2H_6	Diborane.
PH_3	Phosphine.
p-a-Si:H	P-doped hydrogenated amorphous silicon. Note that the attribute ”hydrogenated” is often omitted in the long form for better readability.
i-a-Si:H	Intrinsic hydrogenated amorphous silicon.
n-a-Si:H	N-doped hydrogenated amorphous silicon.
p-a-SiC:H	P-doped hydrogenated amorphous silicon carbide. Note that all silicon alloys treated in this work are *not* stoichiometric. For simplicity and better readability this is neither marked in the abbreviations nor in the long form.
i-a-SiC:H	Intrinsic hydrogenated amorphous silicon carbide.
p-a-SiO:H	P-doped hydrogenated amorphous silicon oxide.
i-a-SiO:H	Intrinsic hydrogenated amorphous silicon oxide.

i-a-SiGe:H	Intrinsic hydrogenated amorphous silicon germanium.
p-nc-Si:H	P-doped hydrogenated nanocrystalline silicon.
i-nc-Si:H	Intrinsic hydrogenated nanocrystalline silicon.
n-nc-Si:H	N-doped hydrogenated nanocrystalline silicon.
i-nc-SiGe:H	Intrinsic hydrogenated nanocrystalline silicon germanium.
i-μc-Si:H	Intrinsic hydrogenated microcrystalline silicon.
i-μc-SiGe:H	Intrinsic hydrogenated microcrystalline silicon germanium.
c-Si	Crystalline silicon.
CIGS	Cu(In,Ga)Se_2, copper indium gallium diselenide.
III-V	Mixed crystal system consisting of the elements of the third and fifth main group of the periodic table of the elements like aluminium (Al), gallium (Ga), indium (In), phosphor (P), arsenic (As) and antimony (Sb).
SnO_2:F	Fluorine-doped tin dioxide.
TCO	Transparent Conductive Oxide.
NSG	Nippon Sheet Glass.
p-layer	P-doped layer.
i-layer	Intrinsic layer.
n-layer	N-doped layer.
RF-PECVD	Radio frequency plasma enhanced chemical vapour deposition.
UV-VIS-NIR	Ultraviolet-visible-near-infrared.
CPM	Constant photocurrent method.
FTIR	Fourier transform infrared spectroscopy.
EBS	Elastic backscattering spectrometry.
IV	Current-voltage.

EQE	External quantum efficiency.
TMM	Transfer matrix method.
AM1.5G	Air mass 1.5 global.
η	Efficiency.
V_{OC}	Open circuit voltage.
FF	Fill factor.
J_{SC}	Short circuit current.
R_S	Series resistance.
R_P	Parallel resistance.
VB	Valence band.
CB	Conduction band.
E_{Tauc}	Optical bandgap energy according to Tauc et al. [1].
E_{04}	Energy at which the absorption coefficient equals $10^{-4}\,\mathrm{cm}^{-1}$.
E_U	Urbach energy.
E_a	Activation energy.
σ_0	Conductivity prefactor.
ms	Microstructure factor.
ADF	Angular distribution function.
d_{el}	Electrode distance.
T_{heater}	Heater temperature.

List of Figures

List of Tables

Contents

1

Introduction

On the way to a sustainable energy supply the combination of several technologies such as photovoltaics, wind turbines, energy storage, fuel cells and smart grids is essential. But even within one technology like photovoltaics several technological concepts may take their own important part. Silicon thin-film photovoltaics is one of these concepts.

This technology has the advantage of silicon being a non toxic abundant absorber material. The attribute "thin-film" allows for low material consumption and production time. Unlike crystalline silicon solar cells, which are most commonly installed [2], silicon thin-film solar cells do not have to be grown from the melt ($\sim 1400\,^\circ\mathrm{C}$) but can be deposited from the gas phase at quite low temperatures ($\sim 220\,^\circ\mathrm{C}$). This enables the choice of different and even flexible substrates, which can be processed quickly and cheaply from roll to roll. Due to the variety of possible substrates, silicon thin-film solar cells qualify for the integration into products like glass faces of buildings, semi-transparent windows, tiles and portable power sources. The use of the silicon thin-film technology in pocket calculators for example has become quite common. Silicon thin-film photovoltaics can also contribute to power generation. Especially in hot areas this technology may be profitable since its temperature stability is better than that of crystalline silicon solar cells [2].

Unfortunately, the highest cell conversion efficiency of the silicon thin-film technology achieved so far (13.6 % [3]) is about only half as much as what can be gained with a crystalline silicon cell (25.6 % [4]). Since area related system installation costs are independent of the module prize, they can only be compensated by cell efficiency. Consequently, the enhancement of cell efficiency is an important research topic of the silicon thin-film technology.

One promising approach to enhance the efficiency of silicon thin-film solar cells is the development of multijunction devices. Figure 1.1a shows the AM1.5G solar spectrum

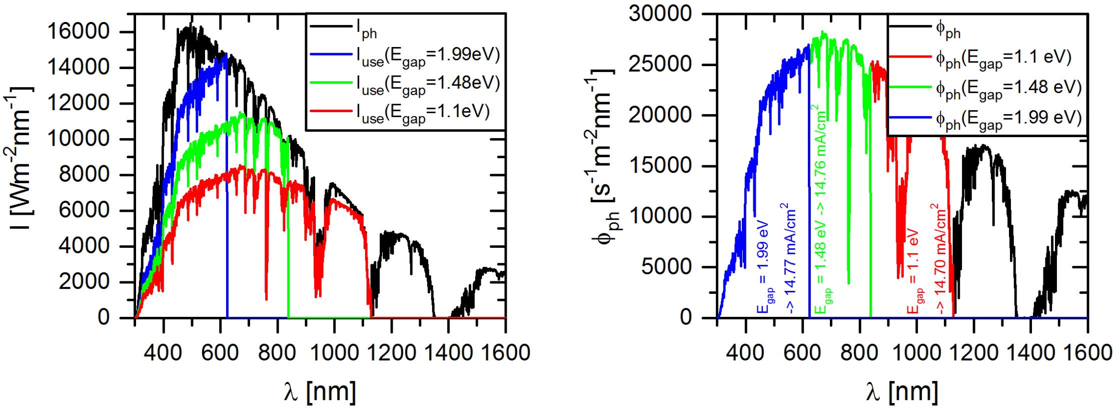

(a) AM1.5G spectral solar intensity from [5]. **(b)** Photon flux density calculated from (a).

Figure 1.1: AM1.5G solar spectrum from [5] and photon flux density. The ideal usable parts of the solar intensity and photon flux density for semiconductors with three different bandgaps.

published by NREL [5] and the maximal usable parts for three different semiconductor bandgaps. Considering the bandgap of microcrystalline silicon (red curve), photons with energies below 1.1 eV or with wavelengths above 1127 nm will not be absorbed. The solar light intensity at higher energies or lower wavelengths cannot be fully exploited because of thermalization losses. Consequently, any absorber material works most effectively at photon energies matching its bandgap. Thus, connecting several single cells with different absorber layer bandgaps in series to form one multijunction cell has the potential to raise the cell efficiency considerably. This is achieved by the reduction of thermalization losses, which becomes evident in increased cell voltage. Figure 1.1a demonstrates, how the combination of the usable spectral parts for several absorber layer bandgaps (coloured curves) almost fills the area of the complete spectrum (black curve). This clearly shows the benefit of a multijunction cell.

Several authors have calculated optimal bandgap combinations for different multijunction cell configurations [6–8]. Interestingly, the optimal bandgap combination is mainly influenced by the requirement of current matching. The current of a multijunction cell is more or less determined by the lowest contribution of any subcell. That is why a loss of total cell current means an effective loss of current in all subcells. Consequently, current matching is very important for a multijunction cell.

Figure 1.1b shows the photon flux density of the adjacent solar spectrum. In order to achieve current matching in a triple cell, the spectral photon flux density should be divided into three parts with equal integrated current values. Choosing a bottom cell bandgap of 1.1 eV like Yunaz et al. [8], the remaining divisions of the photon flux density occur at wavelengths corresponding to bandgap energies of 1.48 eV and 1.99 eV (see figure 1.1b). These bandgap energies are very close to the optimal bandgap combination simulated by Yunaz et al. with the help of a virtual layer stack [8], although neither reflection losses, nor parasitic absorption, defect recombination or realistic absorption edges were considered.

A typical bandgap of amorphous silicon (a-Si:H) is 1.75 eV and of microcrystalline silicon (μc-Si) 1.1 eV [2]. In order to achieve the optimal bandgaps for a triple configuration, amorphous silicon can be alloyed with germanium to reduce the bandgap or with carbon, oxygen as well as hydrogen to increase the bandgap. The previous considerations suggest that for the development of a multijunction cell with more than two subcells a top cell absorber is required whose bandgap exceeds the value of typical a-Si:H.

High bandgap amorphous silicon alloys have already been investigated by many research groups [9–15]. Adding impurities like carbon, oxygen or nitrogen to a-Si:H increases the bandgap energy, lowers the absorption and deteriorates the electrical quality of the films [9–12, 14]. Nevertheless, material with high quality can be achieved if only small amounts of oxygen or carbon are added to a-Si:H [14, 15]. Therefore, high bandgap amorphous silicon alloys have successfully been applied as absorber materials in single and multijunction solar cells [13–20].

The light induced degradation of single cells with a-SiO:H or a-SiC-H absorber layers (E_{gap} = 1.87 to 1.9 eV) is comparable to the case in which a-Si:H is used [17, 21]. The temperature stability of a-SiO:H absorbers is even better compared to a-Si:H [13, 18]. Inthisang et al. [13] achieved a single cell open circuit voltage of 1.062 V with an a-SiO:H absorber at a bandgap of 1.9 eV. This is the highest single cell open circuit voltage reported so far [14]. Si et al. [19] developed a quadruple cell with i-a-SiO:H as the top cell absorbing layer. The resulting cell efficiency amounts to 11.4 % at an open circuit voltage of 2.82 V.

Although a-SiO:H and a-SiC:H have been tested in several multijunction cell configurations [13, 16–19], the recent record of 13.60 % stabilized cell efficiency is still held with an a-Si:H/μc-Si:H/μc-Si:H triple cell [3]. Consequently, the objective of this work is to answer the following open questions and determine the essential factors for the development of an optimised top cell:

1. What is the benefit of a high bandgap amorphous silicon absorber alloy compared to a-Si:H? Which maximum top cell absorber layer bandgap still leads to sufficient current in a triple or quadruple cell configuration?

2. How do the parameters of the RF-PECVD process have to be modified to optimise

the material quality of high bandgap amorphous silicon alloys?

3. When methane (CH_4) is used for the introduction of carbon and carbon dioxide (CO_2) or nitrous oxide (N_2O) for the introduction of oxygen at the same RF-PECVD setup under similar conditions, which type of source gas is suited best for which functional layer and why?

In order to answer these questions, the thesis is laid out in the following way. Firstly, the various employed methods concerning layer deposition, sample analysis and simulation are presented. Then, three main chapters deal with the questions of this work formulated above. In chapter 3, the simulated optimum top cell bandgaps of a triple and a quadruple cell are discussed together with the corresponding cell efficiencies. Chapter 4 presents the trends of the process parameters leading to good material quality of high bandgap amorphous silicon alloys. In chapter 5, single layer and cell properties of samples prepared with N_2O, CO_2 or CH_4 are compared. Finally, a conclusion and an outlook complete the thesis.

2

Methods

2.1 Layer Deposition by RF-PECVD

All semiconducting layers in this work were produced by radio frequency plasma enhanced chemical vapour deposition (RF-PECVD). A plasma is a gas with outward neutrality, which is partly or completely ionised. During the RF-PECVD process, source gases containing the desired species for deposition are let into an otherwise evacuated chamber. Two opposite planar electrodes in the chamber are supplied with an alternating voltage. The resulting radio frequency (rf) electromagnetic field ignites the source gases to form a plasma. In the plasma, the source gases are dissociated. Many primary and secondary reactions lead to the formation of atoms, molecules, ions and radicals. Some of those are precursors for film growth and reach the substrate placed on one of the electrodes. On the substrate, as well as on all other inner chamber surfaces, layer growth takes place according to material properties and surface physics. For more details on plasma deposition of amorphous silicon see [22].

The advantage of RF-PECVD is that the temperatures of electrons, molecule vibrations and the gas in the plasma are not in thermal equilibrium [22]. Chemical reactions are initiated by "hot" or high energetic electrons while the substrate temperature can be kept quite low around 220 °C. This way, cheap and even flexible but temperature sensitive substrate materials such as plastic, glass, or thin metal foils can be used.

The RF-PECVD setup employed in this work is a six chamber cluster tool of the type CS400PS from VON ARDENNE and FAP. To minimize contamination of the chambers and carry over effects, intrinsic and doped layers are deposited in separate chambers. The chambers are connected by an evacuated transfer chamber so cells can be processed without any break of vacuum. The substrate is placed on the grounded anode while the cathode is connected to the rf-power source via matchbox.

process gas	DE [kJ/mol]	main precursor	reaction	BDE [kJ/mol]
SiH_4	323 [23]	SiH_3	$SiH_4 \longrightarrow SiH_3 + H$	393 [24]
CH_4	416 [23]	CH_3	$CH_4 \longrightarrow CH_3 + H$	431 [24]
CO_2	641 [24]	O	$CO_2 \longrightarrow CO + O$	532.2 [24]
N_2O	556 [24]	O	$N_2O \longrightarrow O + N_2$	167 [24]
		NO	$N_2O \longrightarrow NO + N$	480.7 [24]

Table 2.1: Dissociation energies DE of the used process gases, main precursors, reactions leading to main precursors, bond dissociation energies BDE required for the splitting of process gases into precursors.

Apart from hydrogen, the process gases used for the intrinsic layers in this work are silane (SiH_4), methane (CH_4), carbon dioxide (CO_2) and nitrous oxide (N_2O). The dissociation energies (DE) of these process gases are presented in table 2.1. Possible initial reaction pathways, leading to the main precursors for layer growth, are also shown. Finally, the table presents the bond dissociation energies (BDE) required to break the source gases into precursors. Apparently, the dissociation energy of the source gases rises from silane to methane to nitrous oxide to carbon dioxide. Yet, the presence of highly electronegative oxygen can raise the electron temperature in the plasma leading to more dissociations as well [25, 26].

When different atoms, molecules, ions and radicals reach the substrate they are either adsorbed, desorbed or they help remove other particles from the growing surface. An important factor for the growth of high quality layers is the ratio of surface reaction rate and deposition rate. According to Hishikawa et al. [27], there is a competition between the two. Whenever the surface reaction rate dominates, structural relaxations are induced before layer growth takes place. When the deposition rate wins out, the network at the surface has less time to relax, which results in more void formation and poorer material quality [27].

The deposition rate can be reduced by lowering power and pressure as well as by raising the total gas flow rate and hydrogen dilution. Lower power leads to a lower electron temperature and consequently to less decompositions and reduced growth rate [22]. Lower pressure reduces molecule collisions as well as decompositions and thereby the growth rate [2]. High power and low pressure each promote ion bombardment of the growing film [28], which is desirable in the case of amorphous germanium, where it enhances the surface mobility of growth precursors [29]. However, ion bombardment can also shoot

	p-a-Si:H	i-a-Si:H	n-a-Si:H
$\Phi(H_2)$ [sccm]	80	200	200
$\Phi(SiH_4)$ [sccm]	40	40	40
$\Phi(B_2H_6)$ [sccm]	32		
$\Phi(PH_3)$ [sccm]			25
P [W]	10	10	15
p [mbar]	0.3	1	1
d_{el} [mm]	25	15	20
T_{heater} [°C]	220	220	220

Table 2.2: Deposition parameters of standard reference layers.

defects into the material, so it turns out to be mostly detrimental for amorphous silicon and its alloys [14].

Increased total gas flow rate means less residence time for the particles to react and stick to the substrate, which decreases the growth rate of the film [2]. Hydrogen dilution also reduces the growth rate by etching weak bonds and shielding the surface from growth precursors. Moreover, hydrogen incorporation has the benefit of passivating defects and relaxing the network.

The surface reaction rate can be enhanced by increasing the substrate temperature and thereby the surface mobility of the species [27]. Unfortunately, a higher substrate temperature leads to the desorption of hydrogen, so that its positive effects are annihilated. Consequently, a low substrate temperature is required for a high hydrogen content [30].

Several different substrates were used in this work for different samples and characterization techniques. In the case of single layers, commercial flat Schott Eco glass and monocrystalline silicon wafer pieces were employed. The waver pieces were polished on both sides to enable infrared transmission measurements. Solar cells were deposited on commercial Asahi VU and NSG (Nippon Sheet Glass). Both substrates are made of rough SnO_2:F TCO deposited on a glass layer.

The RF-PECVD setup at NEXT ENERGY works at a radiofrequency of 13.57 MHz. The remaining deposition parameters for the standard doped and intrinsic amorphous silicon layers are presented in table 2.2. Table 2.3 shows the deposition parameters for the best high bandgap amorphous silicon alloys developed in this work.

	p-a-SiO:H	i-a-SiO:H	i-a-SiC:H
$\Phi(H_2)$ [sccm]	200	900	900
$\Phi(SiH_4)$ [sccm]	25	30	30
$\Phi(CO_2)$ [sccm]	50	3-20	
$\Phi(CH_4)$ [sccm]			7-30
$\Phi(B_2H_6)$ [sccm]	32		
P [W]	10	10	10
p [mbar]	0.3	1	1
d_{el} [mm]	25	15	15
T_{heater} [°C]	220	180	180

Table 2.3: Deposition parameters of high bandgap materials produced in this work.

2.2 Single Layer Characterization Methods

2.2.1 Optical Spectrometry

2.2.1.1 UV-VIS Spectrometry

In this work, the UV-VIS-NIR spectrometer Cary 5000 from Varian was used for reflectance and transmittance measurements. It covers a wavelength range from 200 to 2500 nm. A monochromator unit splits the overall light intensity into a wavelength dependent spectrum. The sample is placed either in front of an integrating sphere for transmittance measurements, or at the back for reflectance measurements. This way, most of the light interacting with the sample is collected by the sphere and transferred to the detectors.

If multiple reflections are neglected, the absorption coefficient α of a sample with thickness d can be calculated from reflectance (R) and transmittance (T) data as follows:

$$\alpha = -\frac{1}{d}\, ln\left(\frac{T}{1-R}\right). \tag{2.1}$$

According to the Tauc relation [1] the absorption coefficient is connected to the optical bandgap energy E_{Tauc} in the following way:

$$\sqrt{\alpha E} = B\,(E - E_{Tauc}). \tag{2.2}$$

The Tauc slope parameter B indicates how steep the absorption coefficient rises with energy. It should be high ($\sim 1000\,(\mathrm{eV\,cm})^{-1/2}$) for good material quality and is connected to the product of the oscillator strength of the optical transition, the deformation potential and atomic disorder [31].

2.2.1.2 Ellipsometry

Ellipsometry is a valuable tool to obtain information about nk-data, optical bandgap energy, layer thickness, roughness and even density of a material. At NEXT ENERGY the SENTECH SE850 spectroscopic ellipsometer with a wavelength range from 280 to 2500 nm is used.

Linearly polarised light hits the sample, is reflected and changes its polarization to elliptic according to the sample properties. The fractions of the elliptically polarised light parallel (p) and vertical (s) to the sample surface are analysed. The measurement output gained this way are the ratio of the amplitudes of p- and s-polarised light as well as the phase shift between p- and s-polarised waves (for more details see [32]).

It is not possible to relate this data directly to the physical properties of the sample. Therefore, computer modelling of a virtual layer stack with dielectric function models for each unknown material is required. Thus, the measured ellipsometry data is fitted with the model and the desired physical properties are calculated from the fit parameters. In this work, the software SCOUT/CODE by W. Theiss Hard- and Software was used to do the modelling. It calculates the light distribution in the layer stack by the transfer matrix method so that even multiple reflections are considered. In order to fit the spectral ellipsometry data, the OJL-model as described in [33, 34] and the Kramers-Kronig-relation were employed as dielectric function models.

2.2.1.3 Constant Photocurrent Method

Next to Photothermal Deflection Spectroscopy (PDS) and Fourier Transform Photocurrent Spectroscopy (FTPS) the Constant Photocurrent Method (CPM) is a common technique to measure sub-bandgap absorption which is related to disorder and defects in amorphous semiconductors [2]. CPM measurements were conducted at the Fraunhofer ISE Laboratory- and Servicecenter Gelsenkirchen with a self-made setup. Single layers were deposited on Schott Eco glass and evaporated with coplanar aluminium pads of

1 cm length and 1 mm gap in between.

For the measurement, the sample is placed in the dark and the aluminium contacts are supplied with a high constant voltage of about U = 1000 V, depending on the conductivity of the sample. A monochromator splits the light of the halogen lamp into a spectrum and the gap between the aluminium pads on the sample is illuminated step by step with wavelengths from 1400 to 420 nm. The lamp power supply is controlled so that the photocurrent measured between the aluminium pads remains constant. If this condition is fulfilled, the absorption coefficient of the sample is inversely proportional to the photonflux $\Phi(\lambda)$ which is related to the adjusted lamp power:

$$\alpha(\lambda) \sim \Phi^{-1}(\lambda). \tag{2.3}$$

CPM is no absolute measurement technique because the measurement output is just proportional to $\alpha(\lambda)$. Consequently, the measurement results have to be calibrated with the absorption coefficient at the bandgap energy determined from UV-VIS measurements of the same sample. More information about CPM can be found in [35].

The output parameters of CPM measurements are the deep defect density and the Urbach energy E_U, which is a measure for atomic disorder. Both quantities can be deduced from the absorption coefficient at energies below the bandgap energy. The Urbach energy E_U results from the exponential decay of the absorption coefficient at energies just below the mobility gap of the amorphous semiconductor:

$$\alpha(E) \sim exp\left(\frac{E}{E_U}\right). \tag{2.4}$$

There are several methods to determine the absolute deep defect density from the absorption coefficient at very low energies [36, 37]. In this work, the absorption coefficient at the energy E = 1.2 eV is taken as a relative measure for the deep defect density of the samples.

2.2.1.4 Fourier Transform Infrared Spectroscopy

Fourier Transform Infrared Spectroscopy (FTIR) measures the transmittance in the infrared wavelength regime where electromagnetic waves interact with molecule vibrations. In this work, the FTIR spectrometer Spectrum 400 from Perkin Elmer was used for wave numbers between 400 and 7000 cm^{-1}. The advantage of the Fourier transformation technique is the measurement of the complete spectrum at once with the help of

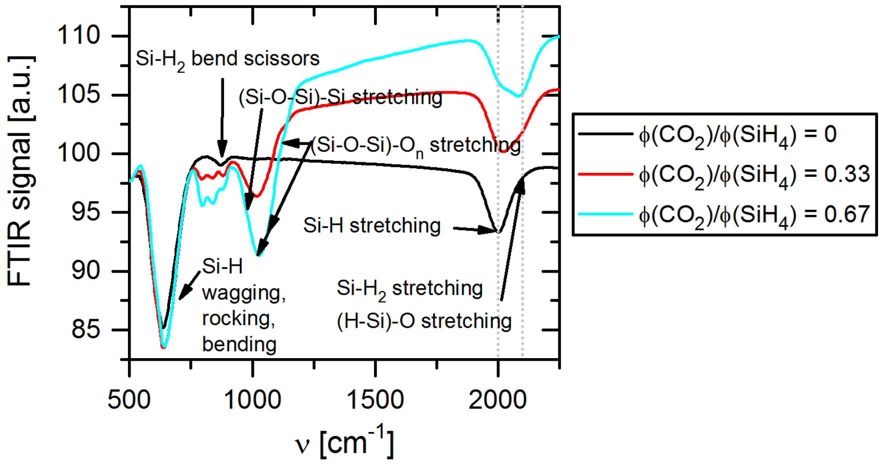

Figure 2.1: FTIR spectra of i-a-SiO:H single layers produced at different ratios of CO_2 with silane.

an integrating Michelson's interferometer. Most glasses are not suitable as substrates for FTIR spectroscopy because they are not transparent in the infrared spectral regime. Thus, monocrystalline silicon wafer pieces polished on both sides were chosen instead.

Figure 2.1 presents the FTIR transmission spectra of i-a-SiO:H single layers produced at different ratios of CO_2 with silane. Black arrows indicate several dips in the spectra which are caused by the light absorption of many unique vibrational modes. The position and the shape of these dips depend on the kind of atomic species and bonds involved, on the kind of bonding environment and bond angle distribution, as well as on the kind of the vibration itself. The transmission dips are often superimposed, as demonstrated by the hydrogen stretching modes around $\nu = 2000\,\text{cm}^{-1}$ in figure 2.1. Therefore, the software SCOUT/CODE by W. Theiss Hard- and Software was used to deconvolute the spectrum, calculate the absorption coefficient and analyse the area, shape and position of each peak. The dielectric function model utilised for the fit procedure was a dielectric background combined with a series of Kim-Oscillators for the description of all the different peaks [34].

Very prominent modes in a-Si:H and its alloys are the wagging, bending and rocking hydrogen modes around the wave number $\nu = 640\,\text{cm}^{-1}$ as well as the stretching hydrogen modes around the wave number $\nu = 2000\,\text{cm}^{-1}$ [38] (see figure 2.1). These modes are used to assess the hydrogen concentration in the film by multiplication of the integrated peak absorption coefficient with a proportionality factor. The proportionality factor is obtained by calibration with samples of known hydrogen content [39, 40]. In analogy to this procedure, the oxygen concentration of a sample can be determined from the oxygen stretching vibrations around the wave number $\nu = 1000\,\text{cm}^{-1}$ [40] (see

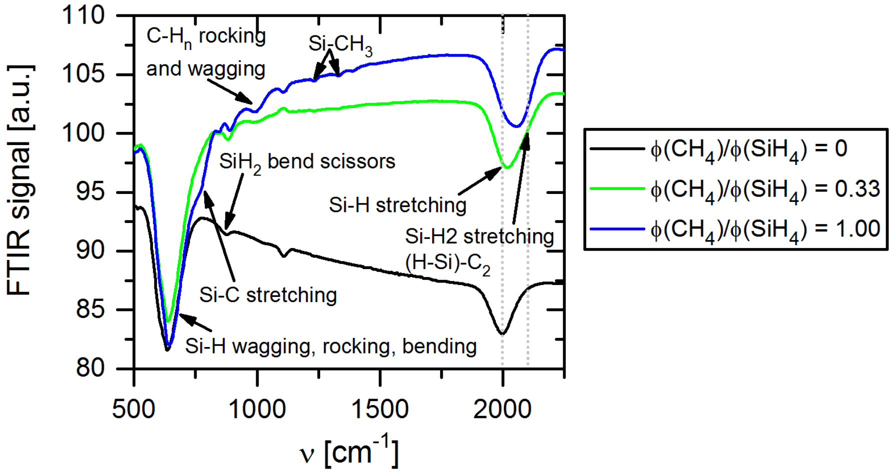

Figure 2.2: FTIR spectra of i-a-SiC:H single layers produced at different ratios of CH_4 with silane.

figure 2.1). The Si-C stretching vibration in silicon carbide interferes with the hydrogen modes around $\nu = 640\,\mathrm{cm}^{-1}$ (see figure 2.2). This makes the determination of the carbon and hydrogen concentrations from the modes near this wave number difficult. Consequently, the hydrogen concentration was calculated from all hydrogen stretching vibrations around $\nu = 2000\,\mathrm{cm}^{-1}$. In summary, the hydrogen and oxygen concentrations (conc.(H), conc.(O)) both were determined from the respective stretching modes according to the relations given by Lucovsky et al. [40]:

$$\text{conc.(H)} = 0.77\frac{at.\%}{eV\ cm^{-1}}\int \alpha dE \tag{2.5}$$

$$\text{conc.(O)} = 0.156\frac{at.\%}{eV\ cm^{-1}}\int \alpha dE \tag{2.6}$$

The proportionality factors for the calculation of the hydrogen concentration are usually obtained from pristine a-Si:H. However, if the bond angles or lengths in the material change, and especially, if different alloy atoms are backbonded to the vibrating bond, the related absorption peak changes its shape and position (see Si-H stretching modes in figures 2.1 and 2.2). Consequently, the determination of different atomic concentrations with proportionality factors from literature is highly inaccurate, especially for amorphous silicon alloys.

FTIR spectroscopy is also commonly used to analyse the microstructure of amorphous silicon and its alloys. Material quality is closely related to film density. If voids or vacancies are formed in the layer, the Urbach energy increases, photoconductivity decreases and light induced degradation is enhanced [41–43]. At the internal surfaces of voids or vacancies several hydrogen atoms bond to the same silicon atom so that clustering of hydrogen takes place. Therefore, polyhydrogen bonds indicate void formation in the material. If one or more hydrogen atoms bond to a silicon atom at a void surface, their stretching vibration modes form at higher wave numbers around $\nu = 2100\,\mathrm{cm}^{-1}$ [38, 44] (see grey dotted lines in figures 2.1 and 2.2). Based on this knowledge, the microstructure factor ms is defined as the ratio of the integrated intensities of the absorption peak around $\nu = 2100\,\mathrm{cm}^{-1}$ and all absorption peaks related to hydrogen stretching modes [2]:

$$\mathrm{ms} = \frac{I_{2100}}{I_{2000} + I_{2100}}. \tag{2.7}$$

As demonstrated in figures 2.1 and 2.2, backbonding effects of oxygen and carbon can shift the monohydrogen modes to higher wave numbers and confuse them with the polyhydrogen modes. This makes the determination of the microstructure factor difficult for amorphous silicon alloys.

2.2.2 Conductivity

Conductivity measurements were performed at the Fraunhofer ISE Laboratory- and Servicecenter Gelsenkirchen. The sample geometry is the same as for CPM measurements. In order to obtain the dark conductivity, the sample is placed in a dark evacuated chamber and annealed for half an hour at about 160 °C. After this step, the heater is switched off and the sample cools down again to room temperature. During the cooling period, a voltage of U = 110 V is supplied to the sample and the corresponding current is measured. The temperature dependent dark conductivity $\sigma_d(T)$ is calculated from the measured resistance and the sample geometry:

$$\sigma_d(T) = \frac{g}{l\,d}\,\frac{I(T)}{U} = \frac{g}{l\,d\,R(T)}. \tag{2.8}$$

Here, d is the layer thickness, l the length of the electrodes and g the gap width in between. For conduction in the extended states the dark conductivity is expected to show an exponential behaviour with temperature [2, 45]:

$$\sigma_d(T) = \sigma_0\, exp\left(-\frac{E_a}{k_B\,T}\right). \tag{2.9}$$

σ_0 is called conductivity prefactor and E_a is the activation energy, which is the difference between the Fermi level energy and the energy of the nearest conduction path. The activation energy and the conductivity prefactor can be temperature dependent, which makes their interpretation difficult.

Photoconductivity is measured at room temperature on air. For this purpose each sample is illuminated with an AM1.5G spectrum and the current voltage characteristic is recorded. Since the photocurrent of good quality semiconductor samples is higher by orders of magnitude compared to the dark current, the samples do not have to be placed in vacuum during measurement.

2.2.3 Elastic Backscattering Spectrometry

Elastic Backscattering Spectrometry (EBS) was conducted at the Institut für Festkörperphysik of the Friedrich-Schiller-Universität Jena in order to obtain the relative oxygen and carbon concentrations of the samples. The measurement setup is depicted in figure 2.3a. The amorphous silicon oxide or carbide sample was deposited on a monocrystalline silicon wafer substrate polished on both sides just like for the FTIR measurements.

During the EBS measurement the sample is bombarded with positively charged helium ions of known energy. When the ions hit the sample, they are scattered and reflected at the atom cores. The deeper the ions penetrate the sample before hitting an atom core, the more their initial energy is reduced by the stopping force of the electrons. After interacting with the sample, the helium ions leave at a certain angle and energy, which is characteristic for the atom type and depth of their collision partner. A silicon detector counts the number of reflected positive charges arriving in different energy intervals. A more detailed description is given in [46].

One example of two resulting spectra is shown in figure 2.3. The measurement output is the yield of the reflected helium ions arriving at different energy channel positions. The blue spectrum belongs to a reference sample for the determination of the oxygen content. The sample consists of 1 µm thick thermal stoichiometric silicon dioxide on a monocrystalline silicon substrate. If one reads the spectrum from right to left, the first step indicates the interaction of helium ions with silicon on the layer surface whereas the second step stands for scattering from silicon atoms on the substrate surface. The following big peak is an enhancement of the interaction with oxygen in the sample at a certain depth. The downwards step signals the end of the interaction with oxygen at the back of the sample layer.

By subtracting the silicon background yields the enhanced oxygen yields of the SiO_2 reference and the sample to be measured (red spectrum) are obtained. Since the oxygen

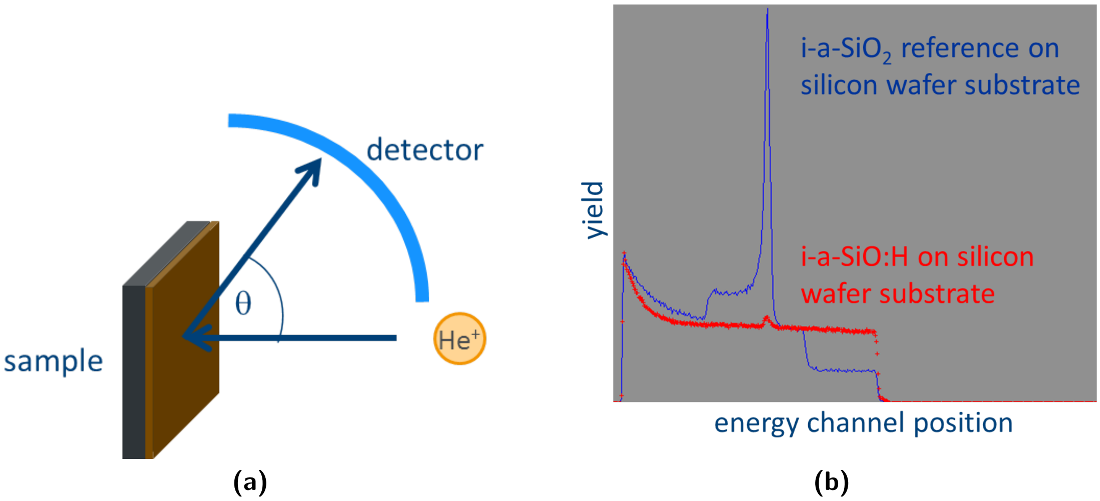

Figure 2.3: (a) EBS measurement setup and (b) Example of EBS spectra.

content of the reference is known, the oxygen content of the sample can be deduced by comparison of the two different oxygen yields. The procedure for the determination of the carbon content works similarly, only with pure glassy carbon as a reference, so no silicon background has to be subtracted.

Elastic Backscattering Spectrometry (EBS) is comparable to Rutherford Backscattering Spectrometry (RBS). Since the oxygen and carbon concentrations to be measured were really small in the range of 1 to 8 at%, the oxygen and carbon yields delivered by RBS would not have been distinguishable from the noise. Therefore, Elastic Backscattering Spectrometry was used where the initial ion energies were increased to 3035 keV for oxygen and to 5700 keV for carbon. As a consequence, the scattering cross sections of the once or twice positively charged helium ions on ^{16}O or ^{12}C were enhanced by a factor of more than 20 for oxygen or 120 for carbon at a certain depth in the sample. This leads to the position and increased height of the oxygen peaks in figure 2.3, so even small oxygen concentrations could be determined.

2.3 Cell Characterization Methods

2.3.1 Current Voltage Characteristic

Illuminated current-voltage characteristic (IV) measurements of solar cells were performed with a triple A WACOM dual lamp solar simulator. The measurement setup (see figure 2.4) includes a halogen lamp and a xenon lamp to cover the solar spectrum of

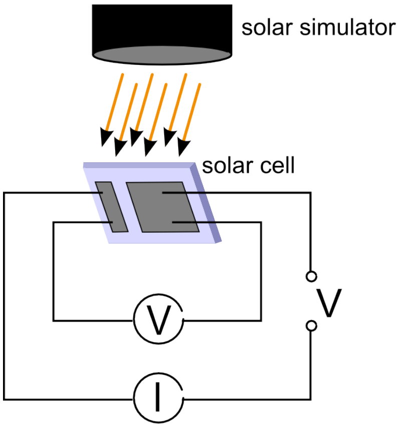

Figure 2.4: Sketch of the IV measurement principle.

interest. In order to produce an AM1.5G solar spectrum at $1000\,\mathrm{W/cm^2}$, the optics of the solar simulator is adjusted. The solar cell sample is placed on a measurement block with a temperature control set at 25 °C. The 16 solar cells of one sample are contacted by the four point method from beneath and illuminated from above. Finally, the direct applied voltage is ramped and the corresponding current is measured for each cell. From the resulting current voltage characteristic the cell efficiency, the fill factor, the open circuit voltage, the short circuit current as well as the parallel and series resistance are deduced.

2.3.2 External Quantum Efficiency

The wavelength dependent external quantum efficiency (EQE) was determined from differential spectral response measurements with the SpeQuest setup from RERA SOLUTIONS. The external quantum efficiency is the fraction of impinging photons transformed into charge carriers that contribute to the photocurrent of the solar cell. In the setup, a xenon lamp and a halogen lamp cover the spectrum from UV to visible and infrared. Passing a filter wheel and a chopper, the light beam is split into a spectrum by a monochromator unit before hitting the solar cell. In order to simulate the real conditions under illumination, the single cell is simultaneously illuminated by white bias light from a halogen lamp. The measurement of single cells is performed at the short circuit condition of 0 V bias voltage. The photocurrent collected at the solar cell contacts is transformed by a transimpedance amplifier (TIV) and sent to a lock-in amplifier, which filters the signal of the chopper frequency. This way, only the wavelength dependent signal of very small photocurrents is measured without the signal of the bias light. Before the measurement, the wavelength dependent photocurrent of a reference cell with known spectral response is collected to calibrate the system.

2.4 Simulation

2.4.1 Sentaurus TCAD

The simulation software Sentaurus TCAD from Synopsys is designed for the modelling of semiconductor devices such as transistors , LEDs and solar cells. In this work, Sentaurus TCAD was used for the potential estimation of amorphous high bandgap materials in thin-film silicon solar cells.

The simulation domain consists of a virtual layer stack corresponding to the solar cell to be modelled. The outward surface of each electrode layer is defined as an electrical contact. The complete simulation domain is covered with a discrete mesh and material properties as well as simulation results are saved at each mesh point. Depending on the optical solver, one to three dimensional modelling is possible.

There are several optical solvers available to calculate the light distribution and the absorbed photon density of the device under illumination [47]. The Raytracer uses geometrical optics, considering light scattering but no coherent propagation of light. The one dimensional Transfer-Matrix-Method (TMM) treats light coherently but neglects scattering effects.

In silicon thin-film solar cells, rough front electrodes are commonly used for absorption enhancement by light scattering into the subsequent layers. Yet, the light beam incident on the rough surface does not loose its coherence completely by scattering, so coherent and incoherent light propagation have to be considered by the simulation. The one dimensional Scattering Solver meets this requirement by combining the concepts of Raytracer and TMM according to the semi-coherent optical model presented in [48]. The amount of scattered light at each rough surface is judged from scalar scattering theory [49].

After the optical solver has calculated the absorbed photon density from the given illumination spectrum at each mesh point, the results are transferred or interpolated to the electrical mesh. Based on the optical results, the software solves the Poisson and continuity equations for electrons and holes. Using the drift and diffusion model, the electrical current at the virtual contacts is obtained for different applied voltages, so the current-voltage characteristic of the solar cell can be simulated. Apart from the optical generation rate, the recombination rate by Shockley-Read-Hall recombination is also considered on the basis of capture cross sections for electrons and holes.

2.4.2 CODE

The software SCOUT/CODE by W. Theiss Hard- and Software is a beneficial tool for the optical simulation of materials and devices. It was used in this work for the evaluation of UV-VIS, ellipsometry and FTIR spectra. The light distribution in the designed virtual layer stack is calculated by TMM, so coherence and multiple reflections are taken into account.

First of all, the materials have to be defined by choosing their optical properties. If their dielectric functions are known already, they can be imported by the software, if not, there are several dielectric function models available for description. In this work, a constant dielectric background model was combined with Kim-Oscillators for the evaluation of FTIR spectra. The susceptibility of a Kim-Oscillator is given by a combination of a Gauss and a Lorentz function [34]. In order to evaluate ellipsometry and UV-VIS spectra, the OJL model was used together with the Kramers-Kronig relations.

The OJL model assumes a square root course of the valence and conduction band density of states against energy. Thus, a sharp energy bandgap E_{gap} is formed in the disorderless limit [33, 34]. The edges of the mobility gap are defined slightly above and below the disorderless band edges. Here, the square root course of the density of states turns into an exponential decay given by the tail breadth parameter. In order to obtain the absorption coefficient, the density of states of the valence band is convoluted with the density of states of the conduction band and the result is multiplied with the optical transition matrix element. Finally, the real part of the dielectric function is calculated from the imaginary part with the help of the Kramers-Kronig relations.

In CODE, the OJL model is defined by the following four fit parameters: the disorderless bandgap E_{gap}, the tail breadth parameter γ, the optical transition strength and a decay parameter. The decay parameter ensures that the imaginary part of the dielectric function decreases exponentially at high energies so the Kramers-Kronig relations can be applied [34].

Once the materials involved are defined by known dielectric functions or dielectric function models, they are combined in a layer stack. The desired optical spectra (T/R, ellipsometry, FTIR, absorption,...) are calculated in dependence on the chosen wavelength range. If any measured spectra of unknown materials shall be analysed, they are compared with the calculated spectra. The parameters of the dielectric function models and the layer thicknesses can be used as fit parameters to achieve maximal agreement between the calculated and measured spectra. This way, the optical properties of the unknown materials, defined by models with arbitrary start parameters, are deduced. Next to the capability of fitting measured optical spectra, CODE also allows the simulation of spectra resulting from known materials and layer stacks.

3

Optimal Top Cell Bandgap and Potential Estimation

The motivation for an amorphous high bandgap top cell absorber alloy is the reduction of thermalization losses. Although Sichanugrist et al. [16] showed the feasibility of an a-SiO:H/a-SiGe:H/μc-Si:H triple cell, standard i-a-Si:H still yields better results as the top cell absorber in a similar cell configuration [50, 51]. This provokes the question, what benefit can be expected from a high bandgap amorphous silicon alloy compared to a-Si:H in a triple or quadruple cell. Since experimental results do not show any efficiency gain compared to a-Si:H yet, simulation tools are used to estimate the potential of high bandgap top cell absorber alloys.

Yunaz et al. have simulated the optimal absorber bandgap combination for a silicon thin-film triple cell assuming μc-Si:H to be the material of the bottom cell absorber [8]. Fixing the lowest absorber bandgap at the value of μc-Si:H (1.1 eV) is reasonable, since alloying with germanium cannot reduce the bandgap much further without significant loss of material quality [52, 53]. Yunaz et al. have chosen quite optimistic simulation conditions. They assume no reflection at the front surfaces, no optical losses in the TCO, high mobilities for electrons and holes ($\mu_e = 50\,\mathrm{cm^2\,V^{-1}\,s^{-1}}$, $\mu_h = 10\,\mathrm{cm^2\,V^{-1}\,s^{-1}}$), very low Urbach energies ($E_U(\mathrm{VB}) = 20\,\mathrm{meV}$, $E_U(\mathrm{CB}) = 10\,\mathrm{meV}$) and a midgap defect density of $10^{15}\,\mathrm{cm^{-3}}$ for all intrinsic layers [8]. The absorption coefficient α is calculated in dependence on the bandgap according to Tauc's formula [1, 8].

As a result, the simulation predicts a maximum triple cell efficiency of $\eta = 21.38\,\%$ with $J_{SC} = 11.36\,\mathrm{mA/cm^2}$, $V_{OC} = 2.43\,\mathrm{V}$ and $\mathrm{FF} = 77\,\%$. This is achieved at a top cell bandgap of 2.0 eV and a middle cell bandgap of 1.45 eV [8]. Interestingly, a top cell bandgap of 2.0 eV also results from dividing the AM1.5G solar spectrum between 300 and 1100 nm in three parts with equal integrated photon flux density (see figure 1.1b).

According to the simulation of Yunaz et al., the voltage contribution of the top cell is 1.23 V and the required top cell absorber thickness is only 200 nm [8]. Raising the top cell bandgap from 1.9 eV, which can be achieved with a-Si:H [54], to 2 eV, increases the triple cell efficiency by about 1.0 % in absolute terms [8].

In contrast to Yunaz et al., Isabella et al. present a purely optical simulation of a silicon thin-film quadruple cell containing a-Si:H or a-SiO:H, a-SiGe:H, μc-Si:H and μc-SiGe:H absorber layers [55]. An efficiency estimation is included by assuming a fill factor of 77 % and by adding the open circuit voltage contributions of the sub cells obtained from literature [13, 51, 52, 56]. According to Isabella et al., the optical data for the layer stack is derived from measurements of realistic state of the art material [55]. The nk-data of the antireflective coating and of the glass substrate is constant. Moreover the absorption of the intermediate reflectors and the back reflector consisting of 20 nm n-nc-SiO:H is believed to be negligible. Scattering is presumed to take place at each rough interface following the only 70 nm thick TCO layer. The scattering parameters include a constant haze of one in reflection and transmission as well as a wavelength independent Lambertian angular distribution function (ADF) [55].

The simulation predicts 8.71 mA/cm^2 matching current and 19.57 % quadruple cell efficiency when 130 nm thick a-Si:H with 1.9 eV bandgap is used as the top cell absorber. By changing the top cell absorber to 170 nm thick a-SiO:H with 2 eV bandgap the matching current can be kept and the cell efficiency increases by 0.26 % due to the increased top cell voltage contribution from literature [55].

In summary, when raising the top cell absorber bandgap from 1.9 eV (a-Si:H) to 2 eV (alloy) Yunaz et al. predict an efficiency gain of ca. 1 % in a triple cell [8] and Isabella et al. assume a gain of 0.26 % in a quadruple cell [55].

While Isabella et al. simulate a current of 8.72 mA/cm^2 at 170 nm a-SiO:H thickness, Yunaz et al. require only 30 nm more to increase the current by 2.64 mA/cm^2. Judging from simulations and experimental results, this is an unusually big increase of cell current. Even if the simulated light beam starts in the absorber material with optical data from Isabella et al. ($E_{gap} = 2$ eV) [55], raising the layer thickness from 170 to 200 nm increases the current only by 0.5 mA/cm^2. The resulting simulated current at 200 nm absorber thickness is 10.95 mA/cm^2. Consequently, Yunaz et al. use a very optimistic absorption coefficient for the top cell absorber to generate a current of 11.36 mA/cm^2 with only 200 nm layer thickness. Since Isabella et al. consider reflection losses at front surfaces, parasitic absorption in the TCO and employ nk-data of state of the art materials, their optical model seems to be more reliable. Hence, it is unclear whether an optimised top cell absorber with a bandgap of 2 eV produces sufficient current for a triple cell under realistic conditions and at a reasonable layer thickness. In order to solve this problem, the following questions shall be answered:

1. What does optimal nk-data of a high bandgap amorphous silicon alloy look like?
2. What is the optimal p-layer bandgap in dependence on the i-layer bandgap?
3. What is the maximum reasonable layer thickness of a high quality top cell absorber?
4. What is the optimal short circuit current of a triple or quadruple cell? At which bandgap of the top cell absorber can this current be achieved with a reasonable layer thickness?

3.1 Optimal nk-data in Dependence on the Bandgap

In order to estimate the optimal nk-data of a high bandgap absorber, amorphous silicon oxide and carbide single layers with varying Tauc bandgaps were deposited on Schott Eco glass substrates. The RF-PECVD process parameters of these layers are presented in table 2.3. Reflection, transmission and ellipsometry spectra of the layers were measured and fitted with the software SCOUT/CODE by W. Theiss Hard- and Software according to the procedure described in section 2.4.2. The OJL model [33, 34] was chosen as optical model to calculate the imaginary part of the dielectric function.

The four fit parameters of the OJL model are depicted in figure 3.1 for the amorphous silicon single layers produced either with CH_4 or CO_2 in dependence on the measured Tauc bandgap. The data points around the lowest Tauc bandgap of 1.85 eV represent standard i-a-Si:H layers without carbon or oxygen. The gap energy parameter E_{gap} describes the disorderless limit of the bandgap. In the case of disorder the mobility gap is bigger by around the tail breadth parameter γ [33]. Figure 3.1a shows that the sum of the fitted gap energy parameter and the tail breadth parameter describes the measured Tauc bandgap (black line) quite well. The tail breadth parameter γ in figure 3.1b was fixed at the measured Urbach energy and not fitted. It increases with the Tauc bandgap in the case of CO_2. The optical transition strength is highest for the i-a-Si:H layers and decreases with the Tauc bandgap while the decay parameter shows the opposite behaviour (see figures 3.1c-3.1d).

High quality material is characterised by a low tail breadth parameter, high optical transition strength and a low decay parameter. In this regard, standard a-Si:H at a Tauc bandgap around 1.85 eV exhibits the best performance in figure 3.1. Since the standard i-a-Si:H layers have device quality [57], it is unlikely that any high bandgap

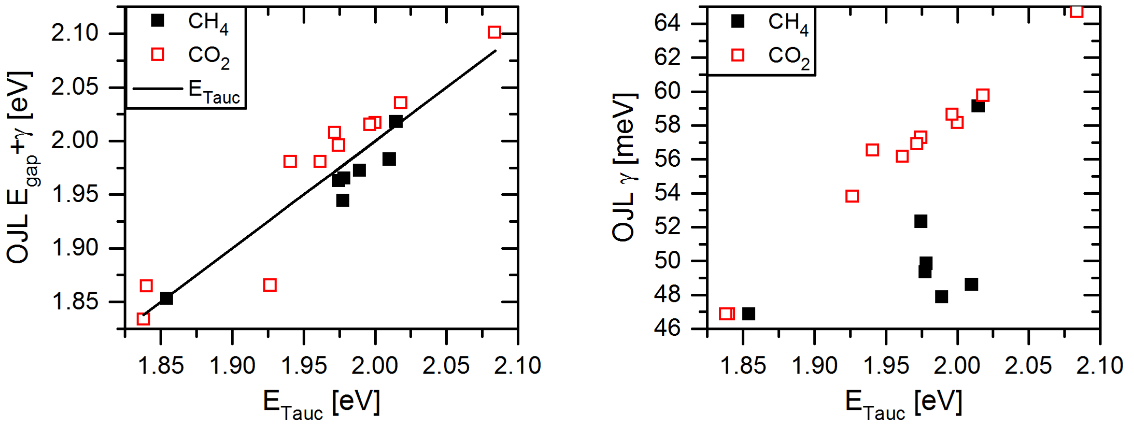

(a) Sum of the disorderless bandgap and the tail breadth parameter.

(b) Tail breadth parameter.

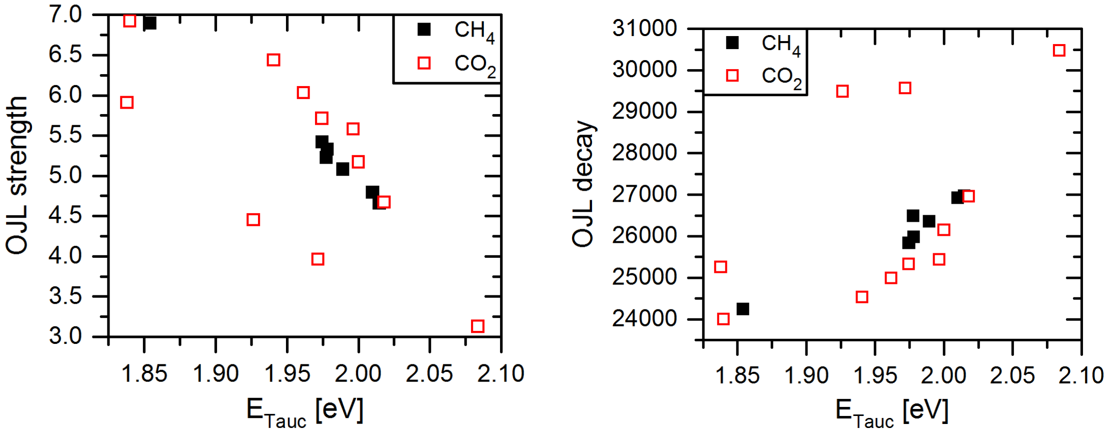

(c) Optical transition strength.

(d) Decay parameter.

Figure 3.1: Fit parameters of the optical data of a-SiO:H and a-SiC:H single layers against measured Tauc bandgap.

alloy shows superior optical properties with respect to the four parameters in figure 3.1. Consequently, the tail breadth parameter, transition strength and decay parameter associated with a-Si:H are chosen as fixed optima and the gap energy parameter is varied to generate optimal optical data for different bandgap energies. The energy gap parameter is adjusted to characterise the nk-data by a certain higher mobility gap E_{mob}. For the generation of optimal nk-data of high bandgap absorber alloys, the model parameters in table 3.1 were used.

The optimised calculated nk-data for two different bandgaps (opt) and one example of nk-data fitted to measured layer results (fitted) are shown in figure 3.2. One might assume

E_{mob} [eV]	γ [meV]	strength	decay
1.70 - 2.10	47	7	24000

Table 3.1: OJL parameters for the generation of optimal nk-data in dependence on the bandgap.

that, by increasing the bandgap, the optimal k data is simply "cut" at the new bandgap energy and that the remaining curve progression remains identical. This is not the case, as can be seen in figure 3.2a. The k data is shifted completely to shorter wavelengths or higher energies with increasing bandgap. In fact, this shift is even documented in the Tauc formula [1]:

$$\sqrt{\alpha E} = B\,(E - E_{Tauc}). \tag{3.1}$$

Consequently, the absorption of the material is reduced at each wavelength for higher bandgap energies. This finding underlines the question whether high bandgap materials can provide enough current for a triple cell.

The optimised n-data in figure 3.2c is shifted downwards and also slightly to lower wavelengths with increasing bandgap. The fitted n-data of the measured absorber layer is even more reduced than the corresponding optimised n-data at the same bandgap. The k-data of the real layer is lower than the optimised counterpart at short wavelengths (see figure 3.2a) but higher in the infrared spectral part due to enhanced Urbach energy (see figure 3.2b).

For different layer positions in the solar cell, the spectral dependence of the optical data has a special relevance. Figure 3.3a shows the simulated absorption of the 200 nm thick intrinsic layer of a single cell for various bandgaps and nk-data. Although the nk-data is quite different, as can be seen in figure 3.2, the simulated absorption curve only reflects this difference from a wavelength of ca. 450 nm onwards. The blue light below this wavelength, which reaches the intrinsic layer, is absorbed within 200 nm for a variety of absorption coefficients. The demarcation wavelength, at which the absorption of the intrinsic layer starts to differ with the optical data, is marked by the red dotted line in figures 3.3a and 3.2 for 200 nm absorber thickness. When the absorber thickness increases, the demarcation wavelength is shifted to higher values, as demonstrated by figure 3.3b.

If the blue spectral part of the k data left of the red dotted line in figure 3.2a is neglected, the difference between the fitted and optimised (opt) k data for a bandgap of 2.00 eV is

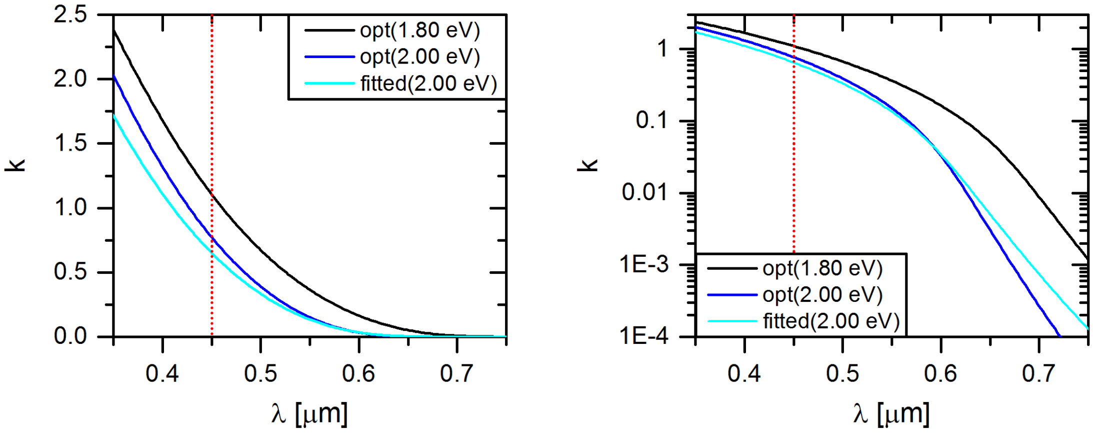

(a) k-data. **(b)** Logarithmic k-data.

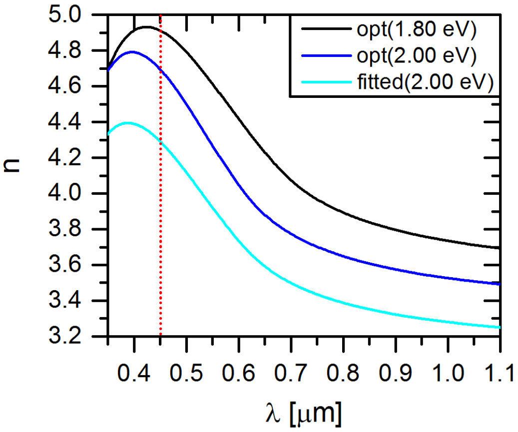

(c) n-data.

Figure 3.2: Optimised (opt) and fitted optical data for different bandgaps.

quite small and leads to very similar absorption curves in figure 3.3a. As a consequence, the red spectral regime of the optical data of absorber layers has a bigger influence than the blue spectral regime. Therefore, the red spectral part should be determined quite precisely. This is difficult, because the UV-VIS and ellipsometry spectra are not very accurate at long wavelengths due to the low absorption of the measured materials. Hence, the tail breadth parameter γ was fixed at the measured Urbach energy and not fitted to determine the optical data described above.

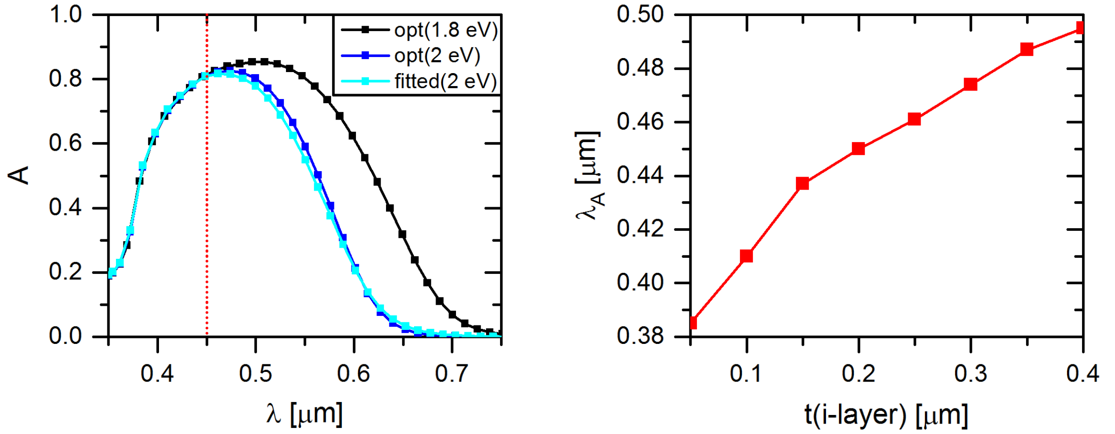

(a) Simulated absorption for different bandgaps and nk-data of the absorbing layer.

(b) Demarcation wavelength, at which the absorption of the intrinsic layer starts to differ with the optical data.

Figure 3.3: Wavelength dependence of the i-layer absorption for different optical data.

3.2 Input Parameters for the Simulation with Sentaurus TCAD

The first question was answered by generating optimal nk-data in dependence on the bandgap. To answer questions 2. - 4. solar cell simulations with Sentaurus TCAD were conducted. The optical problem was solved using the TMM scatter model. This model is a one dimensional optical solver which calculates the semi-coherent light distribution in the cell caused by scattering (see section 2.4.1 and [48]). The electrical solution is gained from the optical generation rate by solving the Poisson and continuity equations for electrons and holes (see section 2.4.1 and [47]).

Figure 3.4 shows a sketch of the layer stack used in the simulation. A half-space of glass ($n = 1.53$) is followed by 70 nm ZnO:Ga, 10 nm p-a-SiC:H, an intrinsic amorphous silicon alloy of varying thickness, 20 nm n-nc-Si:H and 10 nm p-a-SiC:H of the adjacent middle cell. The layer stack is completed with a half-space of i-a-SiGe:H. This way, only the top cell has to be simulated effectively. However, the optical light distribution is close to that of an arbitrary multijunction cell because the i-a-SiGe:H half-space simulates the light transfer to the middle and bottom cells. Reflection at intermediate or back reflectors is neglected by this configuration.

Except for the intrinsic layer, the optical data and thicknesses of the remaining layers and the i-a-SiGe:H half-space were taken from the publication of Isabella et al. [55]. For the intrinsic absorber layer, the optimised and the fitted nk-data from section 3.1 was used. In analogy to Isabella et al. [55], a haze of one in reflection and transmission

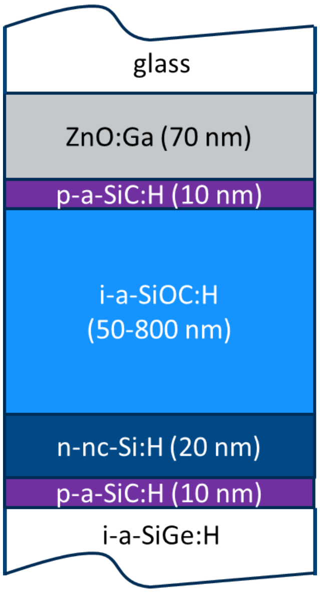

Figure 3.4: Layer stack for the simulation with Sentaurus TCAD.

as well as a wavelength independent Lambertian scattering distribution were attributed to each virtual rough interface following the TCO layer. Electrical contacts were set at the glass/ZnO:Ga and n-nc-Si:H/p-a-SiC:H interfaces. In order to eliminate all electrical influences of the adjacent middle cell, the second p-a-SiC:H layer was defined as a conductor. The electron and hole mobilities in the intrinsic layer were chosen to be 20 and $5\,\mathrm{cm}^2\,\mathrm{V}^{-1}\,\mathrm{s}^{-1}$. The defect distribution was calculated in dependence on the valence band tail parameter γ_V which is set equal to the Urbach energy E_U. According to Orapunt et al., the conduction band tail parameter γ_C results from the following linear relationship with the valence band tail parameter γ_V [58]:

$$\gamma_C = 1.307\,\gamma_V - 40.932\,meV. \tag{3.2}$$

The midgap defect density N_{db} of the intrinsic layer was determined from the Urbach energy E_U using the relation given by Stutzmann et al. [59]:

$$N_{db} = N^*\,E_U\,exp\left\{-\frac{E_{db}-E^*}{E_U}\right\}. \tag{3.3}$$

E_{db} is the demarcation energy, above which the valence band tail states decay spontaneously into dangling bonds [59]. E^* describes the starting energy of the valence band tail.

The energy difference $E_{db} - E^*$ is set to 0.45 eV. $N^* \approx 10^{21}\,\mathrm{cm}^{-3}\,\mathrm{eV}^{-1}$ is the density of states at the starting energy E^* of the valence band tail.

3.3 Optimal p-Layer Bandgap

The motivation for a high bandgap absorber material is the reduction of thermalization losses which shows in a higher open circuit voltage. Yet, the open circuit voltage also strongly depends on the properties and especially on the bandgap of the p-doped layer. The bandgap of the p-doped layer is commonly raised not only to reduce parasitic absorption but also to slow down the extraction of holes at the front contact. The accumulation of holes near the p/i-interface lowers their quasi Fermi level. Consequently the difference of the chemical potentials at the contacts is enhanced, which raises the open circuit voltage. Considering this information, the benefit of a high bandgap intrinsic absorber can only prevail with an optimised p-layer bandgap.

In order to find the optimal p-layer bandgap in dependence on the i-layer bandgap, a combined optical and electrical simulation of the layer stack in figure 3.4 was conducted for varying applied voltages. The intrinsic layer thickness was set to 250 nm and the Urbach energy of the intrinsic layer was chosen to be 50 meV. For several bandgaps of the i-layer the p-layer bandgap was varied. While for each i-layer bandgap the corresponding optimal nk-data was used, the nk-data of the p-layer was kept constant at the values of Isabella et al. [55]. This is justified because the chosen absorption coefficient of the p-layer is quite low. The simulation has shown that in this case the adjustment of the nk-data to the bandgap of the p-layer is not necessary for the determination of the optimal bandgap relation.

The simulation results are depicted in figure 3.5. Figures 3.5a and 3.5b present the open circuit voltage and the fill factor against the p-layer bandgap for i-layer bandgaps of 1.85 and 2.00 eV. As expected, the open circuit voltage rises with the p-layer bandgap for both cases of i-layer bandgaps. After reaching a plateau, the open circuit voltage continues to increase again but the fill factor drops drastically because of the beginning reversal of the diode. Tawada et al. [60] observed the increase of the open circuit voltage with the p-layer bandgap experimentally. They also found that the drop of the fill factor coincides with the saturation of V_{OC} at the plateau.

The optimal p-layer bandgap, which marks the point before the fill factor drops, is indicated by dotted lines in figures 3.5a and 3.5b. Figure 3.5c shows a linear relationship between the optimal p-layer bandgap and the i-layer bandgap. Apparently, the simulated optimal p-layer bandgap is always about 0.25 to 0.3 eV higher than the corresponding

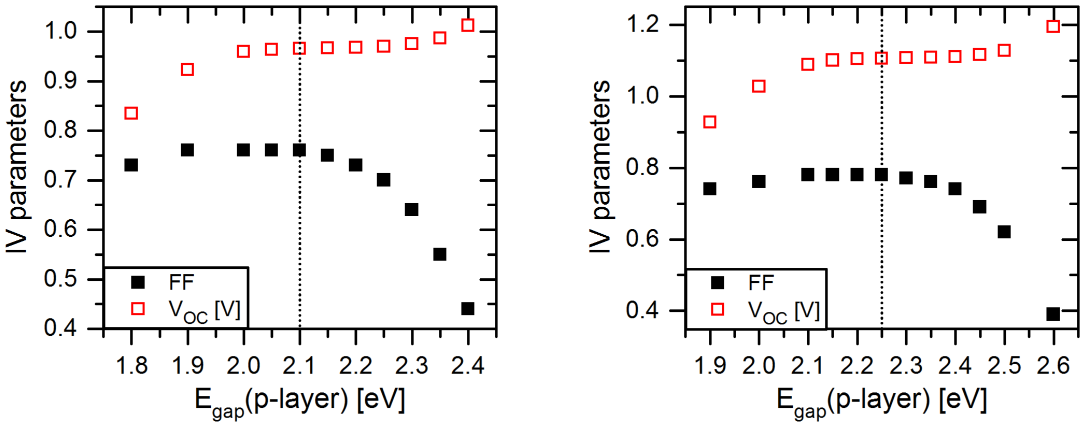

(a) V_{OC} and FF for 1.85 eV i-layer bandgap.

(b) V_{OC} and FF for 2.00 eV i-layer bandgap.

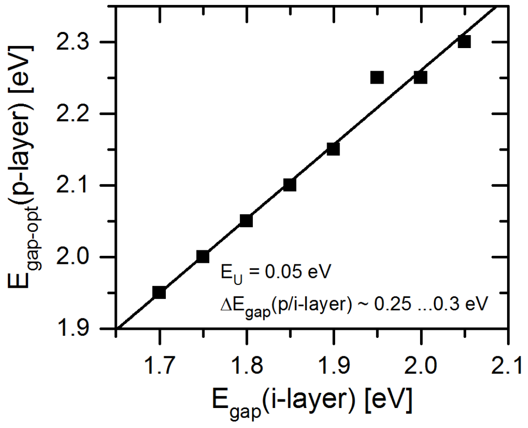

(c) Optimal p-layer bandgap against i-layer bandgap.

Figure 3.5: Simulated V_{OC} and FF for the determination of the optimal p-layer bandgap in dependence on the i-layer bandgap.

i-layer bandgap.

3.4 Maximum Top Cell Absorber Thickness

In order to be superior to standard i-a-Si:H, a high bandgap amorphous silicon alloy has to achieve about the same short circuit current in a multijunction cell. This can only be realised with a higher i-layer thickness because of the lower absorption of high bandgap alloys (see figure 3.2a). The electrical quality of high bandgap alloys is not better than that of a-Si:H. Consequently, there is a limit to the practical absorber thickness given by defect recombination and the reduction of the open circuit voltage. In order to find this limit, the layer stack in figure 3.4 was simulated for several absorber thicknesses. A voltage ramp was applied for each thickness variation. The Urbach energy was kept constant at $E_U = 50\,\mathrm{meV}$ and the simulation was conducted for two different bandgaps of the intrinsic layer with optimal nk-data. The nk-data of the p-layer was taken from Isabella et al. [55] but the p-layer bandgap was set to the optimised values in dependence on the i-layer bandgap.

Figure 3.6 shows the simulated IV parameters against the absorber thickness for two different bandgaps of the i-layer. The open circuit voltage first drops steeply and then more moderately with the i-layer thickness. According to Lambert-Beer's law, this can be explained by the exponential decay of light intensity with penetration depth in the absorber layer. The generated free charge carrier density, responsible for the Fermi level splitting, is high for thin layers, but decreases with the layer thickness like the light intensity. Moreover, defect recombination also reduces the open circuit voltage at high i-layer thicknesses.

Long conduction paths enhance the chances of defect recombination, so the fill factor drops linearly with the absorber layer thickness. Since the defect distribution and quantity are held constant, the open circuit voltage and the fill factor increase when the i-layer bandgap is raised from 1.85 to 2.00 eV. Higher absorber layer bandgaps reduce the probability of charge carrier recombination. Consequently, they lead to an enhanced fill factor at a constant defect distribution.

The short circuit current shows the opposite course with i-layer thickness than the open circuit voltage. Again, this follows from Lambert-Beer's law and increasing defect recombination with i-layer thickness. The short circuit current is constantly higher for the lower i-layer bandgap by almost $3\,\mathrm{mA/cm^2}$ due to superior k-data. This advantage leads to an enhanced cell efficiency for the lower i-layer bandgap by about 0.5 to 0.8 % independent of the i-layer thickness. In order to compensate the difference in the short circuit currents for the two i-layer bandgaps at 300 nm absorber thickness, the difference of the open circuit voltages would have to be 0.238 V. So, the cell with 2.00 eV i-layer

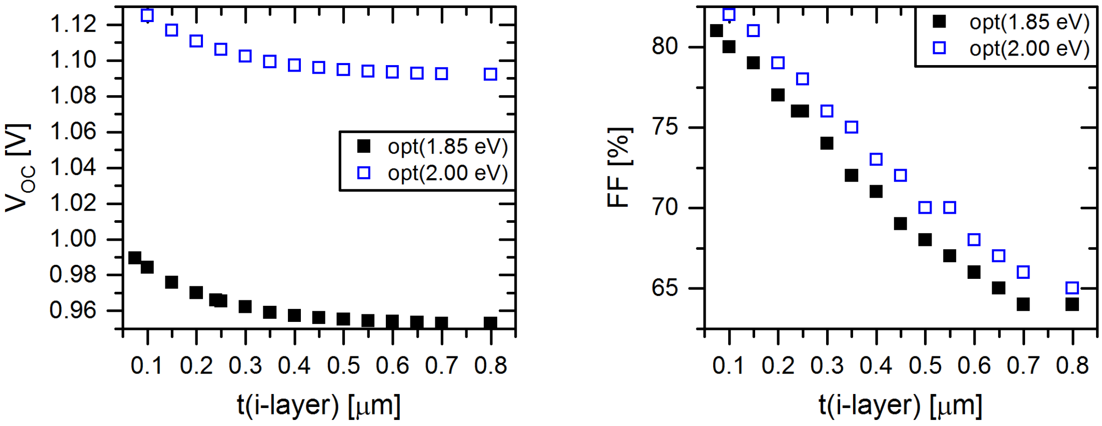

(a) Open circuit voltage. **(b)** Fill factor.

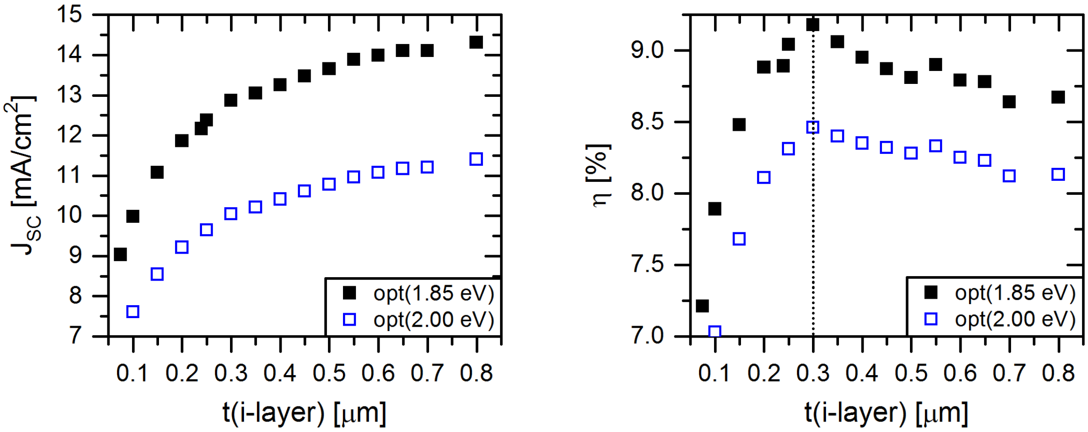

(c) Short circuit current. **(d)** Efficiency.

Figure 3.6: Simulated IV parameters for varying i-layer thicknesses.

bandgap would have to deliver 1.200 V open circuit voltage instead of just 1.102 V to achieve the same efficiency as the cell with 1.85 eV i-layer bandgap. These considerations only apply to the simulated single cell. In a multijunction cell the situation is different because the loss of the short circuit current affects all subcells. Therefore, the increased voltage of the top cell V_{OC}^1 has to compensate for all these losses, which becomes evident in the following formula for the triple cell efficiency:

$$\eta = \frac{(V_{OC}^1 + V_{OC}^2 + V_{OC}^3)\, J_{SC}\, FF}{P_{sun}} = \frac{(V_{OC}^1\, J_{SC} + V_{OC}^2\, J_{SC} + V_{OC}^3\, J_{SC})\, FF}{P_{sun}}. \qquad (3.4)$$

Figure 3.6d shows that the efficiency of the simulated single cell rises up to 300 nm i-layer thickness due to enhanced absorption. Then, the efficiency drops for higher thicknesses because the gain in short circuit current is overcome by the loss of open circuit voltage and fill factor. Consequently, the maximum reasonable top cell absorber layer thickness is 300 nm according to the simulation. Since this result is the same for two different i-layer bandgaps, it seems to be independent of the latter to a certain extent.

The fill factor of the top cell is not necessarily transferred to the multijunction cell, so the maximum efficiency of a multijunction cell might be achieved at a higher top cell absorber thickness. However, the current limiting subcell usually strongly influences the fill factor of the multijunction cell. Thus, a top cell with a high bandgap absorber is likely to take this part.

The material quality of amorphous silicon and its alloys deteriorates under illumination because of the Staebler-Wronski effect [61]. This light induced degradation of amorphous silicon solar cells is known to increase with the absorber layer thickness [62, 63]. Consequently, a limit of 300 nm for the thickness of the intrinsic layer is justified.

As long as a maximum absorber layer thickness of 300 nm is the only current limitation of the top cell, standard a-Si:H will always outperform any high bandgap alloy. Even if a reflecting layer behind the absorber is considered, the resulting current gain will always be higher in standard i-a-Si:H than in a high bandgap alloy.

3.5 Required Top Cell Bandgap for Optimal Short Circuit Current

In the previous section, it was established that standard a-Si:H will always be superior to any high bandgap absorber alloy as long as the i-layer thickness is the only criterion limiting the current. This only applies to a single cell, as presented in figure 3.4. In a multijunction cell, the current matching condition also sets an upper limit to the top cell current. In a triple cell, for example, the top cell current should be no more than one third of the total absorbed current.

Recently Sai et al. reported the development of a μc-Si:H single cell which produces 34.1 mA/cm^2 current at -4 V bias voltage and with 4 µm absorber thickness [3]. This current value is very high and quite close to the absorbed current at the Lambertian scattering limit of an equally thick c-Si slab [3]. The bottom cell absorber material is likely to be μc-Si:H. Therefore, a total absorbed current of 34.1 mA/cm^2 is very close to the realistic optimum for a thin-film silicon based multijunction cell. Consequently, the optimal top cell current of a triple or quadruple cell can be estimated to the following values:

$$\mathrm{J}_{opt}(\text{triple}) = \frac{34.1}{3}\,\mathrm{mA/cm^2} \approx 11.37\,\mathrm{mA/cm^2} \tag{3.5}$$

$$\mathrm{J}_{opt}(\text{quad}) = \frac{34.1}{4}\,\mathrm{mA/cm^2} \approx 8.53\,\mathrm{mA/cm^2}. \tag{3.6}$$

The optimal current value for the triple cell is very close to the current of $11.36\,\mathrm{mA/cm^2}$ simulated by Yunaz et al. for a triple configuration [8]. Thus, any high bandgap absorber should at least produce $11.37\,\mathrm{mA/cm^2}$ or $8.53\,\mathrm{mA/cm^2}$ short circuit current at a reasonable layer thickness in the respective cell configuration.

To answer the question, which maximum i-layer bandgap leads to sufficient short circuit current, the cell stack in figure 3.4 was simulated for varying i-layer bandgaps and thicknesses. The wavelength was ramped and the optical as well as the electrical solution was generated. Optimal p-layer bandgaps were used for each i-layer bandgap at constant optical data of the p-layer. The Urbach energy was kept constant at $E_U = 50\,\mathrm{meV}$.

Figure 3.7 shows the simulated short circuit current of the top cell against the i-layer thickness on the left side and against the i-layer bandgap at 300 nm i-layer thickness on the right side. The optimal top cell currents, which should be achieved in a triple or quadruple cell, are indicated by horizontal red and blue lines in each subfigure.

In figures 3.7a and 3.7b the data was generated with the optical conditions according to Isabella et al. [55] as described in section 3.2. For the data in figures 3.7c and 3.7d, scattering parameters fitted to a commercial Asahi-U substrate were used. Finally, figures 3.7e and 3.7f show simulation results, which were gained with Asahi-U scattering conditions, fitted nk-data of doped layers (see tables 2.2 and 2.3)[1] and digitised nk-data of SnO_2:F TCO from Schropp et al. [64]. For the intrinsic layer the optimised nk-data generated in this work in dependence on the bandgap is used in all cases.

Figures 3.7a, 3.7c and 3.7e show that the simulated short circuit current of the top cell first rises steeply with i-layer thickness and then more moderately (see also figure 3.6c and explanations in section 3.4). For higher i-layer bandgaps the moderate increase of J_{SC} starts at smaller i-layer thicknesses because there is no current gain from long-wave light. Otherwise, the curves are shifted downwards for higher i-layer bandgaps due to reduced absorption coefficients. Consequently, the intersection of the short circuit currents with the optimal triple and quadruple cell currents is transferred to higher i-layer thicknesses for higher i-layer bandgaps.

Figures 3.7b, 3.7d and 3.7f depict the short circuit current of the top cell against the

---

[1] The optical data of the standard n-a-Si:H layer was kindly provided by Tim Möller from NEXT ENERGY.

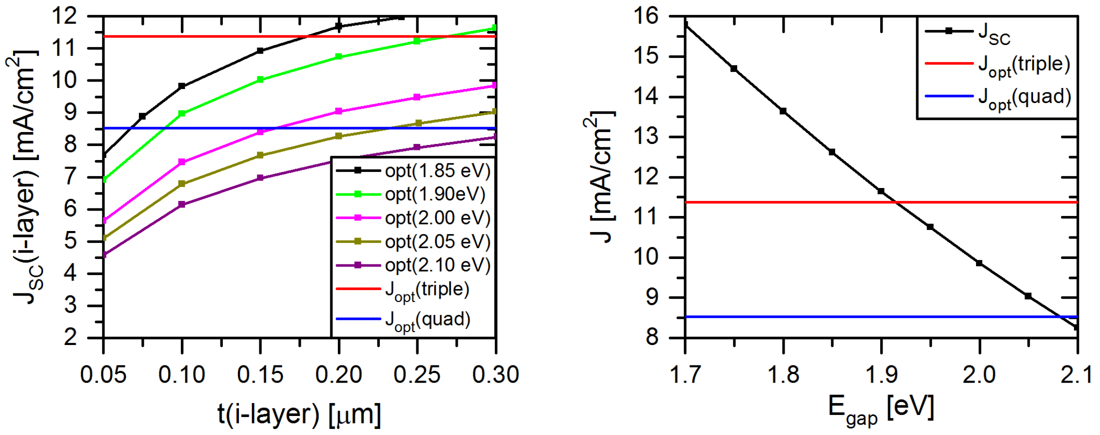

(a) Optics according to Isabella et al. [55].

(b) Optics according to Isabella et al. [55]

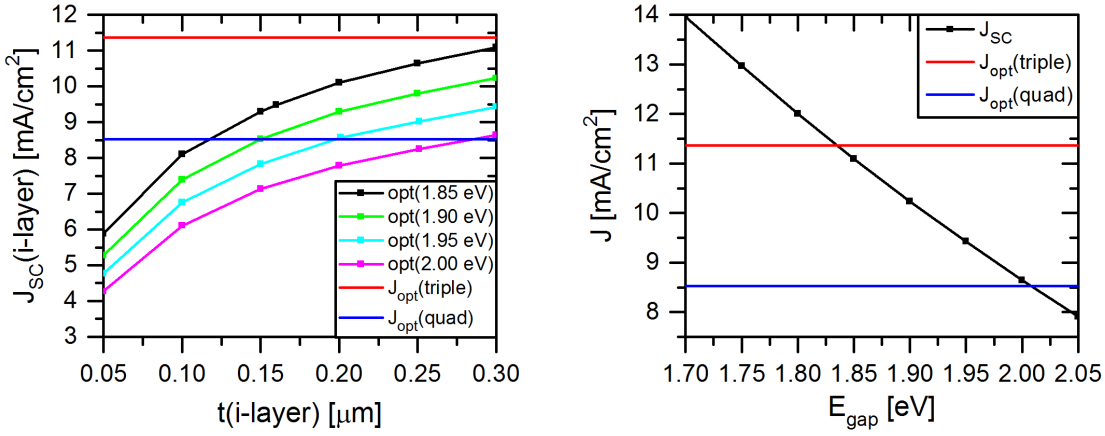

(c) Scattering distribution of Asahi-U substrate.

(d) Scattering distribution of Asahi-U substrate.

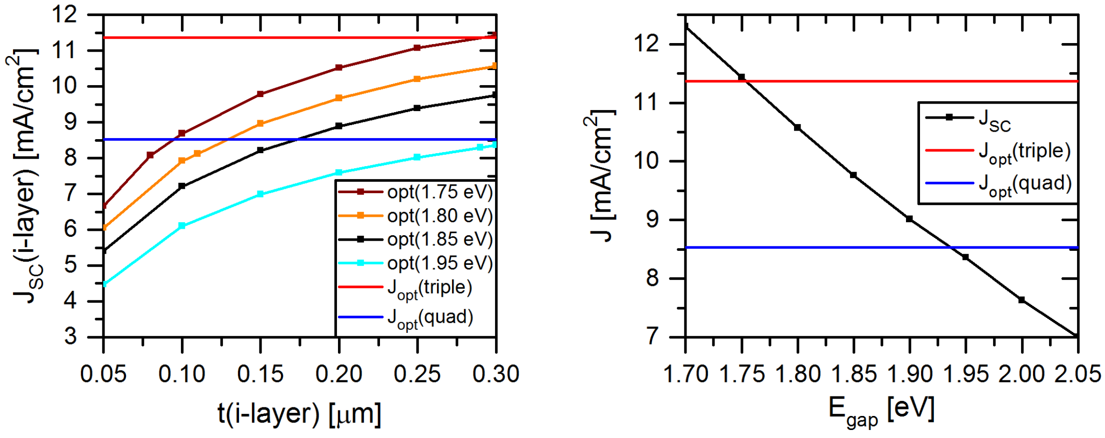

(e) Scattering distribution of Asahi-U substrate and fitted optical data of doped layers.

(f) Scattering distribution of Asahi-U substrate and fitted optical data of doped layers.

Figure 3.7: Left: Simulated short circuit current against i-layer thickness for varying i-layer bandgaps. Right: Simulated short circuit current against i-layer bandgap for an i-layer thickness of $300\,\mathrm{nm}$.

i-layer bandgap at a maximum reasonable i-layer thickness of 300 nm. When the best optical conditions of this work (Isabella et al. [55]) are assumed, the short circuit current of the top cell meets the optimal triple cell current at an i-layer bandgap of about 1.91 eV (see figure 3.7b). This bandgap can even be achieved without additional alloying of i-a-Si:H [54]. Therefore, the simulation predicts that the enhancement of the top cell bandgap to 2 eV, as suggested by Yunaz et al. [8], is not beneficial for a thin-film silicon triple cell. An intermediate reflector following the top cell could increase the short circuit current and consequently the optimum top cell bandgap. However, this would also lead to more reflection losses right in the middle of the cell stack and reduce the absorption of the bottom cells.

For a quadruple cell, the optimum top cell bandgap is higher than for the triple cell. Consequently, the curves of the short circuit current and the optimal quadruple cell current in figure 3.7b intersect at a bandgap of approximately 2.08 eV.

The previous results have been obtained with optimal optical conditions. If the scattering parameters are changed to represent the scattering conditions of a commercial Asahi-U substrate and the light beam starts in air instead of glass, the short circuit current is reduced for each i-layer bandgap (see figure 3.7c). Moreover, the optimal top cell absorber bandgap at 300 nm i-layer thickness is lowered from 1.91 to 1.83 eV and from 2.08 to 2.01 eV for a triple and a quadruple cell respectively. Figures 3.7e and 3.7f depict the simulation results for non optimised optical data of the front layers, the light beam starting in air and Asahi-U scattering parameters. As a result, the short circuit current decreases further. The optimal top cell bandgaps for a triple and a quadruple cell are only 1.75 eV and 1.93 eV in this case (see figure 3.7f).

So, in order to develop an optimised top cell for a multijunction configuration, it is important to have high quality front layers with low absorption, excellent scattering conditions and an antireflection coating. Apart from good electrical quality, the top cell absorber requires a bandgap which allows for sufficient absorption to reach the optimal current given by the number of subcells.

Table 3.3 presents the simulation results of the top cell under the best mentioned optical conditions and with $E_U = 50\,\mathrm{meV}$ Urbach energy. Apart from one exception, the top cell absorber layer thickness was adjusted, so the optimal triple ($11.37\,\mathrm{mA/cm^2}$) or quadruple ($8.53\,\mathrm{mA/cm^2}$) short circuit current is achieved. For the top cell bandgap of 1.95 eV combined with 300 nm absorber thickness, the short circuit current is only $10.94\,\mathrm{mA/cm^2}$ instead of $11.37\,\mathrm{mA/cm^2}$. Triple and quadruple cell efficiencies were calculated using the optimal short circuit currents as well as the simulated open circuit voltage and fill factor of the top cell. The open circuit voltages of the bottom cells were taken from literature

absorber	V_{OC} [V]	source
i-a-SiGe:H	0.743	[51]
μc-Si:H	0.505	[51]
μc-SiGe:H	0.494	[52]

Table 3.2: Open circuit voltages from literature.

$E_{gap}(top)$ [eV]	t(i-layer, top) [nm]	$V_{OC}(top)$ [V]	FF [%]	$\eta(triple)$ [%]
1.85	170	0.973	77	19.45
1.90	245	1.013	76	19.54
1.95	300	1.057	75	18.91
$E_{gap}(top)$ [eV]	t(i-layer, top) [nm]	$V_{OC}(top)$ [V]	FF [%]	$\eta(quad)$ [%]
1.85	65	0.991	80	18.65
1.90	83	1.034	81	19.18
1.95	111	1.078	80	19.24
2.00	150	1.117	81	19.75
2.05	210	1.156	80	19.78

Table 3.3: Simulated top cell parameters and calculated triple and quadruple cell efficiencies at optimal short circuit currents of 11.37 and $8.53\,\mathrm{mA/cm^2}$.

(see table 3.2).

The quadruple cell efficiency in table 3.3 is lower than the triple cell efficiency at equivalent top cell bandgaps. The reason for this observation is that the reduction of thermalization losses in a quadruple cell cannot show if fixed bottom cell voltages are used. According to the simulation, the triple cell efficiency rises by 0.09 % if the top cell bandgap is increased from 1.85 to 1.90 eV. It reaches a maximum of 19.54 %. Increasing the top cell bandgap further to 1.95 eV shows no merit because the higher open circuit voltage cannot compensate the loss of short circuit current and fill factor. The quadruple cell efficiency can be enhanced by 0.6 % when the top cell bandgap is changed from 1.9 to 2.05 eV. This leads to an efficiency of 19.78 % which is very close to the quadruple cell efficiency of 19.83 % obtained by Isabella et al. [55].

3.6 Conclusion

When developing a high bandgap top cell absorber alloy, the question arises which advantage this material could have over standard a-Si:H and which bandgap is required to still absorb sufficient current in a triple or quadruple cell. In order to solve this problem, four questions were developed in the introduction of this chapter. The following answers were gained with the help of optical and electrical simulations:

1. The OJL fit parameters of standard i-a-Si:H are considered as the optimum for any high bandgap alloy since the material quality deteriorates with alloying.
2. The optimum p-layer bandgap in a top cell is about 0.25 eV higher than the following i-layer bandgap.
3. The maximum reasonable top cell absorber thickness is about 300 nm. Standard i-a-Si:H always results in higher single cell efficiency than any high bandgap alloy at an equivalent absorber thickness due to superior short circuit current.
4. The optimal short circuit current of a triple cell is $J_{opt}(\text{triple}) = 11.37\,\text{mA/cm}^2$ and of a quadruple cell $J_{opt}(\text{quad}) = 8.53\,\text{mA/cm}^2$. The highest top cell bandgap which leads to the optimal triple cell current at an absorber thickness of 300 nm is 1.91 eV. This is considerably lower than the optimal bandgap of 2 eV reported previously. In the case of a quadruple cell the highest bandgap leading to the required top cell current at 300 nm absorber thickness is about 2.08 eV.

If the bandgap of standard i-a-Si:H is assumed to be 1.85 eV, increasing this bandgap to 1.90 eV raises the triple cell efficiency by 0.09 %. The quadruple cell efficiency is enhanced by 0.6 % when the bandgap is increased from 1.90 to 2.05 eV. These improvements lead to a triple cell efficiency of 19.54 % and a quadruple cell efficiency of 19.78 %. In summary, the simulation results suggest that high bandgap i-a-Si:H is sufficient for the optimization of the top cell in a triple configuration. Raising the top cell absorber bandgap to 2 eV or beyond by alloying amorphous silicon with carbon or oxygen might be beneficial in a quadruple cell.

4

Process Development

The results of the previous chapter recommend a high bandgap i-a-Si:H top cell absorber for a triple cell but further bandgap widening of the top cell absorber for a quadruple cell. Therefore, this chapter is dedicated to the process development of high bandgap amorphous silicon alloys. For this purpose the parameters of the RF-PECVD process have to be adjusted compared to the standard recipes (see table 2.2). The optimization of both the i- and the p-layer process parameters is crucial for the quality of the complete cell. The open circuit voltage is defined by the potential difference of the Fermi levels at the solar cell contacts. Therefore, the p-layer also requires a widened bandgap, so it does not limit the potential of the i-layer to increase the open circuit voltage [18]. The bandgap of the n-layer has no strong influence on the open circuit voltage. Consequently, a standard n-a-Si:H layer was employed (see table 2.2).

The process parameters of the i- and p-layer were optimised using CO_2 and the comparison with the other source gases was carried out under similar process conditions. The aim of the optimization is to raise the open circuit voltage above the value of the standard a-Si:H single cell without significant loss of fill factor. This is realised at low CO_2 flow ratios as demonstrated by figure 4.1. The highest open circuit voltage of 1 V is achieved with CH_4 in this work. In the following, the steps leading to the optimised amorphous silicon alloys will be discussed.

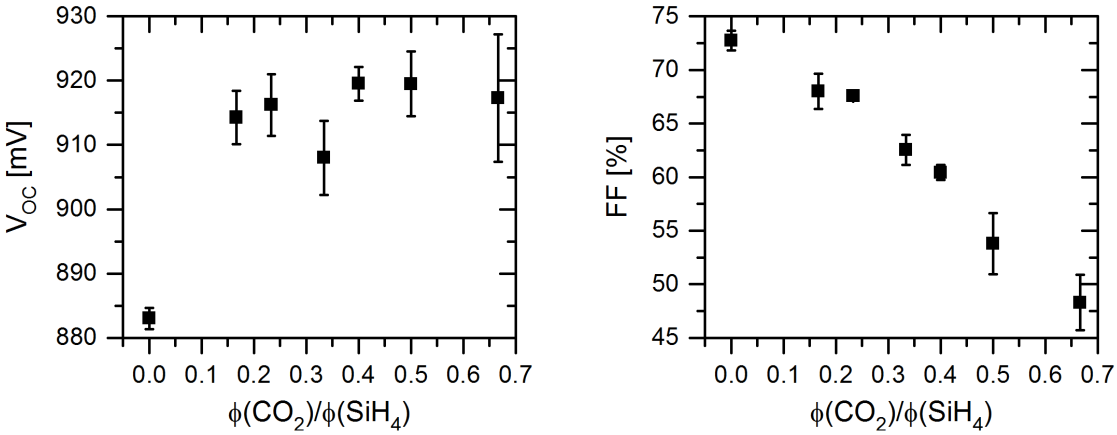

(a) Open circuit voltage. **(b)** Fill factor.

Figure 4.1: IV parameters of optimised a-SiO:H single cells at different flow ratios of CO_2 and SiH_4 in the intrinsic layer.

4.1 Development of the Intrinsic Layer

4.1.1 CO_2 Flow Variation

High bandgap intrinsic amorphous silicon alloys were developed starting with the deposition parameters of standard i-a-Si:H (see table 2.2). As a first variation CO_2 was added to the process gases in different concentrations. Figure 4.2 shows that the optical bandgap and the growth rate of single layers increase with the CO_2 fraction as expected [11]. A Tauc bandgap of 2 eV is barely reached at the highest CO_2 flow ratio. Das et al. [25] also observed an enhanced growth rate with the addition of oxygen. They explained their findings by the electronegativity of oxygen causing a higher effective electron density in the plasma for the decomposition of silane.

The i-a-SiO:H layers were tested as single cell absorbers in the following layer stack outlined in figure 4.3: glass/SnO_2:F/p-a-SiO:H/i-a-SiO:H/n-a-Si:H/Ag. This layer stack was used for all remaining development steps. The IV parameters of single cells prepared with different flow ratios of CO_2 in the i-layer are depicted in figure 4.4. The fill factor, short circuit current and efficiency decline with increasing CO_2 flow ratio. Moreover, the open circuit voltage decreases by approximately 30 mV and then stays more or less constant. The series resistance rises and the parallel resistance drops both accounting for the decrease in fill factor with CO_2 flow ratio.

Oxygen is yet another impurity in the material. It produces a higher bond angle in the Si-O-Si bridge than the silicon tetrahedron angle [65]. Moreover, oxygen has the

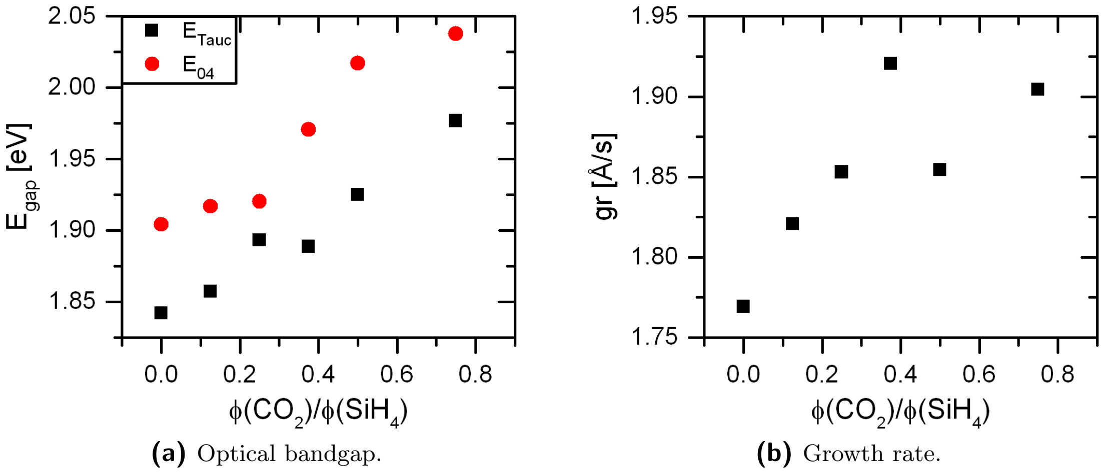

(a) Optical bandgap.

(b) Growth rate.

Figure 4.2: Properties of i-a-SiO:H single layers at different flow ratios of CO_2 and SiH_4.

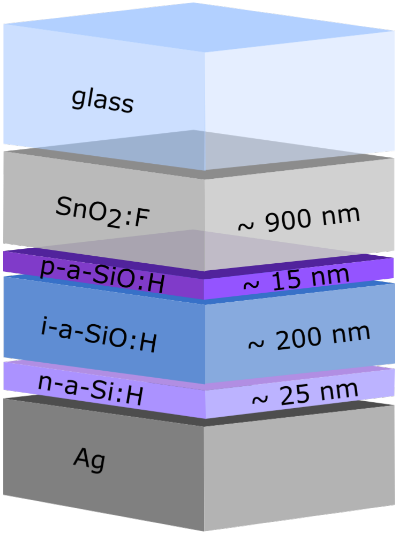

Figure 4.3: Sketch of the layer stack for the development of high voltage single cells.

tendency to form a-SiO:H clusters [66]. Therefore, the deterioration of material quality with oxygen content apart from stoichiometry is expected. This is demonstrated by the decrease of the fill factor and the open circuit voltage. Yet, it should be possible to retain good material quality at low oxygen concentrations. While the drop in short circuit current is anticipated due to bandgap widening, the open circuit voltage should increase for the material to be feasible as a high bandgap absorber. Consequently, further process development steps are needed to reach sufficient material quality.

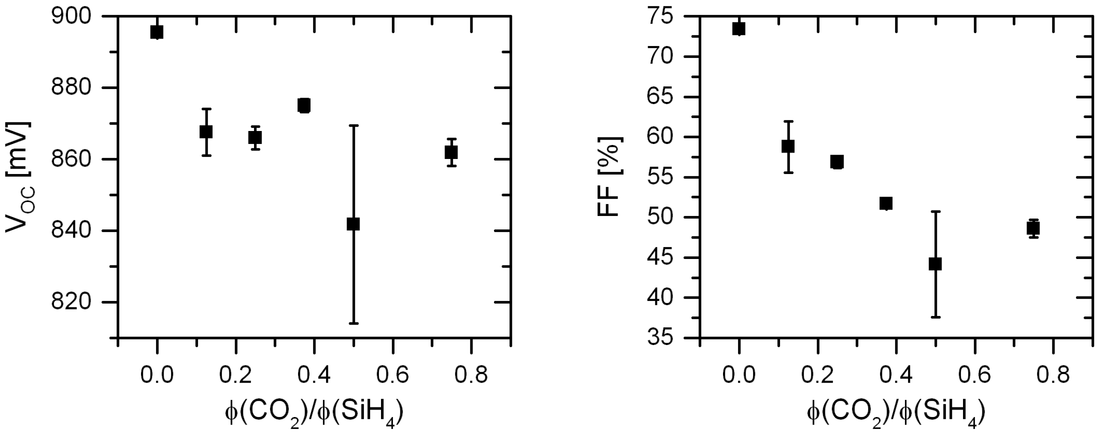

(a) Open circuit voltage. **(b)** Fill factor.

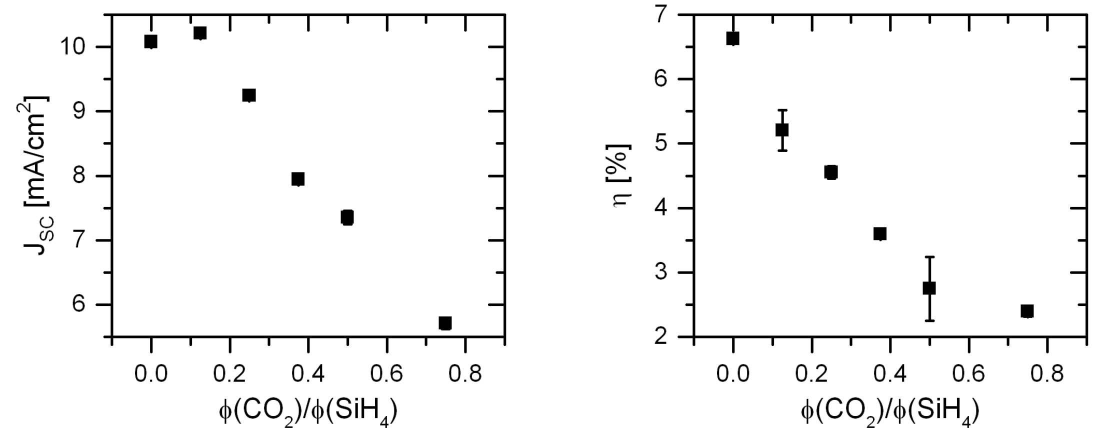

(c) Short circuit current. **(d)** Efficiency.

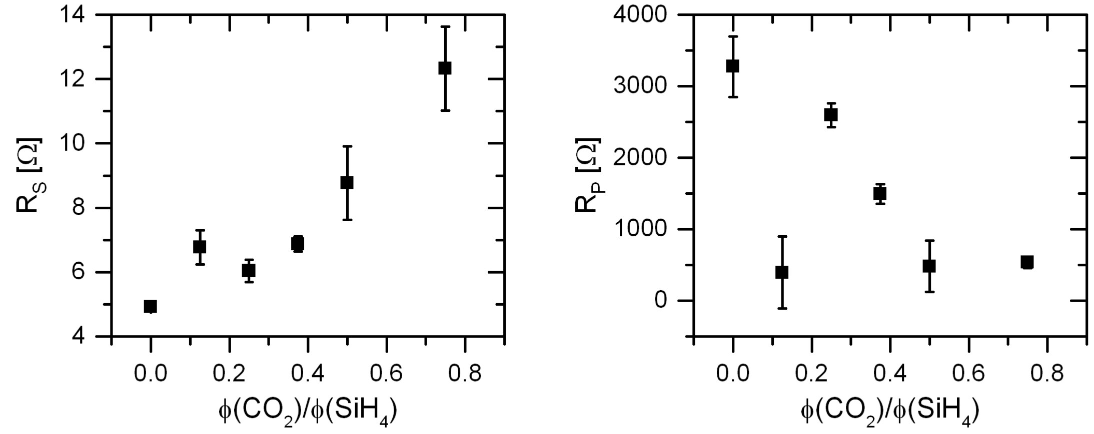

(e) Series resistance. **(f)** Parallel resistance.

Figure 4.4: IV parameters of a-SiO:H single cells at different flow ratios of CO_2 and SiH_4 in the intrinsic layer.

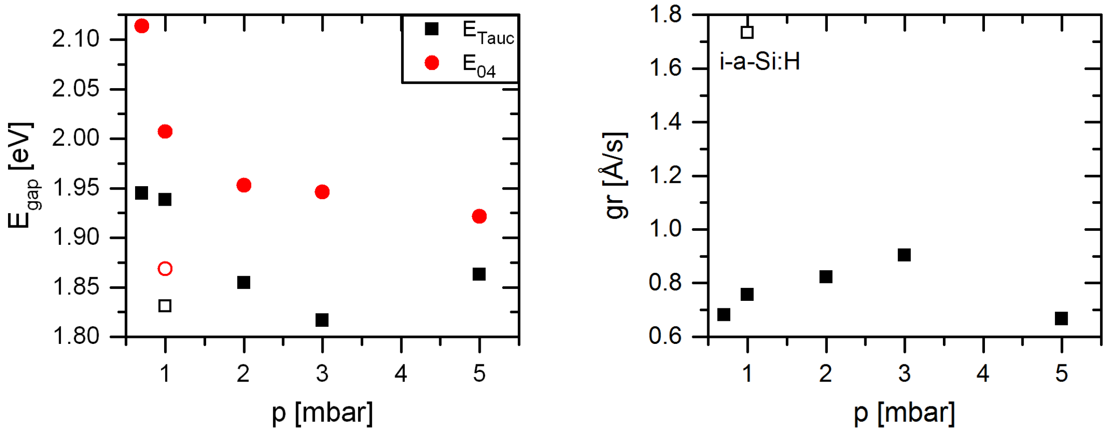

(a) Optical bandgap. **(b)** Growth rate.

Figure 4.5: Properties of i-a-SiO:H single layers against process pressure.

4.1.2 Pressure Variation

Process pressure variation was carried out for the deposition of i-a-SiO:H layers. Higher pressure is expected to decrease the oxygen incorporation and to increase the growth rate like in i-a-Si:H [14, 26]. Figure 4.5 shows the optical bandgap and the growth rate of i-a-SiO:H single layers at varying process pressures. The CO_2 flow ratio was fixed at $\phi(CO_2)/\phi(SiH_4) = 0.25$. The open symbols represent standard i-a-Si:H layers without oxygen and at six times lower hydrogen dilution for comparison. Thus, these layers exhibit a lower bandgap and much higher growth rate.

The Tauc bandgap and E_{04} of the i-a-SiO:H layers decrease with rising process pressure except for the last value of E_{Tauc} at 5 mbar. Similarly, Iftiquar [26] et al. report a decline of oxygen content and bandgap with rising process pressure. They explain this behaviour by higher process pressures leading to lower electron temperature and kinetic energy of the electrons. As a result, less hydrogen molecules are split to help in the dissociation of CO_2. From figure 4.5a, one can deduce that the smallest difference between the E_{04} and E_{Tauc} bandgap is achieved at low and high pressures indicating that the absorption coefficient of these samples rises more steeply [67].

The growth rate behaves contrarily to the Tauc bandgap. The rise in growth rate with the process pressure can be explained by the greater density of all precursors in the reaction zone. Moreover, the presence of electronegative oxygen accelerates the reaction with SiH_3 radicals at the film surface [26]. Higher pressure enhances the precursor density but lowers the electron temperature for the primary dissociation. This might explain why at a pressure of 5 mbar the growth rate decreases again.

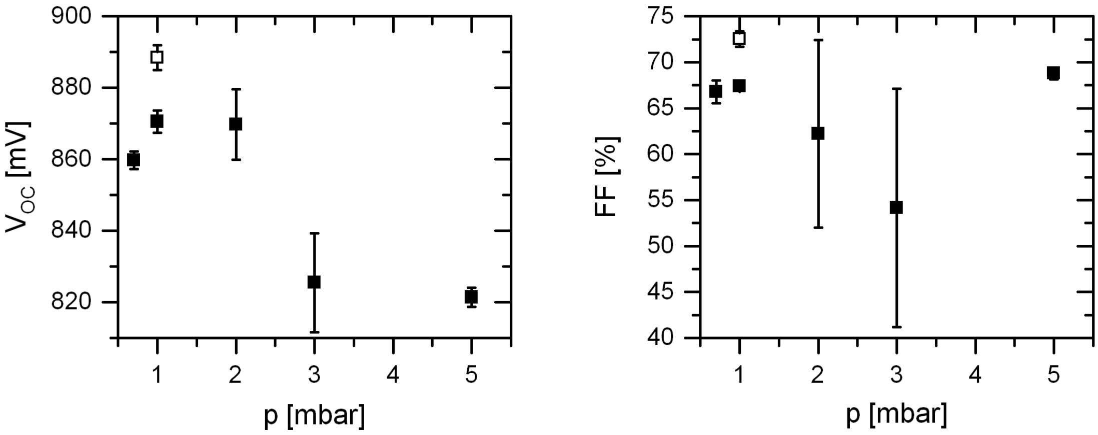

(a) Open circuit voltage. **(b)** Fill factor.

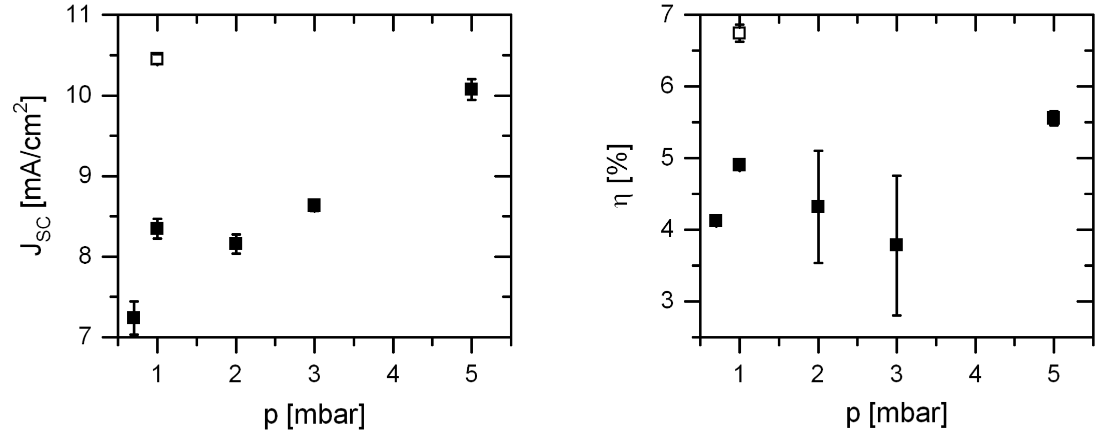

(c) Short circuit current. **(d)** Efficiency.

Figure 4.6: IV parameters of a-SiO:H single cells against process pressure in the intrinsic layer.

The current-voltage parameters of single cells are depicted in figure 4.6 at different process pressures for the intrinsic layer. The open symbols characterise single cells with the standard i-a-Si:H absorber. According to the trend of the bandgap in figure 4.5a, the open circuit voltage decreases and the short circuit current increases with rising process pressure. Moreover, the drop of open circuit voltage is also influenced by the deterioration of material quality. The fill factor and the efficiency are highest for low and high pressures. Therefore, either a process pressure of 1 mbar or of 5 mbar yields the best single cell performance and material quality. Since the optical bandgap is higher for lower process pressures, it is preferable to keep the process pressure at the standard value of 1 mbar. This conclusion corresponds to the results of Kim et al. who also obtained better material quality for i-a-SiO:H produced at a low CO_2 flow and a low pressure of

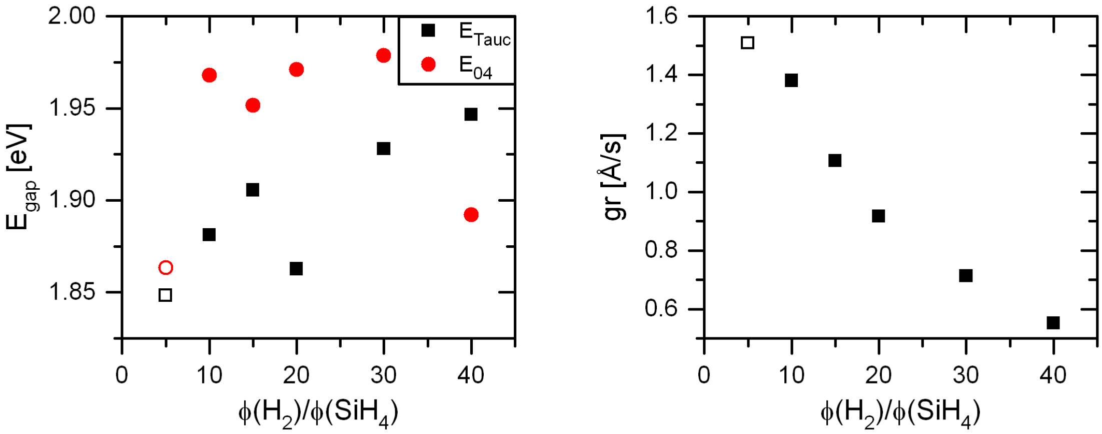

(a) Optical bandgap. **(b)** Growth rate.

Figure 4.7: Properties of i-a-SiO:H single layers at different flow ratios of H_2 and SiH_4.

approximately 2 mbar [14]. Low pressure reduces the growth rate (see figure 4.5b) which helps a denser network growth [27]. Nevertheless, as can be seen in figure 4.6a, the aim of raising the open circuit voltage above the value of the a-Si:H standard cell has not been achieved yet.

Experiments with N_2O and CH_4, which are not shown here, and results from literature with CO_2 [14] indicate that lower rf-power is beneficial for material quality. This can be explained by lower growth rate and reduced ion bombardment, which otherwise can destroy the atomic network [14, 27]. Thus, the lowest available power value ($P = 17.5\,\mathrm{mW/cm^2}$) of the i-a-Si:H standard layer was kept for the i-a-SiO:H layer development.

4.1.3 Hydrogen Dilution

One basic approach for the improvement of material quality by variation of process parameters is hydrogen dilution. Hydrogen can have a beneficial effect on layer growth by passivating defects, relaxing the network and etching weak bonds [22]. The reduction of growth rate by hydrogen dilution can lead to increased film density [27]. Yet, clustering of hydrogen is detrimental because it occurs at voids or vacancies in the network and enhances light induced degradation [43].

Figure 4.7 presents the optical bandgaps and the growth rate of i-a-SiO:H single layers at varying hydrogen dilution and at a constant CO_2 flow ratio of $\phi(CO_2)/\phi(SiH_4) = 0.25$. The open symbols represent the standard i-a-Si:H layer without oxygen. The Tauc bandgap rises with hydrogen dilution as expected since hydrogen replaces weak silicon

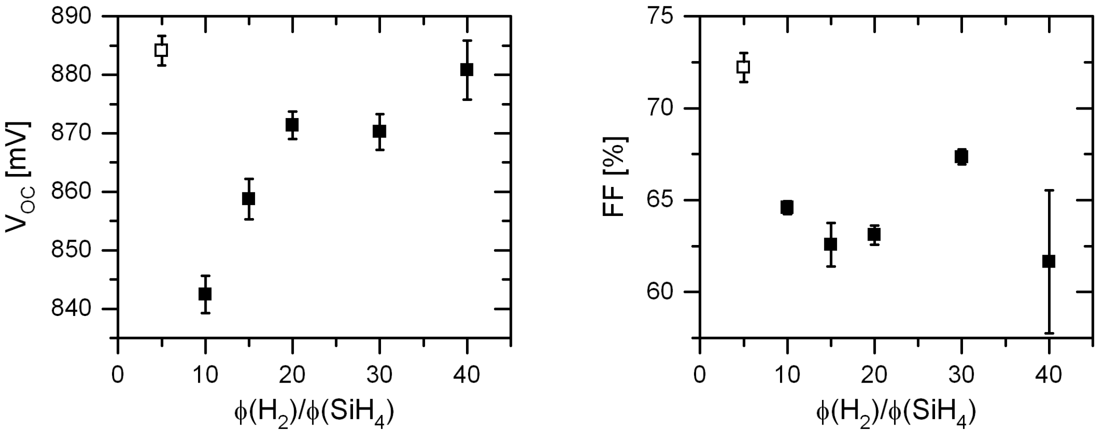

(a) Open circuit voltage. **(b)** Fill factor.

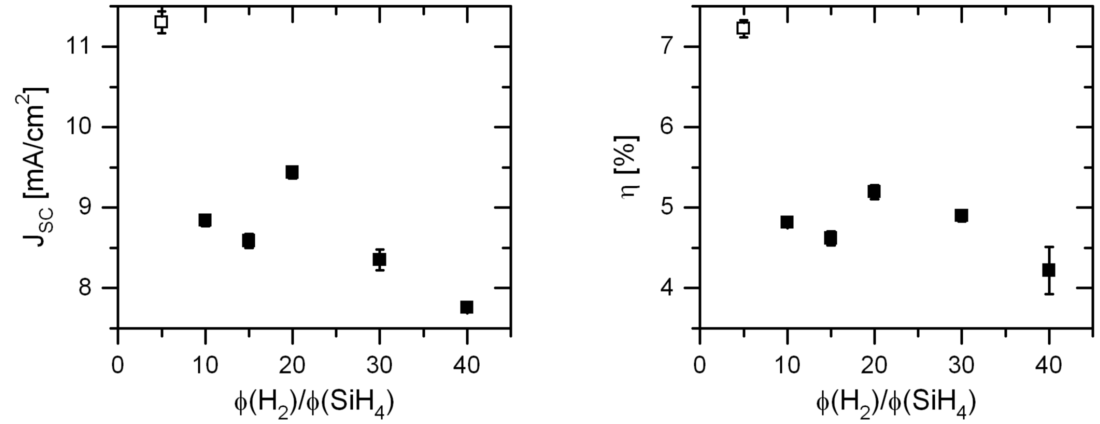

(c) Short circuit current. **(d)** Efficiency.

Figure 4.8: IV parameters of a-SiO:H single cells at different flow ratios of H_2 and SiH_4 in the intrinsic layer.

bonds at the valence band edge by shorter silicon-hydrogen-bonds deeper in the bands [68]. Thus, hydrogen enhances the bandgap by its intrinsic alloying effect but also by increasing the structural order of the film [69].

The growth rate decreases with hydrogen dilution because hydrogen etches weak bonds and partly shields the surface of the film from growth precursors [22]. Moreover, the total flow is increased by raising the hydrogen flow so that the species have less time to react with the growing surface before leaving the chamber again.

The hydrogen diluted intrinsic single layers were also used as absorber layers in a-SiO:H single cells. Figure 4.8 shows the corresponding IV parameters. The open symbols represent cells with the standard i-a-Si:H absorber layer. Although the open circuit

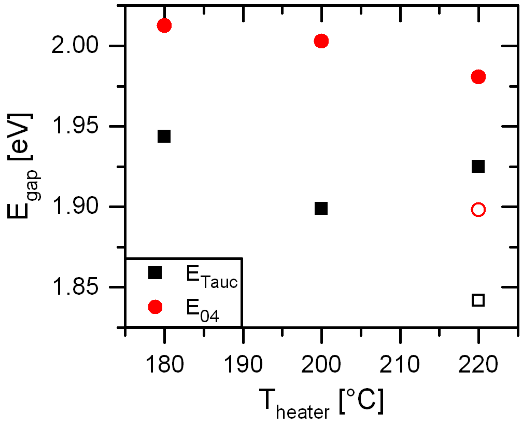

Figure 4.9: Optical bandgap of i-a-SiO:H single layers against heater temperature.

voltage drops with the addition of CO_2, it rises again with hydrogen dilution. This can be explained by the increased bandgap (see figure 4.7a) but also by better material quality. Hydrogen dilution has a positive influence on the fill factor at a hydrogen flow ratio of 30. The short circuit current drops with hydrogen dilution and behaves contrarily to the Tauc bandgap as expected [54]. The maximum efficiency is achieved with a hydrogen flow ratio of 20 because of enhanced short circuit current. The exceptional current value is caused by unintentional changes of the p-layer or the absorber thickness. So, it is not related to the material quality of the intrinsic layer. Therefore, a flow ratio of 30 was chosen for future developments in favour of a better fill factor. The open circuit voltage could be increased by hydrogen dilution almost up to the value achieved with the standard i-a-Si:H absorber.

4.1.4 Variation of the Heater Temperature

As a next step, the heater temperature and consequently the substrate temperature was varied for the i-layer development. Higher substrate temperature increases the mobility of the precursors at the growth surface which is beneficial for a dense network [14, 27]. Yet, higher substrate temperature leads to the desorption and emission of hydrogen so that the hydrogen content and the bandgap are reduced [14, 25]. Hydrogen is preferable to oxygen in a high bandgap alloy [14]. Therefore, the heater temperature was lowered starting with the standard value of 220 °C.

In figure 4.9, the optical bandgaps of i-a-SiO:H single layers are depicted for various heater temperatures. The open symbols mark the results from the standard i-a-Si:H layer. Except for the Tauc bandgap at a heater temperature of 200 °C, the optical bandgaps

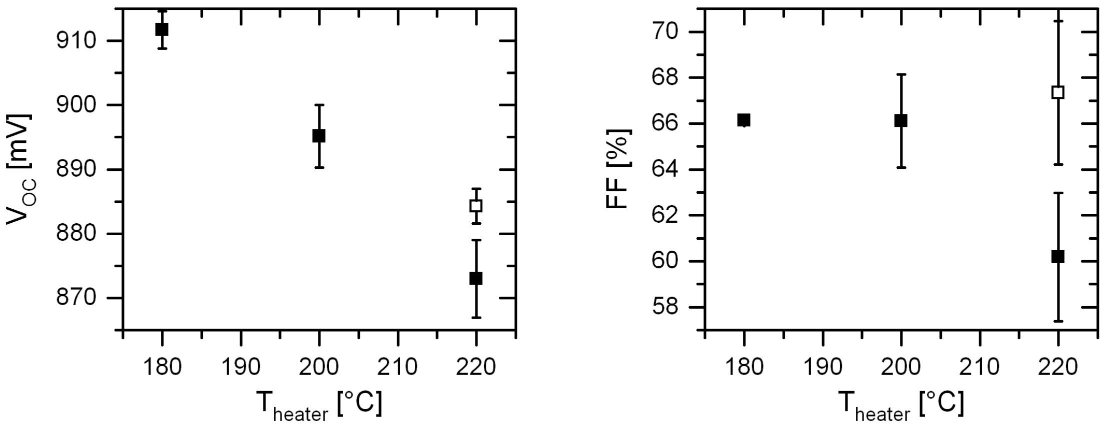

(a) Open circuit voltage. **(b)** Fill factor.

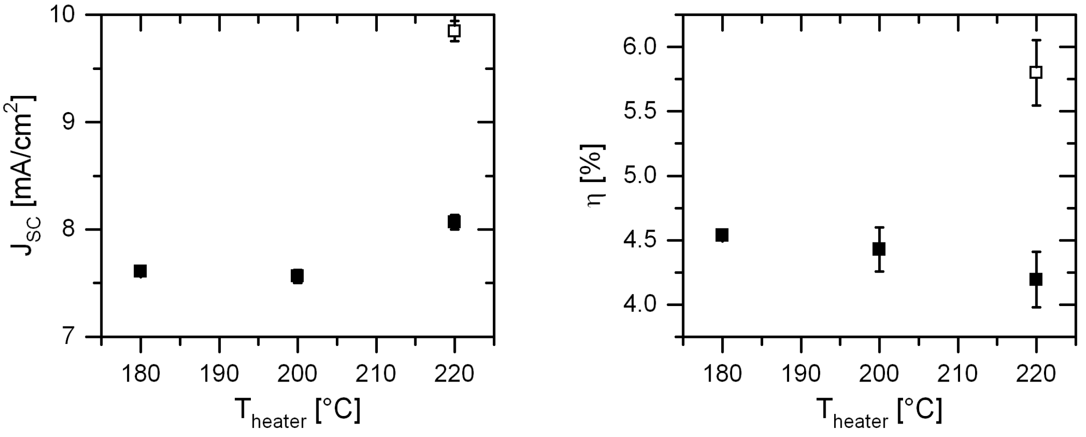

(c) Short circuit current. **(d)** Efficiency.

Figure 4.10: IV parameters of a-SiO:H single cells at different heater temperatures for the intrinsic layer.

increase with decreasing substrate temperature in accordance with the discussion above. The IV parameters of single cells at different heater temperatures for the i-a-SiO:H and i-a-Si:H absorbers are presented in figure 4.10. The open circuit voltage rises with decreasing heater temperature and for the first time surpasses the value of the a-Si:H reference cell by approximately 25 mV. This can be explained by the higher bandgap and the positive effects of hydrogen on layer growth at lower heater temperatures. Thus, hydrogen passivates defects, relaxes the network, etches weak bonds and shields the growing surface from unfavourable growth precursors. The fill factor rises when the heater temperature is lowered from 220 to 200 °C. This trend contradicts the results of Kim et al. who report a drop in fill factor with decreasing heater temperature [14]. Possibly the positive effects of hydrogen compensate the reduced surface reaction rate at low heater temperatures in our case. Yet, the fill factor of the reference cell is uncharacteristically low at a heater temperature of 220 °C. Moreover, the fill factors of the alloyed cells do not rise above the values achieved in the former development steps. The short circuit current decreases slightly with lower heater temperature, which can be attributed to the increased bandgap. A heater temperature of 180 °C leads to the highest open circuit voltage and efficiency of the alloyed cells.

4.2 Development of the p-doped Layer

The motivation for using high bandgap amorphous p-layer alloys is to enhance the open circuit voltage and the short circuit current. The open circuit voltage is raised because the increased p-layer bandgap forms a barrier for the holes in the i-layer and slows down their extraction at the front contact. As long as the holes still pass the barrier and do not recombine at defects, their quasi Fermi level is lowered and the open circuit voltage is increased. The short circuit current rises with the p-layer bandgap because the parasitic absorption of the p-layer is reduced, which enhances the absorption of the i-layer.

Apart from amorphous doped layers with high bandgaps, p- and n-doped nc-SiO:H has been developed by several research groups [51, 70, 71]. This kind of material consists of two phases with vertical crystalline silicon filaments for good electrical conduction and a surrounding a-SiO:H matrix for high transparency. In multijunction cells, n-doped nc-SiO:H layers do not only help to separate the charge carriers but also contribute to light management as back and intermediate reflectors. P-doped nc-SiO:H layers ensure good electrical conduction at high transparency. Yet, since their electrical bandgap is determined by the crystalline silicon filaments, they do not enhance the open circuit voltage. Here, only amorphous high bandgap p-doped layers will be treated.

4.2.1 CO_2 Flow Variation

As a first development step, CO_2 was added to the standard recipe of the p-doped layer. Figure 4.11 shows the corresponding single layer properties. The Tauc bandgap rises almost linearly with the CO_2 flow ratio while the dark conductivity at room temperature decreases exponentially in accordance with Janotta et al. [72]. Comparing figures 4.2a and 4.11a, it becomes clear that a higher CO_2 flow ratio is required in the p-layer to achieve the same Tauc bandgap as in the intrinsic layer. This can be explained by the lowering effect of B_2H_6 on the optical bandgap [73, 74]. The activation energy in figure 4.11c does not show any clear trend with the CO_2 flow ratio but generally seems to be a

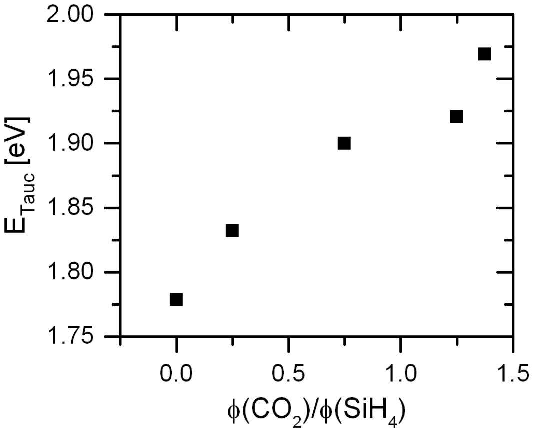

(a) Tauc bandgap.

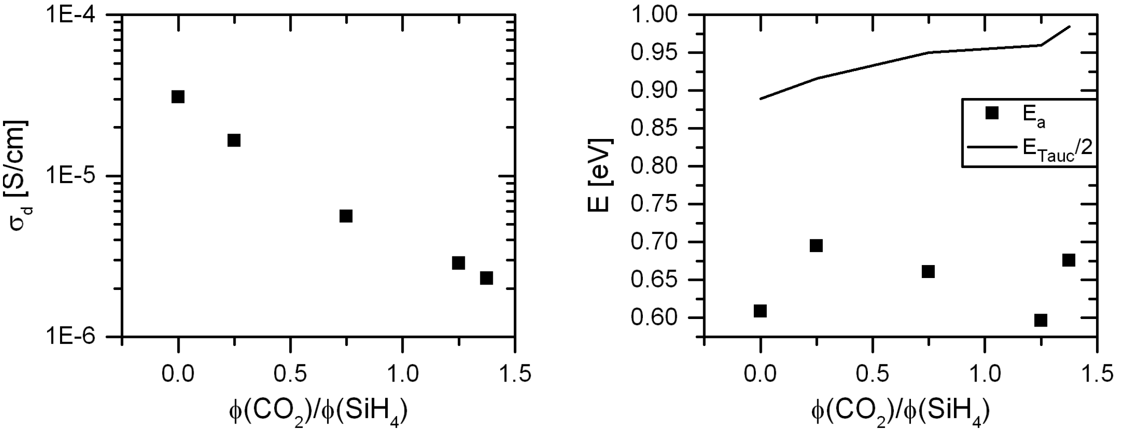

(b) Dark conductivity at room temperature.

(c) Activation energy.

Figure 4.11: Properties of p-a-SiO:H single layers against different flow ratios of CO_2 and SiH_4.

bit higher when CO_2 is added. According to Janotta et al. [72], the activation energy is expected to rise with the optical bandgap due to the increased CO_2 flow ratio.

Single cells were prepared with the p-a-SiO:H layers from above and with intrinsic as well as n-doped standard layers. The corresponding IV parameters are depicted in figure 4.12 for different CO_2 flow ratios in the p-doped layer. As expected, the open circuit voltage and the short circuit current increase with the CO_2 flow ratio and the p-layer bandgap (see figures 4.12a and 4.12c). Yet, the short circuit current in figure 4.12c only rises above the value of the standard cell at high CO_2 flow ratios. This leads to a maximum of about $1\,\mathrm{mA/cm^2}$ short circuit current that is gained by the addition of CO_2 in the p-layer process. The non-monotonic behaviour of the short circuit current is surprising since the Tauc bandgap increases monotonically with the CO_2 flow ratio (see figure 4.11a). Ex-

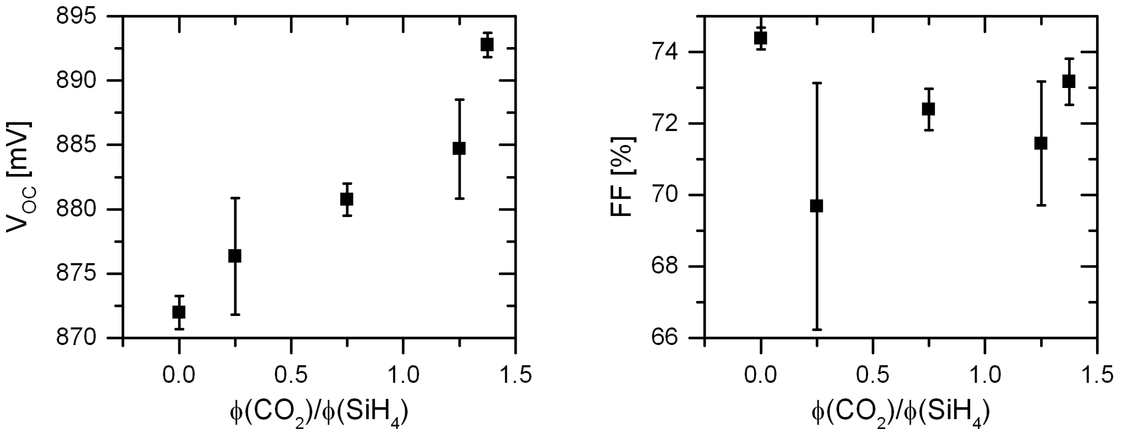

(a) Open circuit voltage.

(b) Fill factor.

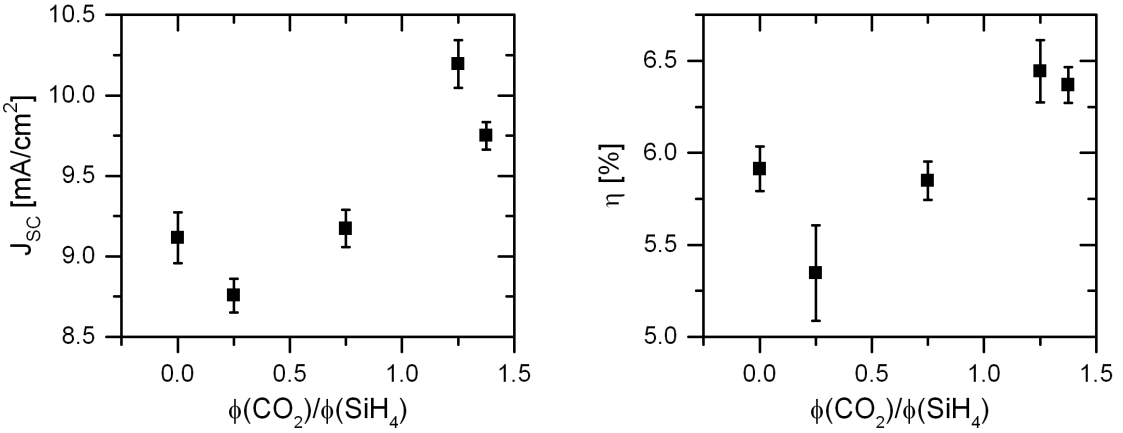

(c) Short circuit current.

(d) Efficiency.

Figure 4.12: IV parameters of a-Si:H single cells at different flow ratios of CO_2 and SiH_4 for the p-doped layer.

planations for this discrepancy could be a similar non-monotonic trend of the activation energy in figure 4.11c or unintended different p- and i-layer thicknesses.

Figure 4.13 depicts the EQE curves of the single cells prepared with different flow ratios of CO_2 in the p-layer. The EQE curves show that the short circuit current is mainly influenced by the spectral response in the blue part, which reflects the transparency of the p-layer and the p/i-interface properties. The only exception occurs for $\phi(CO_2)/\phi(SiH_4) = 1.25$ where the higher short circuit current compared to the highest CO_2 flow ratio is caused mainly by the red spectral response. This can be explained by unintended different i-layer thicknesses or deviating scattering properties.

The fill factor drops slightly, when CO_2 is added to the p-layer process gases, and then

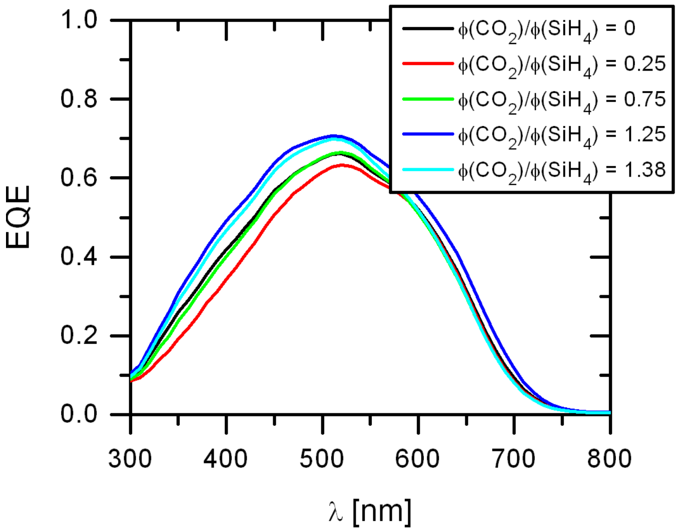

Figure 4.13: EQE of a-Si:H single cells at different flow ratios of CO_2 and SiH_4 for the p-doped layer.

stays constant (see figure 4.12b). The small decline of fill factor can be explained by the deterioration of the electrical quality of the p-layers with CO_2 flow ratio (see figures 4.11b and 4.11c). The improvement of open circuit voltage and short circuit current at high CO_2 flow ratios lead to an increase of efficiency by about 0.5 % compared to the standard cell.

4.2.2 SiH_4 Flow Variation

Since the maximal available CO_2 flow was already reached in the previous experiment, the silane flow in the production of the p-a-SiO:H layer was lowered to see if the bandgap could be raised further without serious deterioration of the electric properties. By lowering the silane flow the ratios of CO_2, H_2 and B_2H_6 become larger.

Figure 4.14 shows the IV parameters of a-SiO:H single cells against the silane flow in the p-a-SiO:H layer. The p-doped layers of all cells contain oxygen. The open symbols represent a cell with the i-a-Si:H standard layer while all other cells contain the same non-optimised high bandgap intrinsic absorber developed until then. Apart from outliers, the open circuit voltage and the short circuit current rise with decreasing silane flow because the Tauc bandgap of the p-layer is increased (see figure 4.15a). The fill factor is maximal for 25 sccm silane flow. It drops for the lowest silane flow, which can be explained by the reduced dark conductivity (see figure 4.15b) and the higher activation energy (see figure 4.15c). Efficiency is highest for the lowest silane flow. Nevertheless, in favour of the highest V_{OC}-FF product, 25 sccm silane flow was chosen for the further p-layer

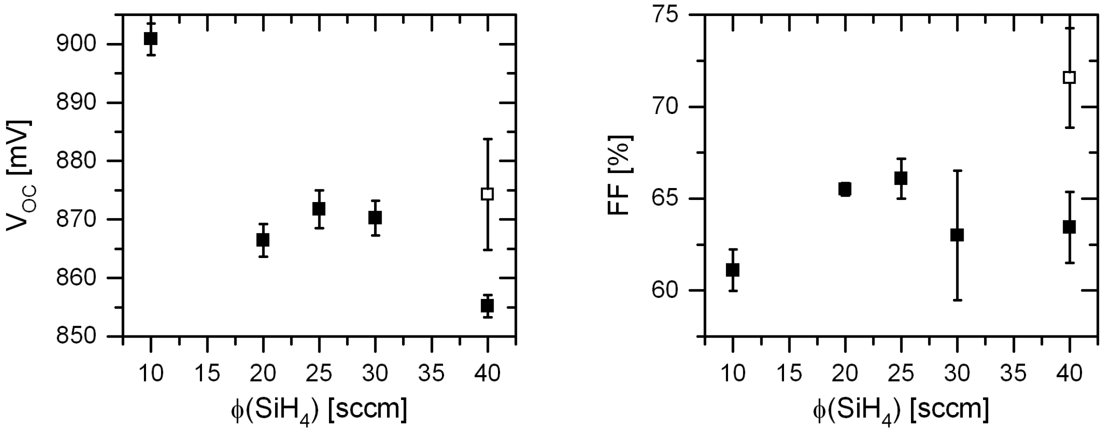

(a) Open circuit voltage.

(b) Fill factor.

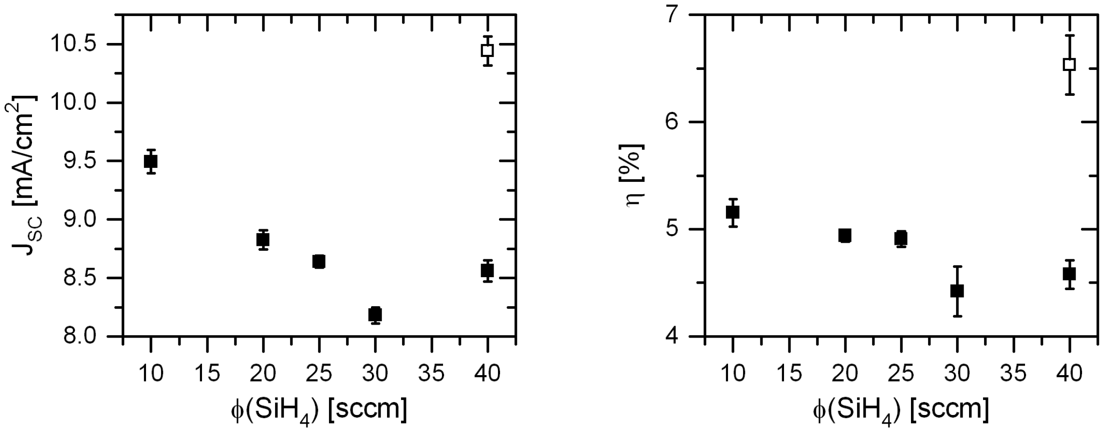

(c) Short circuit current.

(d) Efficiency.

Figure 4.14: IV parameters of a-SiO:H single cells against SiH_4 flow in the p-doped layer.

development.

4.2.3 B_2H_6 Flow Variation

The effective dopant concentration is important for the electrical performance of the p-a-SiO:H layers. Therefore, the B_2H_6 flow was varied. Figure 4.16 presents the Tauc bandgap of the p-a-SiO:H single layers. The open symbol represents the standard p-a-Si:H layer without oxygen. The Tauc bandgap first decreases with increasing B_2H_6 flow ratio but then remains constant. This trend is similar to the results of Inthisang et al. [73]. Boron and silicon have a lower dissociation energy than two silicon atoms [24]. Consequently, boron reduces the bandgap. Probably, the effectively bonded boron

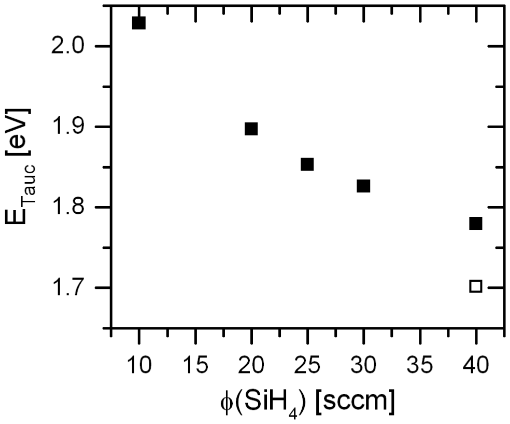

(a) Tauc bandgap.

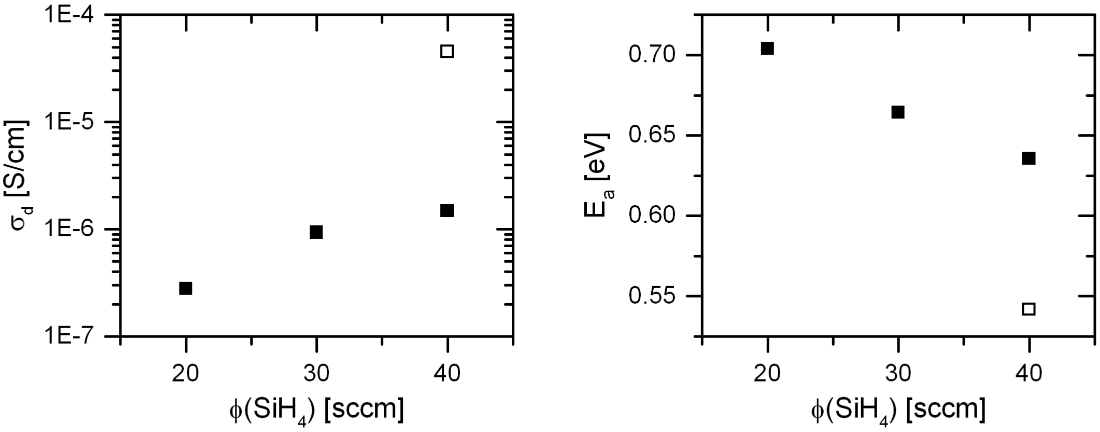

(b) Dark conductivity at room temperature.

(c) Activation energy.

Figure 4.15: Properties of p-a-SiO:H single layers against SiH_4 flow.

content saturates at higher B_2H_6 flow ratios, so the bandgap changes no further.

Single cells were prepared at varying B_2H_6 flow ratios in the p-a-SiO:H layers. The high bandgap intrinsic absorber layers were not optimised yet. The corresponding IV parameters are depicted in figure 4.17. The open circuit voltage tends to decrease with the B_2H_6 flow ratio in the p-layer like the Tauc bandgap in figure 4.16. The short circuit current stays more or less constant with some outliers. The fill factor exhibits a maximum at a flow ratio of $\phi(B_2H_6)/\phi(SiH_4) = 3$. An optimum of the B_2H_6 flow is expected. B_2H_6 introduces effective dopants which lower the activation energy and raise the conductivity [73, 74]. Yet, too much B_2H_6 incorporates more detrimental defects in the film [73]. The efficiency follows the trend of the fill factor so that the flow ratio of $\phi(B_2H_6)/\phi(SiH_4) = 3$ yields the best result.

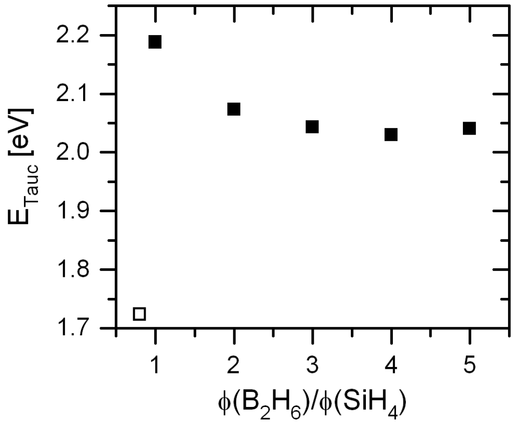

Figure 4.16: Tauc bandgap of p-a-SiO:H single layers against different flow ratios of B_2H_6 and SiH_4.

4.2.4 Hydrogen Dilution

There are reports in literature which claim that hydrogen dilution raises the optical bandgap of p-a-SiO:H while the electrical properties stay constant or are even improved to a certain extent [14, 73]. Consequently, the hydrogen flow was varied in the production of p-a-SiO:H layers and the corresponding single layer properties are depicted in figure 4.18. The open symbols represent the standard p-a-Si:H layer without oxygen. The Tauc bandgap of the layers is not influenced much by the hydrogen flow while the growth rate decreases as expected. Since the tail absorption superimposes the square root course of the absorption coefficient [33], the Tauc bandgap is probably underestimated for higher hydrogen flows.

Figure 4.19 depicts the IV parameters of single cells against hydrogen dilution in the alloyed p-layer. The high bandgap intrinsic absorber layers are optimised. Surprisingly, the open circuit voltage exhibits a maximum at medium hydrogen flow although the Tauc bandgap does not vary much with hydrogen dilution and is even lowest in this case (see figure 4.18a). The short circuit current also tends to increase with hydrogen flow. This underlines the idea, that the Tauc bandgap in figure 4.18a is underestimated for increasing hydrogen flows due to tail absorption.

Hydrogen dilution deteriorates the electrical properties of the p-doped layers. Therefore, the series resistance rises with the hydrogen flow leading to a small overall decrease of the fill factor (see figures 4.19e and 4.19b). Kim et al. [14] report reduced dark conductivity of p-a-SiO:H layers when the hydrogen dilution becomes too high. This could explain the increased series resistance in figure 4.19e. The efficiency as well as the open circuit voltage are highest for a hydrogen flow ratio of $\phi(H_2)/\phi(SiH_4) = 12$. At this flow ratio, a

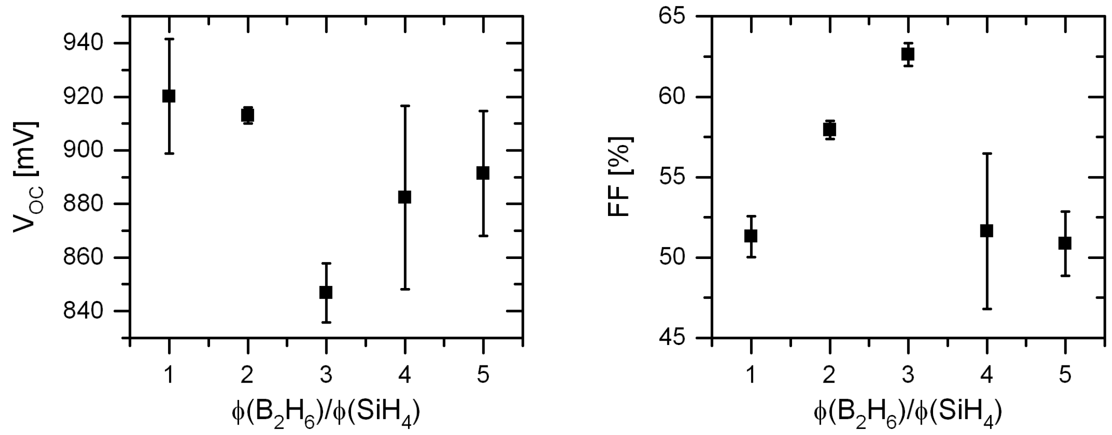

(a) Open circuit voltage.

(b) Fill factor.

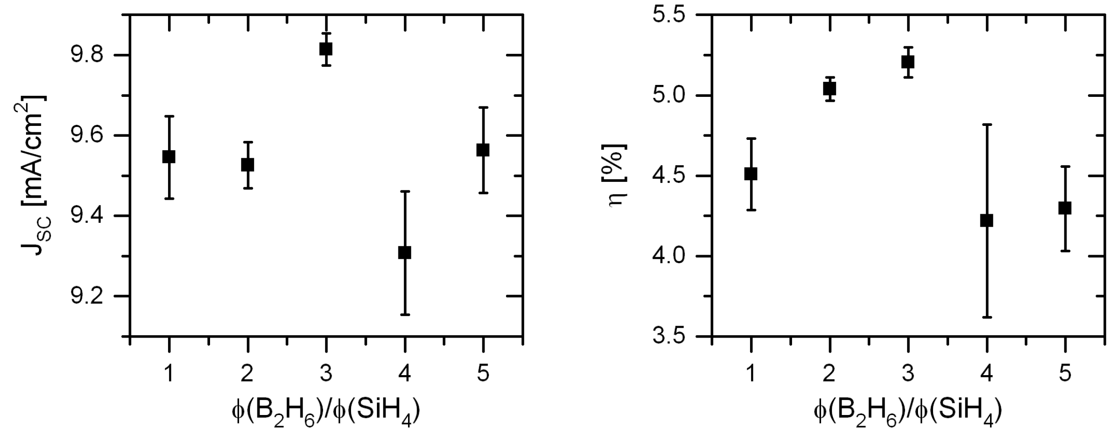

(c) Short circuit current.

(d) Efficiency.

Figure 4.17: IV parameters of a-SiO:H single cells against different flow ratios of B_2H_6 and SiH_4 in the p-doped layer.

trade-off between the benefits of a higher p-layer bandgap and reduced electrical quality is achieved.

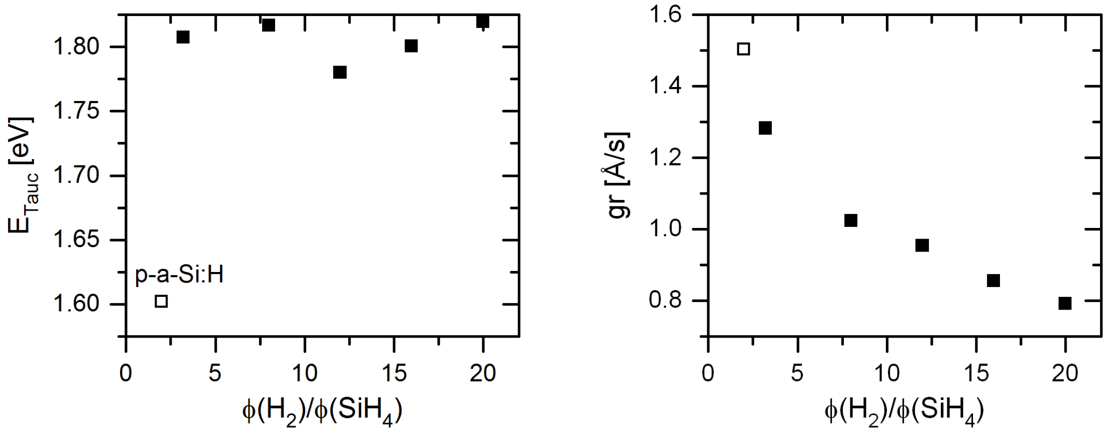

(a) Tauc bandgap.

(b) Growth rate.

Figure 4.18: Properties of p-a-SiO:H single layers against different flow ratios of H_2 and SiH_4.

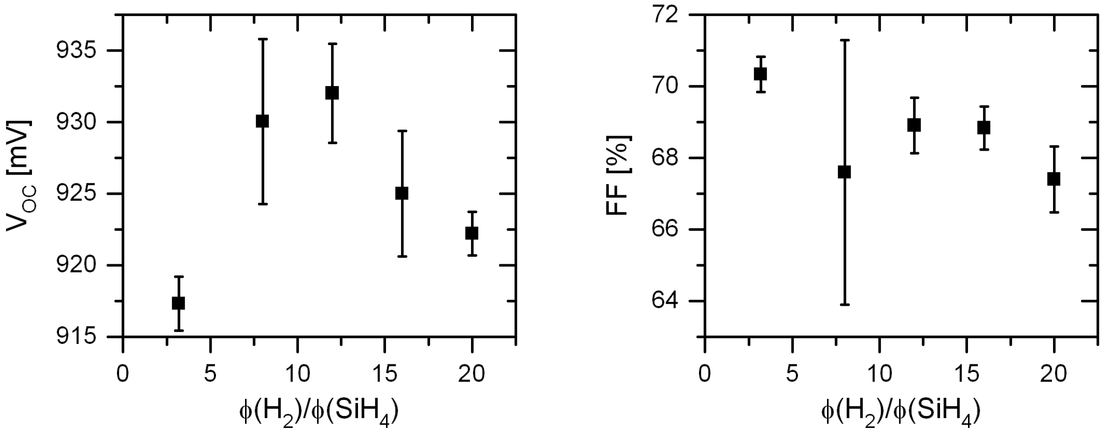

(a) Open circuit voltage. **(b)** Fill factor.

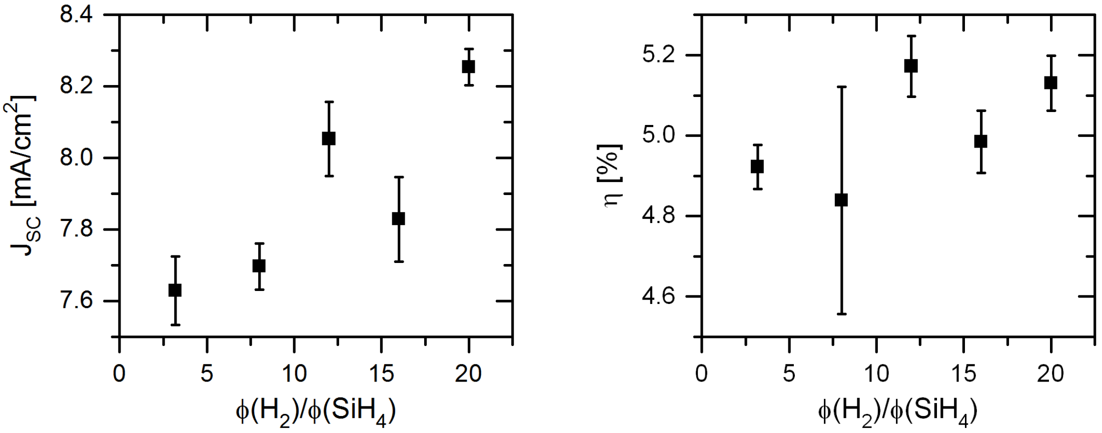

(c) Short circuit current. **(d)** Efficiency.

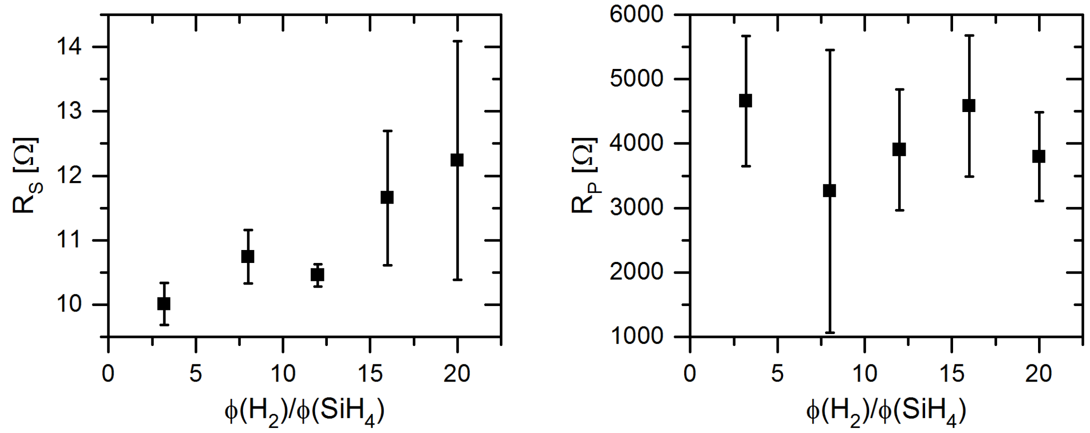

(e) Series resistance. **(f)** Parallel resistance.

Figure 4.19: IV parameters of a-SiO:H single cells against different flow ratios of H_2 and SiH_4 in the p-doped layer.

4.3 Conclusion

In this chapter, the process conditions leading to good material quality of high bandgap amorphous silicon alloys were investigated. The development of high bandgap absorber layers resulted in the following adjustments of the RF-PECVD process parameters. CO_2 was added only in small amounts ($\phi(CO_2)/\phi(SiH_4)= 0.25$), the ratio of hydrogen to silane was increased from 5 to 30 and the heater temperature was lowered from 220 to 180 °C. The total flow rate was increased from 240 sccm to 937 sccm to enable sufficient hydrogen dilution and fine tuning of all alloying process gases. Consequently, the best strategy for the development of an intrinsic high bandgap amorphous silicon alloy is to give hydrogen incorporation precedence over any other impurity. For this purpose, the substrate temperature has to be lowered. However, a low substrate temperatures reduces the surface reaction rate, which leads to porous material. In order to compensate this effect, the growth rate must be reduced. This can be done by raising the hydrogen dilution as well as lowering pressure and power. Therefore, following these trends of the process parameters resulted in the best high bandgap amorphous silicon absorbers.

The final properties of the high bandgap amorphous silicon p-layers were gained by finding a trade-off between the benefits of a higher p-layer bandgap and reduced electrical quality. The bandgap was raised by increasing the gas flow ratios of CO_2 and hydrogen. In order to optimise the ratio of B_2H_6, the SiH_4 flow was lowered. This way, a maximum of effective dopants is introduced into the film before the defect density becomes too high. The optimised deposition parameters of the high bandgap intrinsic and p-doped layers are presented in table 4.1.

	p-a-SiO:H	i-a-SiO:H
$\Phi(H_2)$ [sccm]	200	900
$\Phi(SiH_4)$ [sccm]	25	30
$\Phi(CO_2)$ [sccm]	50	3-20
$\Phi(B_2H_6)$ [sccm]	32	
P [W]	10	10
p [mbar]	0.3	1
d_{el} [mm]	25	15
T_{heater} [°C]	220	180

Table 4.1: Deposition parameters of high bandgap materials obtained by process development.

5

Comparison of N_2O, CO_2 and CH_4

Although many authors report the development of high bandgap amorphous silicon alloys for the application in multijunciton cells [10, 11, 13–15, 51, 72, 75], there are very few comparisons of different material types [9, 76]. Now that high bandgap intrinsic and p-doped layers with sufficient quality are available as a basic system, the question shall be answered, which source gas yields the best results in which functional layer. For this purpose N_2O, CO_2 and CH_4 are compared with respect to the resulting properties of intrinsic and p-doped layers as well as single cells. First of all, the optical Tauc bandgap is introduced as the common parameter for the comparison and its dependence on hydrogen, oxygen and carbon content is investigated. Then, the sample properties achieved with N_2O, CO_2 or CH_4 in the intrinsic layer are discussed. Finally, the same comparison of the process gases is applied to the p-doped layer.

5.1 Optical Tauc Bandgap in Dependence on Hydrogen, Oxygen and Carbon Content

The optical Tauc bandgap is reported to follow the behaviour of the mobility gap [77]. Thus, it was chosen to serve as a common variable for the comparison of sample properties achieved with different alloying source gases. The Tauc bandgap is influenced by the atomic concentration of the different species introduced by the varying flow of their source gases.

Figure 5.1a from [57] shows the carbon and oxygen atomic concentrations in i-a-SiO(C):H single layers for different flow ratios of either CH_4 or CO_2 with silane. The data was obtained from EBS measurements (see section 2.2.3). All concentrations exhibit a linear rising trend with increasing CH_4 or CO_2 flow ratio. Oxygen is incorporated more easily

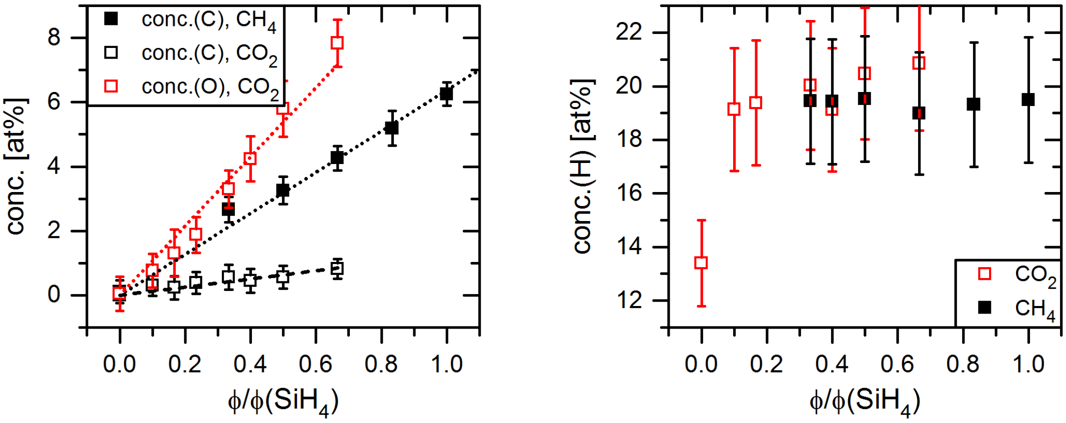

(a) C and O concentration from EBS [57]. **(b)** H concentration from FTIR.

Figure 5.1: Different atomic concentrations against CH_4 or CO_2 flow ratio with silane in amorphous silicon alloy single layers.

into the film by CO_2 than carbon by CH_4 since the oxygen concentration is almost twice as high as the carbon concentration at equivalent flow ratios. This is surprising, because the dissociation energy of CO_2 is higher than that of CH_4 (see table 2.1). Yet, according to Iftiquar [26], the reaction between the oxygen precursor OH and silicon is very strong, which could explain, why oxygen connects faster to the growing surface than carbon does. Although CO_2 also contains carbon, almost none of it is incorporated into the film within the error margin in agreement with other authors [9]. This might be explained by the CO-molecule taking a lot of energy to dissociate (749 to 1076.5 kJ/mol [24]) and being highly reactive with oxygen [26].

Figure 5.1b presents the hydrogen atomic concentration for different CO_2 or CH_4 flow ratios with silane. Within the errors of the FTIR spectroscopy evaluation the hydrogen concentration stays constant at about 20 at% irrespective of the gas flow ratio or the used process gas. Although the hydrogen concentration seems to increase slightly with the CO_2 flow ratio, this could also be an effect of oxygen backbonding to the Si-H stretching modes [40]. The backbonding effect of oxygen enhances the FTIR peak at $\nu = 2000\,\mathrm{cm}^{-1}$ where the hydrogen concentration was evaluated according to Lucovsky et al. [40]. The reference a-Si:H layer has a lower hydrogen content of about 13 at% because 6 times lower hydrogen dilution was used in its fabrication (see tables 2.2 and 2.3). The optimization of a high bandgap i-a-Si:H layer with high hydrogen content would have taken more development steps so the standard layer was used instead.

In figure 5.2, the optical Tauc bandgap is depicted against the carbon, oxygen and hydro-

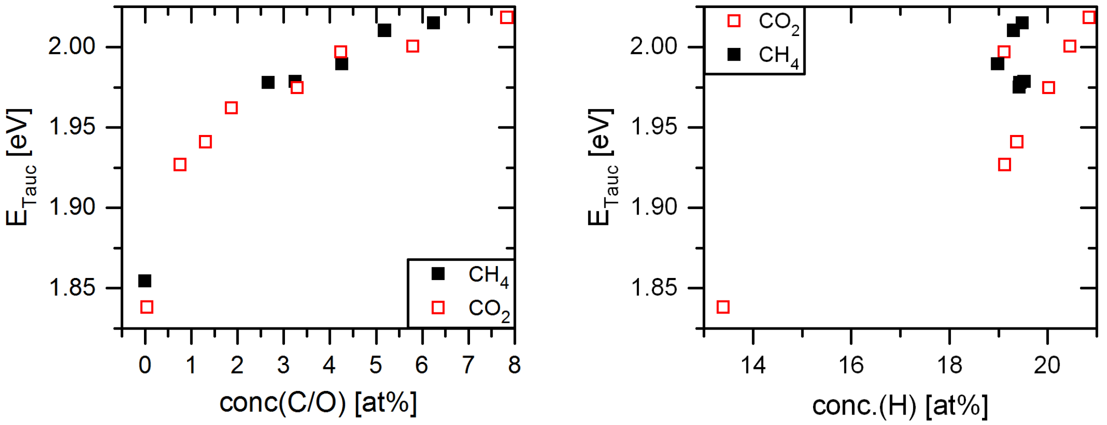

(a) E_{Tauc} against C or O concentration from EBS [57].

(b) E_{Tauc} against H concentration from FTIR.

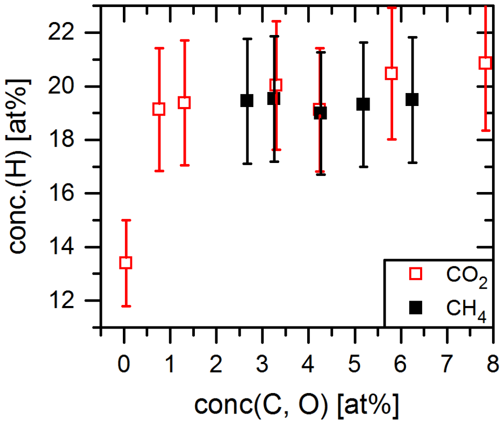

(c) H concentration from FTIR against C or O concentration from EBS.

Figure 5.2: Tauc bandgap energy and hydrogen concentration against atomic concentrations of different species for CH_4 or CO_2 in amorphous silicon alloy single layers.

gen concentrations depending on CH_4 or CO_2 as process gas. Figure 5.2a from [57] shows a first steep increase of the Tauc bandgap with the addition of carbon or oxygen. This is probably caused by the enhanced hydrogen content of the alloyed samples due to higher hydrogen dilution (see figure 5.2b). Hydrogen is reported to increase the bandgap of amorphous silicon and its alloys [78]. At constant hydrogen dilution the Tauc bandgap increases more moderately with the oxygen or carbon concentration (see figure 5.2a). This can be explained by lower bond lengths, higher binding energies and backbonding effects of oxygen or carbon with silicon [11, 24, 79].

Surprisingly, the Tauc bandgap shows almost no difference at equivalent concentrations of carbon and oxygen. Since oxygen has a higher binding energy with silicon than carbon, it is expected to produce a higher bandgap at equivalent concentrations [80]. One explanation for this discrepancy could be the hydrogen content. Hydrogen concentration has been reported to increase with carbon concentration but to decrease with oxygen concentration [81, 82]. So higher hydrogen concentration in the carbonated films could lead to the same Tauc bandgap as in the oxidised films although the carbon and oxygen concentrations are the same. The FTIR evaluation of the present samples shows that the hydrogen content seems to be rather higher than lower in the silicon oxide layers than in the silicon carbide layers. This contradicts the latter theory (see figure 5.2c). Yet, the hydrogen concentrations are the same within the errors independent of the alloying source gas. Moreover the backbonding of oxygen to the Si-H stretching modes might lead to an overestimation of the hydrogen concentration in the silicon oxide layers, as described above.

5.2 N_2O versus CO_2 in the Intrinsic Layer

One objective of this work is the comparison of different alloying source gases for the development of high bandgap amorphous silicon absorbers. As a first step, the two source gases containing oxygen, N_2O and CO_2, are compared to find out, which source gas is preferable for the incorporation of oxygen.

Figure 5.3 presents single layer properties of i-a-SiO:H alloys produced either with CO_2

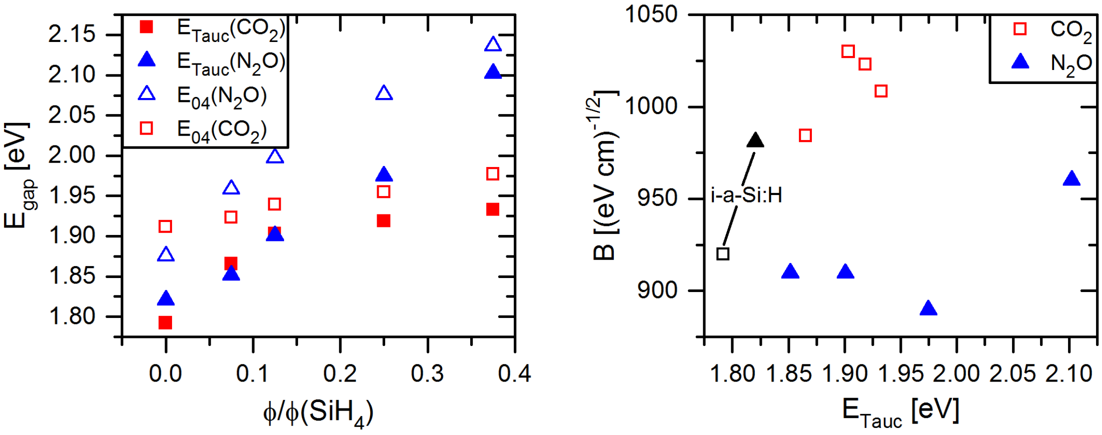

(a) Optical bandgap against gas flow ratio of N_2O or CO_2 with silane.

(b) Tauc slope parameter against Tauc bandgap.

Figure 5.3: Single layer properties of i-a-SiO:H films produced with CO_2 or N_2O.

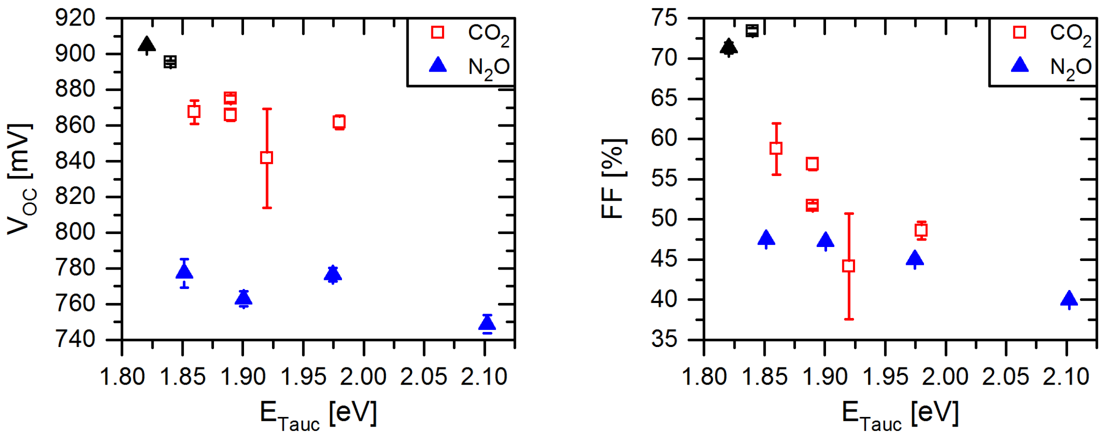

(a) Open circuit voltage. **(b)** Fill factor.

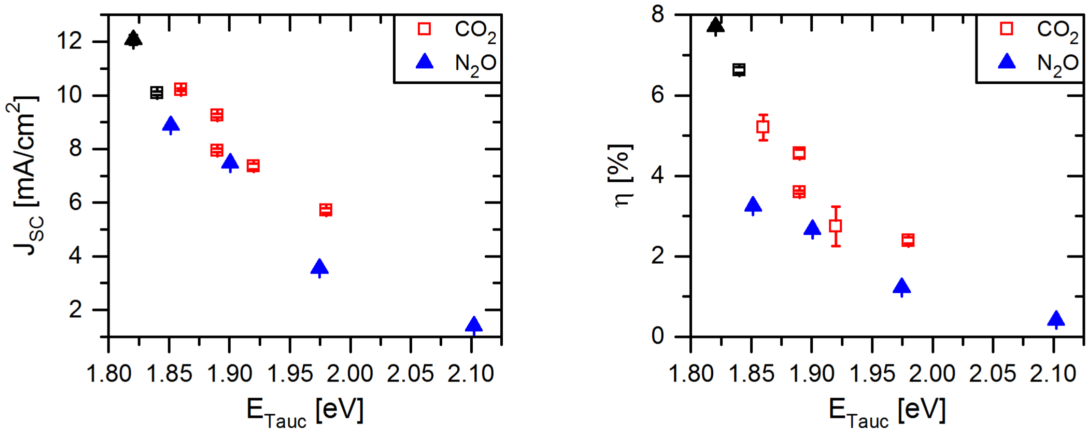

(c) Short circuit current. **(d)** Efficiency.

Figure 5.4: IV parameters of a-SiO:H single cells produced with CO_2 or N_2O against Tauc bandgap.

or N_2O. While the optical Tauc bandgap rises linearly with the N_2O flow ratio, it saturates at high CO_2 flow ratios (see figure 5.3a). At low gas flow ratios, the Tauc bandgap achieved with CO_2 or N_2O is similar. The Tauc slope parameter B in figure 5.3b is higher when CO_2 is used, indicating a steeper rise of the absorption coefficient with energy and better material quality. Yet, the black data points at the lowest Tauc bandgaps differ considerably, although they represent i-a-Si:H reference layers produced with the same standard recipe. So the Tauc slope parameter fluctuates a lot.

In figure 5.4, the IV parameters of a-SiO:H single cells, produced either with CO_2 or N_2O in the p- and i-layer, are depicted. For the cells prepared with CO_2 or N_2O different TCO substrates, different p-layers and different i-layer process parameters were used (see table 5.1). Thus, the comparison of the IV parameters is difficult. The black data points

	CO_2-conditions		N_2O-conditions	
substrate	NSG		Asahi VU	
layer	p-a-SiO:H	i-a-SiO:H	p-a-SiO:H	i-a-SiO:H
$\Phi(H_2)$ [sccm]	80	200	80	600
$\Phi(SiH_4)$ [sccm]	40	40	40	40
$\Phi(CO_2)$ [sccm]	55	0-30		
$\Phi(N_2O)$ [sccm]			30	0-15
$\Phi(B_2H_6)$ [sccm]	32		50	
P [W]	10	10	10	20
p [mbar]	0.3	1	0.3	1
d_{el} [mm]	25	15	25	20
T_{heater} [°C]	220	220	220	220

Table 5.1: Deposition parameters of high bandgap cell component layers produced with CO_2 or N_2O.

in figure 5.4 represent reference cells deposited either under CO_2- or N_2O-conditions but with the same i-a-Si:H absorber and cell thickness of 250 nm. The N_2O-conditions lead to higher open circuit voltage and short circuit current of the reference cell compared to the CO_2-conditions. The fill factors of the reference cells are similar for the CO_2- and N_2O-conditions. Consequently, the different substrate and p-layer support the performance of the cells deposited under N_2O-conditions. The process parameters of the intrinsic layers were not optimised, so all IV parameters deteriorate drastically with increasing Tauc bandgap. Cells produced with CO_2 exhibit higher open circuit voltage, fill factor and short circuit current than the cells produced with N_2O in spite of the inferior p-layer and substrate. Explanations for these observations are given in section 5.5. In summary, CO_2 appears to be more suitable for the production of high bandgap absorber alloys than N_2O.

5.3 CH_4 versus CO_2 in the Intrinsic Layer

After identifying CO_2 to be preferable over N_2O as a source gas for high bandgap absorber layers, the question arises whether CH_4 could be superior to CO_2 for the same purpose. Figure 5.5 shows single layer properties of amorphous silicon carbide and amorphous

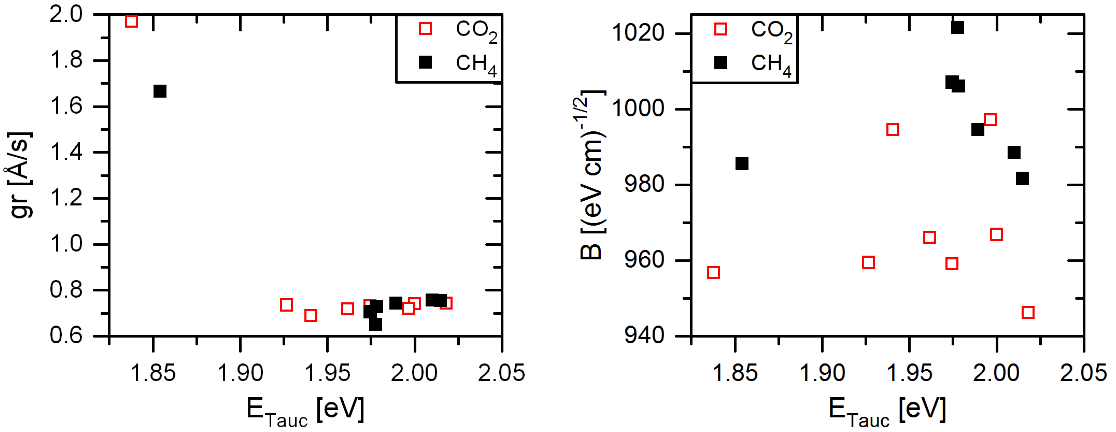

(a) Growth rate. **(b)** Tauc slope parameter.

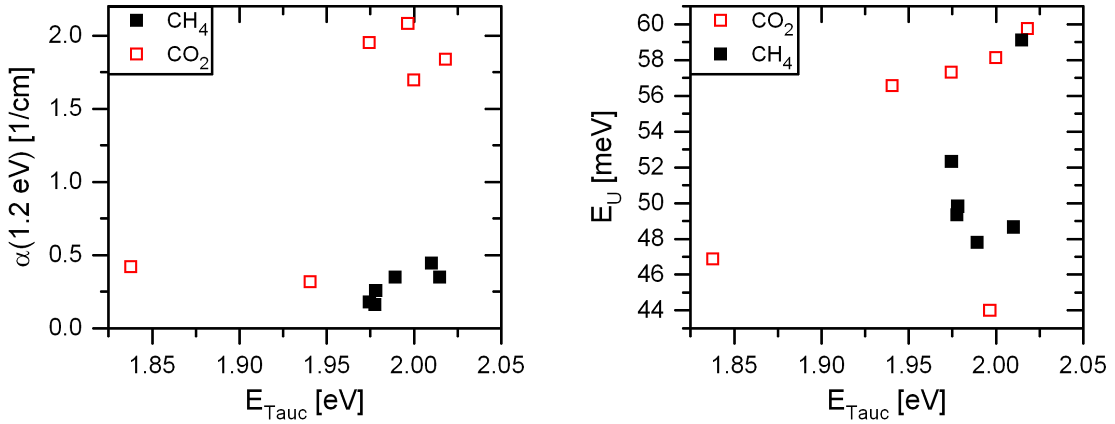

(c) Defect absorption coefficient at 1.2 eV. **(d)** Urbach energy.

Figure 5.5: Growth rate and optical properties of amorphous silicon carbide and silicon oxide single layers produced with CH_4 or CO_2 against Tauc bandgap.

silicon oxide produced with CH_4 or CO_2 against the Tauc bandgap. The data points at the lowest Tauc bandgaps around 1.85 eV represent standard i-a-Si:H layers without oxygen or carbon.

The growth rate in figure 5.5a depends neither on the kind, nor on the amount of the alloying source gas but on the hydrogen dilution, which is six times higher for the alloys than for the standard i-a-Si:H layers. The Tauc slope parameter is expected to decrease with rising Urbach energy [31]. However, it does not show any clear trend with rising Tauc bandgap and even varies for the two standard i-a-Si:H layers prepared with the same recipe (see figure 5.5b). Nevertheless, the Tauc slope parameter tends to be higher when CH_4 is used instead of CO_2.

Apart from one outlier, the Urbach energy of samples produced with CO_2 increases monotonously with the Tauc bandgap (see figure 5.5d). It takes lower values when CH_4 is employed, but does not show any clear trend with the Tauc bandgap. Similarly, Shimizu et al. [12] found that oxygen and nitrogen increase the Urbach energy of a-Si:H more than carbon at equivalent concentrations. Desalvo et al. prepared amorphous silicon carbide samples with an Urbach energy of approximately 43 meV at a bandgap of E_{04} = 2.1 eV [10]. As depicted in figure 5.5d, an Urbach energy of 49 meV was reached with amorphous silicon carbide at a similar bandgap energy. The absorption coefficient at the energy of 1.2 eV was measured by CPM and UV-VIS spectroscopy. It represents deep defect absorption and is depicted in figure 5.5c. Whereas the samples prepared with CH_4 show more or less constant defect absorption in the range of the i-a-Si:H standard layer, most of the samples prepared with CO_2 take higher values.

In figure 5.6 FTIR spectra and the microstructure factor of i-a-SiO:H and i-a-SiC:H single layers are depicted. The peak area of the Si-O-Si stretching modes around $\nu = 1000\,\mathrm{cm}^{-1}$ increases with the Tauc bandgap indicating an enhanced oxygen content as determined by EBS (see figures 5.1a and 5.6a). Si-O-Si stretching modes modified by one to three backbonded oxygen atoms (-O_n) dominate the absorption peak around $\nu = 1000\,\mathrm{cm}^{-1}$. Consequently, since the oxygen concentration is low (see figure 5.1a), oxygen is accumulated in certain regions leading to an inhomogeneous material. In contrast, no clear evidence of carbon clustering is found in the FTIR spectrum of amorphous silicon carbide in figure 5.6b.

The peak area of the hydrogen stretching modes around $\nu = 2000\,\mathrm{cm}^{-1}$ is shifted to higher wavenumbers for the amorphous silicon oxide samples than for the amorphous silicon carbide samples at comparable Tauc bandgaps (compare figures 5.6a and 5.6b). Therefore, CO_2 appears to introduce more polyhydrogen bonds than CH_4. Polyhydrogen bonds with carbon are neglected, however. The evaluation of the microstructure factor, which determines the fraction of polyhydrogen stretching modes related to all hydrogen stretching modes in the FTIR spectrum, is shown in figure 5.6c from [57]. The microstructure factor rises with the addition of alloying source gases compared to the standard i-a-Si:H layer at the lowest Tauc bandgap. The increase of microstructure with alloying has been observed by several authors [14, 41, 42]. Kim et al. achieved a microstructure factor of 0.23 with amorphous silicon oxide at a bandgap of $E_{04} \approx 2.07$ eV [14]. Stuckelberger et al. obtained a microstructure factor of 0.17 for pristine a-Si:H at a bandgap of $E_{04} \approx 1.99$ eV [54]. Figure 5.6c shows that with CH_4 a microstructure factor close to the latter value (0.18) can be achieved even at a slightly higher bandgap energy. The microstructure factor of the amorphous silicon oxide layers rises more steeply with the bandgap

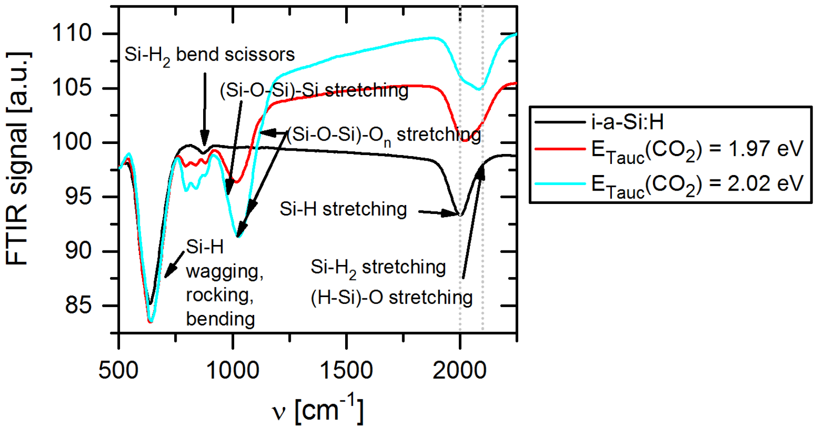

(a) FTIR spectra of i-a-SiO:H single layers.

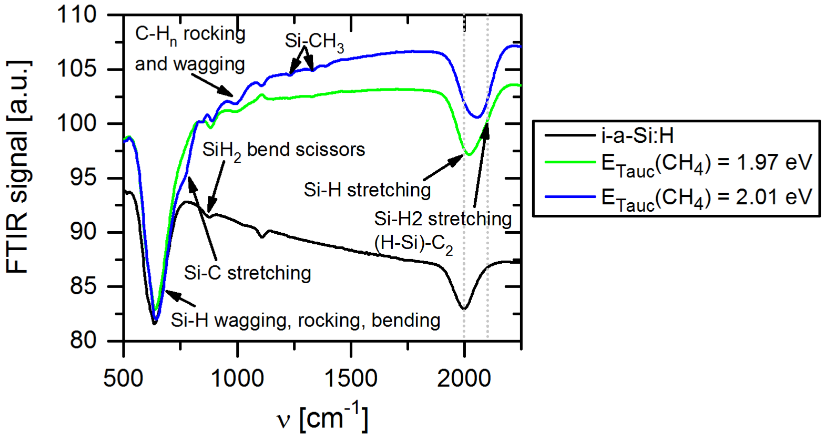

(b) FTIR spectra of i-a-SiC:H single layers.

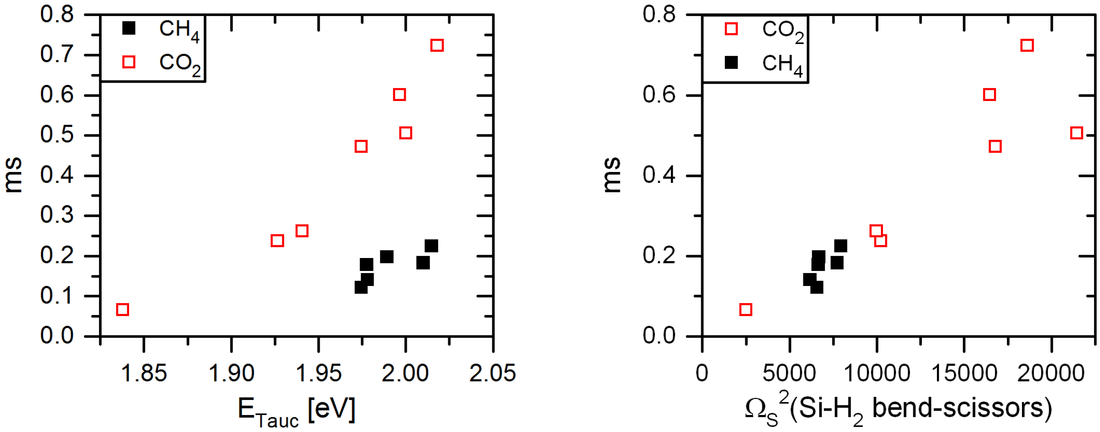

(c) Microstructure factor against Tauc bandgap [57].

(d) Microstructure factor against squared absorption strength of the $Si-H_2$ bend scissors FTIR mode.

Figure 5.6: FTIR spectra and microstructure factor of amorphous silicon carbide and silicon oxide single layers produced with CH_4 or CO_2.

and takes much higher values than the microstructure factor of the silicon carbide layers. The evaluation of the microstructure factor is difficult in the case of amorphous silicon alloys. Backbonding effects of carbon or oxygen can shift the monohydrogen stretching modes in the FTIR spectrum to higher wavenumbers and confuse them with the polyhydrogen stretching modes [40, 60] (see also figures 5.6a and 5.6b). Therefore, in figure 5.6d, the microstructure factor is depicted against the squared absorption strength of the $Si{-}H_2$ bend scissors FTIR mode at $\nu = 880\,\mathrm{cm}^{-1}$. The relationship between the two quantities is quite linear for most data points, which confirms, that the microstructure factor really describes the fraction of the polyhydrogen modes. At high oxygen concentrations, the microstructure factor deviates from the linear relationship since the polyhydrogen stretching modes are overestimated due to oxygen backbonding effects.

The electrical properties of amorphous silicon carbide and oxide single layers produced with CH_4 or CO_2 are depicted against the Tauc bandgap in figure 5.7. For both source gases, dark and photoconductivity at room temperature decrease at higher Tauc bandgaps (see figure 5.7a from [57]). However, the photoconductivity of the samples produced with CO_2 is larger than of samples produced with CH_4. This agrees with Haga et al. [76] and Fujikake et al. [9], who report one order of magnitude higher photoconductivity of a-SiO:H than of a-SiC:H at equivalent bandgaps. One might attribute the higher photoconductivity of amorphous silicon oxide to better material quality. Yet, this contradicts the previous findings about the optical properties in figures 5.5 and 5.6. Fujikake et al. also measured the spin densities of amorphous silicon oxide and amorphous silicon carbide films. Amorphous silicon oxide exhibited only slightly lower spin density values than amorphous silicon carbide, which cannot explain the differences in photoconductivity [9]. Yet, according to Beck et al. [83], photoconductivity is not a good measure for material quality, if the material is not truly intrinsic. In figure 5.7a from [57], the dark conductivity of amorphous silicon carbide is also lower than of amorphous silicon oxide and comes closer to the ideal curve, where the activation energy equals half the Tauc bandgap:

$$\sigma_d(\mathrm{ideal}) = \sigma_0 exp\left[-0.5\frac{E_{Tauc}}{kT}\right]. \tag{5.1}$$

In analogy to Wang et al. [84], the conductivity prefactor σ_0 was kept constant. It was adjusted, so that the ideal dark conductivity matches the values of the standard i-a-Si:H samples at the lowest Tauc bandgaps.

The photosensitivity describes the quotient of photo- and dark conductivity and is quite

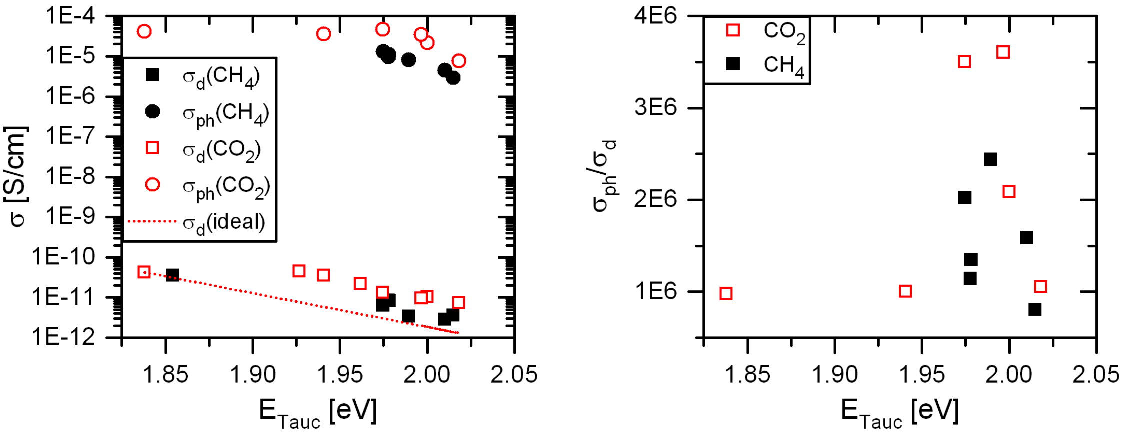

(a) Planar horizontal conductivity [57]. **(b)** Photosensitivity.

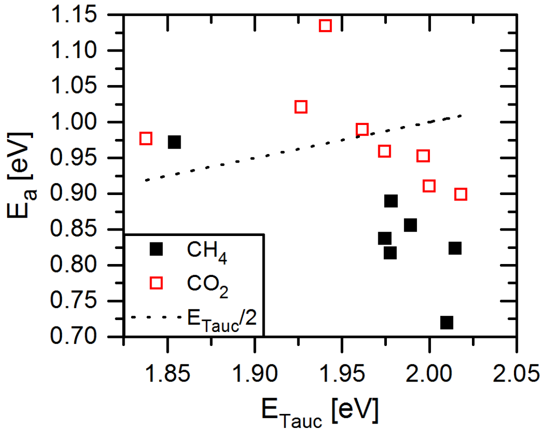

(c) Activation energy.

Figure 5.7: Electrical properties of amorphous silicon carbide and silicon oxide single layers produced with CH_4 or CO_2 against Tauc bandgap.

similar for samples produced with CH_4 or CO_2 within the expected uncertainties (see figure 5.7b). The highest photosensitivity of 3.6×10^6 is achieved with CO_2 at a Tauc bandgap of 2 eV. This is slightly lower than the values reported in literature. Inthisang et al. [13, 85] obtained a photosensitivity of about 7×10^6 for a-SiO:H at a Tauc bandgap of approximately 1.89 eV. Desalvo et al. developed an amorphous silicon carbide layer with a photosensitivity of $\sigma_{ph}/\sigma_d \approx 10^7$ at a bandgap of $E_{04} \approx 2.1\,\mathrm{eV}$ [10]. So, it is not completely clear, if amorphous silicon carbide or amorphous silicon oxide yields higher photosensitivity at equivalent bandgaps.

One explanation for the observed differences in photo- and dark conductivity of amorphous silicon oxide and carbide could be the n-type doping effect of oxygen enhancing the effective electron mobility in the material and therefore also conductivity. Shimizu et al. [12] and Morimoto et al. [86] observed higher dark conductivity when nitrogen or oxygen impurities were added to amorphous silicon than when carbon was added. They explain this behaviour by positively charged N_4^+ and O_3^+ impurities acting as donors. If the higher conductivity values of the amorphous silicon oxide samples are caused by n-type doping in contrast to amorphous silicon carbide, the activation energy of amorphous silicon oxide is expected to be lower. Surprisingly, the opposite is demonstrated in figure 5.7c. Amorphous silicon carbide samples show lower activation energies than amorphous silicon oxide samples. The activation energies of the amorphous silicon oxide samples even rise above the line marking the intrinsic case, where the activation energy equals half the Tauc bandgap. Unlike the conductivity, the activation energy was not measured at room temperature but at varying higher temperatures. Since the activation energy E_a and the conductivity prefactor σ_0 can be temperature dependent [68], this might explain the inconsistencies in figure 5.7c.

The single layer results in figures 5.5 and 5.6 favour CH_4 over CO_2. Now, the question arises, if a mixture of carbon and oxygen can annihilate the defects introduced by the other atom type respectively and relax the network further. Therefore, the influence of both, CH_4 and CO_2, on the properties of intrinsic layers was investigated. Figure 5.8 presents single layer properties of amorphous silicon alloys produced with a mixture of CO_2 and CH_4. The total gas flow of the alloying source gases varied between 7 and 15 sccm. The single layer results are depicted in dependence on the share of CO_2 in the total gas flow of alloying source gases. Consequently, the alloy gas composition changes from pure CH_4 on the left to pure CO_2 on the right. The open symbols represent standard i-a-Si:H.

As can be deduced from figure 5.8a, the optical Tauc bandgap stays constant at about 1.88 eV for almost all alloy gas compositions. The photoconductivity was measured with a blue LED lamp at room temperature in this case. The same values were achieved for the standard i-a-Si:H layer and the composition containing only CH_4 at a CO_2 flow ratio of zero (see figure 5.8b). When CO_2 is added, the photoconductivity increases by an order of magnitude and then stays constant. The dark conductivity also increases with the CO_2 flow ratio. As described before, n-type doping by oxygen (O_3^+) can raise the photo- and dark conductivity of samples prepared with CO_2. Yet, the dark conductivity increases less abruptly with the addition of CO_2 than the photoconductivity. Consequently, the photosensitivity in figure 5.8c shows a maximum for a low CO_2 flow ratio of 0.2. The photosensitivities caused by a pure CH_4 or CO_2 composition are quite comparable as in figure 5.7b.

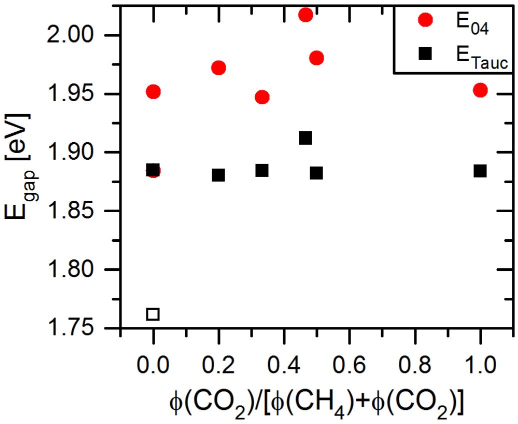

(a) Optical bandgap.

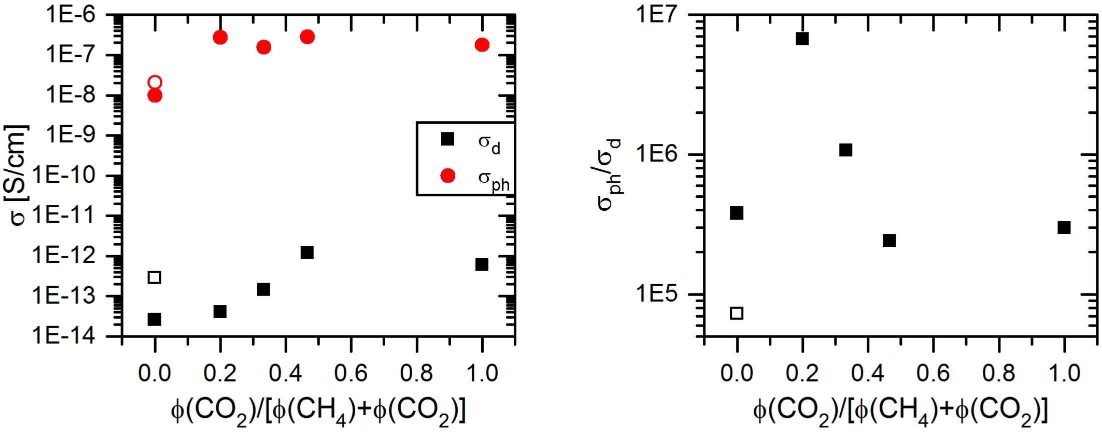

(b) Dark and photoconductivity at room temperature.

(c) Photosensitivity at room temperature.

Figure 5.8: Single layer properties of amorphous silicon alloys produced with a mixture of CO_2 and CH_4 at different CO_2 ratios.

Figure 5.9 presents the IV parameters of single cells prepared with the intrinsic layers discussed above. The open symbols represent a cell with the i-a-Si:H standard absorber. Just like the Tauc bandgap in figure 5.8a, the short circuit current remains constant for all alloy gas compositions. Disregarding the reference cell, the fill factor is maximal at the same alloy gas composition as the photosensitivity in figure 5.8c. Otherwise, the fill factor takes similar values for all alloy gas compositions within the errors. The main trend is expressed by the open circuit voltage which decreases monotonously with the CO_2 fraction in the alloy gas composition. Consequently, the open circuit voltage is about 60 mV higher for the pure CH_4 composition than for the pure CO_2 composition (see figure 5.9a). The resulting cell efficiency is highest (5 %) if only CH_4 or just a small

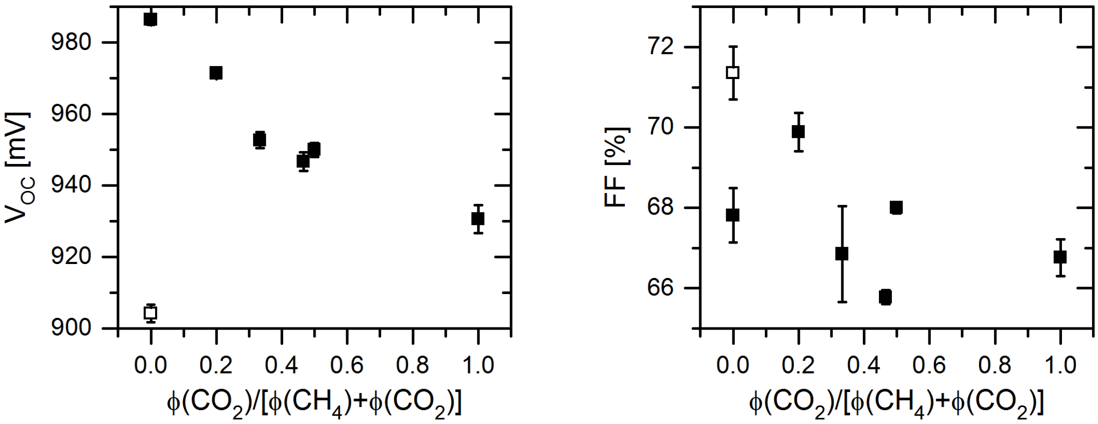

(a) Open circuit voltage. **(b)** Fill factor.

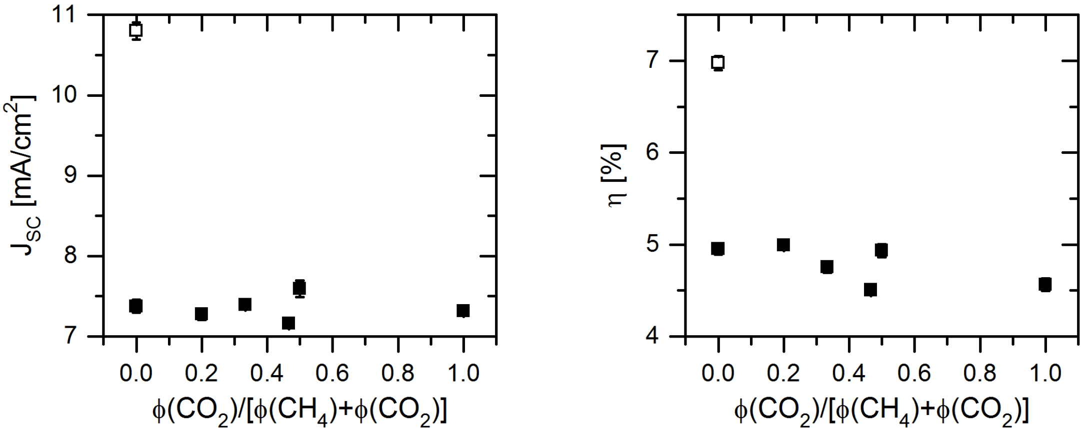

(c) Short circuit current. **(d)** Efficiency.

Figure 5.9: IV parameters of a-SiO(C):H single cells produced with a mixture of CO_2 and CH_4 at different CO_2 ratios in the i-layer.

fraction of CO_2 is used. The difference in the cell efficiencies achieved with the pure CO_2 or CH_4 composition is about 0.5 % at the same Tauc bandgap.

The previous results indicate that the use of pure CH_4 or a mixture with a small fraction of CO_2 is favourable for the alloying of intrinsic absorber layers. To investigate these relations further, single layers and cells were produced with a mix of a constant small CO_2 flow ratio ($\phi(CO_2)/\phi(SiH_4) = 0.1$) and varying CH_4 flow ratios in the same layers. In figure 5.10, single layer properties of intrinsic amorphous silicon alloys are compared using either pure CH_4 or a mixture with a constant low CO_2 flow ratio during preparation. As depicted in figure 5.10a, the carbon content increases linearly with the CH_4 flow ratio and is the same for the use of pure CH_4 and the alloy gas mix. The oxygen content of

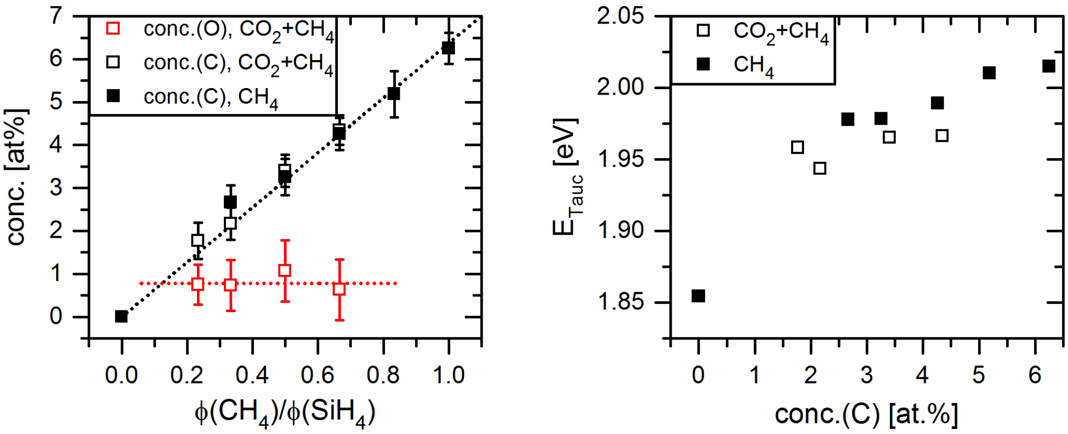

(a) C and O concentration from EBS against CH_4 flow ratio with silane.

(b) Tauc bandgap against carbon concentration from EBS.

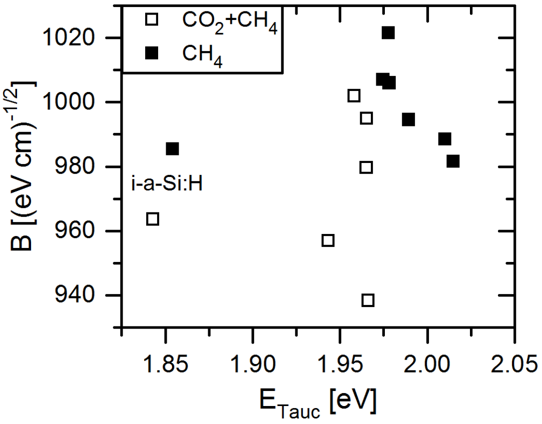

(c) Tauc slope parameter against Tauc bandgap.

Figure 5.10: Single layer properties of intrinsic amorphous silicon alloys produced with a mixture of CH_4 and a small constant amount of CO_2 ($\phi(CO_2)/\phi(SiH_4) = 0.1$). Comparison with layers alloyed only with CH_4 in dependence on the ratio of CH_4 with silane.

layers produced with the alloy gas mix stays at a constant low value below 1 at%. This concentration is similar to the result obtained with pure CO_2 at the same low flow ratio (compare to figure 5.1a). So, the alloy gas mix produces the same carbon and oxygen concentrations as if the gases were used separately at equivalent flow ratios.

The Tauc bandgap in figure 5.10b rises with the carbon content, but takes lower values for the alloy gas mix. This is surprising, because the additional oxygen content should raise the bandgap and not lower it. Possibly, the different Tauc bandgaps can be explained by higher hydrogen content of the samples prepared only with CH_4. Moreover, if an

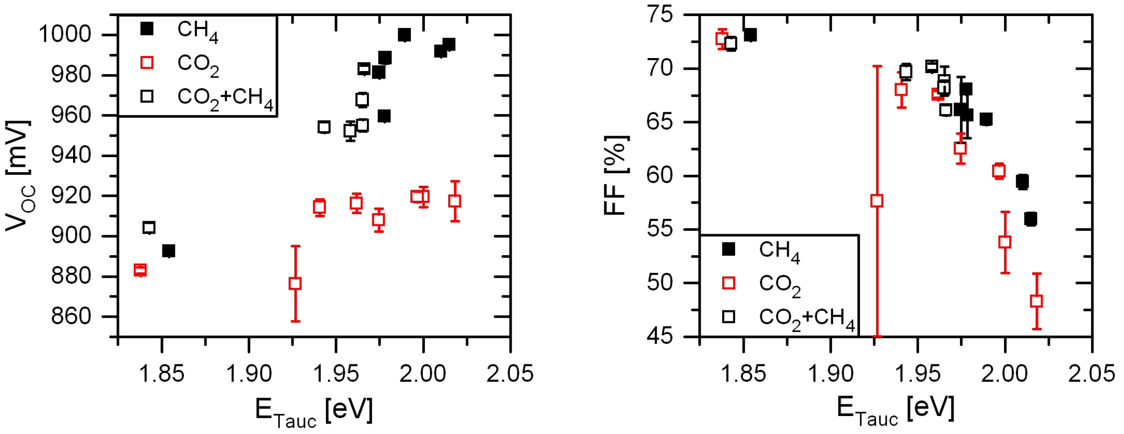

(a) Open circuit voltage.

(b) Fill factor.

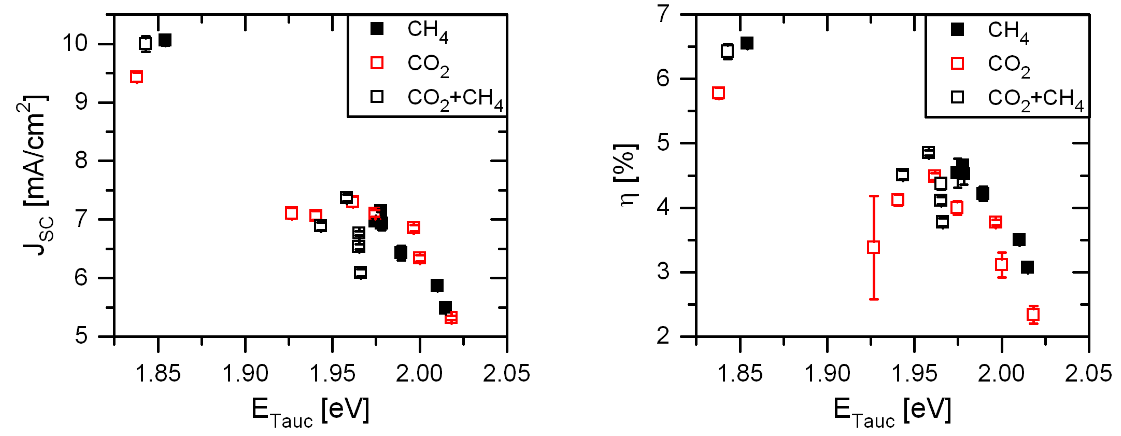

(c) Short circuit current.

(d) Efficiency.

Figure 5.11: IV parameters of a-SiO(C):H single cells produced with CO_2 or CH_4 and a mixture of CO_2 and CH_4 in the i-layer.

increasing number of carbon atoms connects to the same silicon atom, the bandgap rises even at a fixed carbon concentration [87]. Yet, the difference in the Tauc bandgaps of samples prepared with the gas mix or pure CH_4 is quite small and lies within the uncertainties of the bandgap and carbon content evaluations.

The Tauc slope parameter in figure 5.10c is slightly higher when pure CH_4 is used instead of the gas mix. However, one has to acknowledge that even the Tauc slope parameters of the two reference i-a-Si:H samples differ and are lower than those of the average alloy.

Figure 5.11 shows the IV parameters of amorphous silicon alloy single cells prepared either with CH_4, CO_2 or a combination CO_2+CH_4 in the intrinsic layer. For the alloy gas mix, a constant low CO_2 flow ratio of $\phi(CO_2)/\phi(SiH_4) = 0.1$ was used. Just like before, the biggest difference can be seen in the open circuit voltage which is higher for samples prepared with CH_4. While the open circuit voltage of samples prepared only with CO_2 remains constantly low, the open circuit voltage of samples prepared with CH_4 rises with the bandgap. It reaches a maximum of 1000 mV at a Tauc bandgap of 1.99 eV. In the case CO_2 the open circuit voltage is lower by 80 mV at an equivalent bandgap. The fill factor decreases with the bandgap for all gas compositions but takes a little higher values when CH_4 is used. The short circuit current drops with the bandgap. It is comparable for most gas compositions independent of the alloy. Only a few values obtained with the alloy gas mix are a bit lower.

While the photosensitivity in figure 5.8c and the fill factor in figure 5.9b suggest a slightly better performance of the alloy gas mix with a small amount of CO_2, this could not be reproduced by the results in figures 5.10 and 5.11. The fill factor in figure 5.11b takes higher values for the gas mix than for CH_4. Yet, this difference is caused by the lower bandgap energy obtained with the gas mix. Accordingly, the open circuit voltage of the cells produced with the gas mix is lower than when CH_4 is employed. Therefore, the performance of the alloy gas mix is not expected to be superior to using only CH_4 at equivalent bandgaps.

As observed in figure 5.9d, the efficiency in figure 5.11d is also higher by about 0.5 % when CH_4 is used instead of CO_2. The best amorphous silicon alloy single cell, prepared with CH_4 in the 200 nm thick absorber layer, shows an initial single cell efficiency of 4.95 % at an i-layer bandgap of 1.88 eV (see figures 5.8a and 5.9). The remaining IV parameters are: $V_{OC} = 986\,\mathrm{mV}$, FF = 68 % and $J_{SC} = 7.38\,\mathrm{mA/cm^2}$ (see figure 5.9). The highest open circuit voltage of 1000 mV is achieved with CH_4 at a Tauc bandgap of 1.99 eV and a fill factor of 65 % (see figure 5.11). This still leaves room for improvement. Ma et al. achieved an efficiency of 7.2 %, an open circuit voltage of 1.036 V, a fill factor of 72 % and a short circuit current of 9.66 $\mathrm{mA/cm^2}$ with amorphous silicon carbide as a single cell absorber [15]. Kim et al. [14] presented an a-SiO:H single cell with an efficiency of 7.83 %, an open circuit voltage of 1.042 V, a fill factor of 73 % and a short circuit current of 10.3 $\mathrm{mA/cm^2}$. Stuckelberger et al. showed that, even with a simple i-a-Si:H absorber, the open circuit voltage of a single cell can be raised to 1.04 V [62].

According to the results of this work, it can be concluded, that CH_4, when used in the intrinsic layer, leads to better optical single layer results (see figures 5.5 and 5.6) and higher open circuit voltage (see figure 5.11a) than CO_2. A transition from pure CH_4 to pure CO_2 in a mixture of both source gases confirms the deteriorating trend towards CO_2 (see figure 5.9). Thus, a mixture with a low CO_2 and high CH_4 fraction is not remarkably superior to using only CH_4 as can be seen in figure 5.11. Possible reasons for all these observations are discussed in section 5.5.

5.4 N_2O versus CO_2 versus CH_4 in the p-doped Layer

In the previous sections, it was established that CH_4 produces better material quality of high bandgap intrinsic amorphous silicon alloys than N_2O and CO_2. However, p-doped layers differ from intrinsic layers with respect to the requirements for good material quality. While intrinsic layers should have a low defect density and microstructure, doped layers need sufficient conductivity and high transparency. Moreover, the quasi Fermi level of the holes can only be lowered to the extremes given by the absorber if the p-doped emitter layer has a corresponding high bandgap too. Consequently, the bandgap of the p-doped layer has to be increased as well, aiming for the best trade-off between transparency, conductivity and Fermi level splitting. According to the simulation results in section 3.3, the optimal p-layer bandgap exceeds the following i-layer bandgap by 0.25 eV.

There are numerous studies dealing with p-doped silicon carbide or oxide in the amorphous or microcrystalline form [14, 60, 70, 72, 74, 76, 88–91]. However, there are not so many reports about the comparison of p-doped amorphous silicon carbide and oxide [9, 92]. Now the question arises, which alloying source gas is suited best for the high bandgap p-doped amorphous silicon layer.

Figure 5.12 shows single layer properties of high bandgap p-doped amorphous silicon alloys produced with N_2O, CO_2 or CH_4. The results of the p-doped layers prepared with N_2O were kindly provided by Alex Neumüller from NEXT ENERGY and are partly published in [93]. The optical Tauc bandgap in figure 5.12a rises linearly with the flow ratio of any alloying source gas but most steeply for N_2O. While carbon from CO_2 is barely incorporated into the film (see figure 5.1a), oxygen and nitrogen both have the effect of widening the bandgap. Moreover, N_2O is dissociated more easily than CO_2 (see table 2.1), which might increase the bandgap by enhanced oxygen incorporation. As observed before, CO_2 and CH_4 do not differ much with respect to bandgap widening although the points related to CO_2 in figure 5.12a are slightly higher than those related to CH_4. Whereas the growth rate rises with the Tauc bandgap for N_2O, it decreases for CO_2 and CH_4. One reason for this observation could be that N_2O is split more easily than CO_2 due to its lower dissociation energy (see table 2.1). The electronegativity of oxygen promotes further reactions [25, 26]. CH_4 and CO_2 do not dissociate easily [26, 79]. At low flow ratios of silane, their presence simply reduces the fraction of silicon growth precursors and consequently the growth rate.

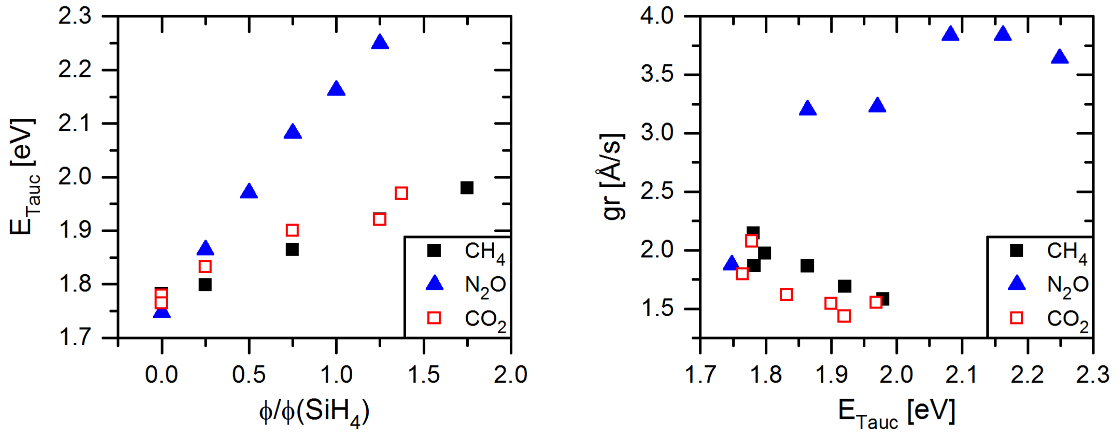

(a) Tauc bandgap against flow ratio with silane. **(b)** Growth rate against Tauc bandgap.

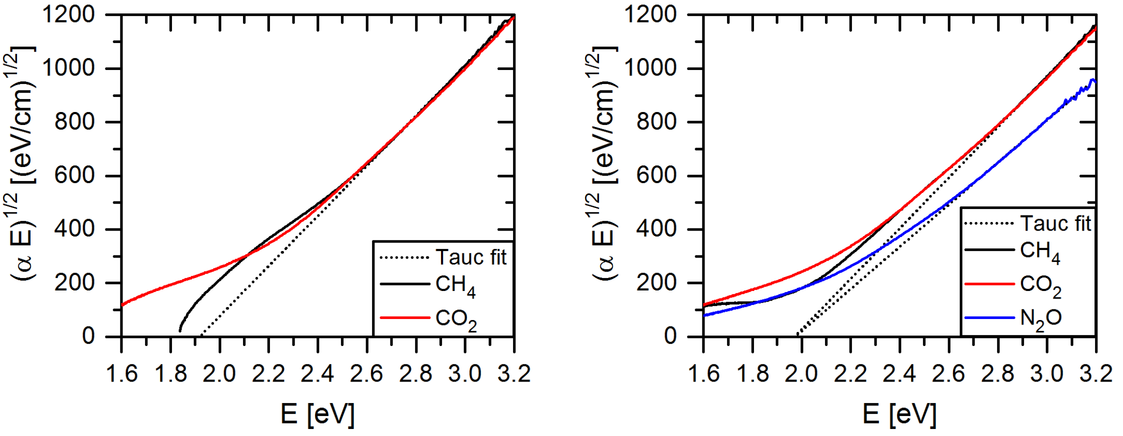

(c) Tauc plot with $E_{Tauc} \approx 1.92\,\mathrm{eV}$. **(d)** Tauc plot with $E_{Tauc} \approx 1.97\,\mathrm{eV}$.

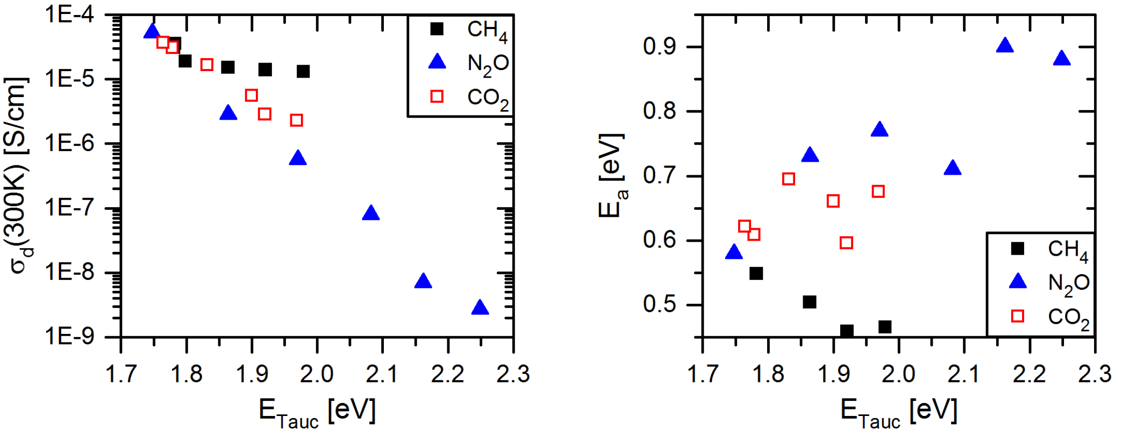

(e) Dark conductivity at room temperature against Tauc bandgap. **(f)** Activation energy against Tauc bandgap.

Figure 5.12: Single layer properties of high bandgap p-doped amorphous silicon alloys produced with N_2O, CO_2 or CH_4.

Figures 5.12c and 5.12d present the Tauc plots (see equation 2.2) of p-doped amorphous silicon alloys prepared with CH_4, CO_2 or N_2O. At similar bandgaps, the only remarkable difference between CH_4 and CO_2 appears in the low energy regime, where films prepared with CO_2 show more defect absorption. Otherwise, the absorption is comparable for CH_4 and CO_2 at equivalent bandgaps. At a bandgap of 1.97 eV the sample prepared with N_2O exhibits less absorption than what is achieved with the other two alloys. Consequently, N_2O might lead to less parasitic absorption of the p-layer than CO_2 and CH_4 at equivalent bandgaps. Yet, the defect absorption of p-layers produced with N_2O superimposes the square root course of the absorption coefficient. So, the Tauc bandgap could be underestimated in the case of N_2O.

The dark conductivity at room temperature in figure 5.12e decreases exponentially with the Tauc bandgap for N_2O and CO_2, while it stays almost constant for CH_4. The dark conductivity associated with CH_4 takes higher values than those related to CO_2 and N_2O at equivalent bandgaps. This finding contradicts the results of Matsumoto et al. [92], who report similar dark conductivities of p-a-SiC:H and p-a-SiO:H with a much higher optical bandgap of p-a-SiO:H. Figure 5.12f shows the activation energy, which takes lower values for samples prepared with CH_4 than when CO_2 or N_2O is used. The activation energy even decreases with the Tauc bandgap in the case of CH_4 while it rises for N_2O and scatters for CO_2. Apparently, CH_4 introduces some kind of p-doping effect. Robertson et al. [94] discovered C_3^- defect centres in silicon rich silicon carbide alloys, which might explain the reduced activation energy of samples prepared with CH_4 in figure 5.12f. The increase of the activation energy associated with N_2O can be explained by the increase of the Tauc bandgap as well as by the n-type doping effect of oxygen and nitrogen [12]. In summary, the dark conductivity and activation energy of p-doped amorphous silicon alloys improve from the use of N_2O to CO_2 to CH_4.

The IV parameters of a-Si:H single cells produced with CO_2, CH_4 or N_2O in the p-layer are depicted in figure 5.13. Standard i-a-Si:H was used as the absorber layer. The results of the cells prepared with N_2O were kindly provided by Alex Neumüller from NEXT ENERGY. These cells were deposited on Asahi VU instead of NSG with a cell thickness of about 400 nm instead of just 250 nm. Thus, all three alloying source gases are only compared with respect to the open circuit voltage and the fill factor. The cells produced with N_2O in the p-layer show the highest open circuit voltage despite their thick absorbers, so this qualitative relation can be trusted in any case. The open circuit voltage rises with the Tauc bandgap for N_2O and CO_2, but stays almost constant for CH_4, neglecting some outliers. In the case of CH_4, the open circuit voltage is lower than for CO_2 and N_2O at all Tauc bandgaps. The trend of the open circuit voltage

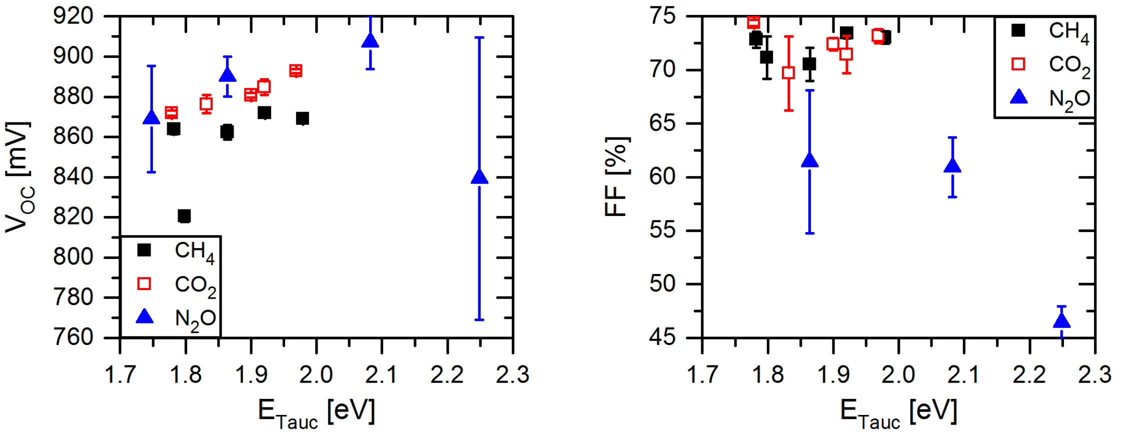

(a) Open circuit voltage. **(b)** Fill factor.

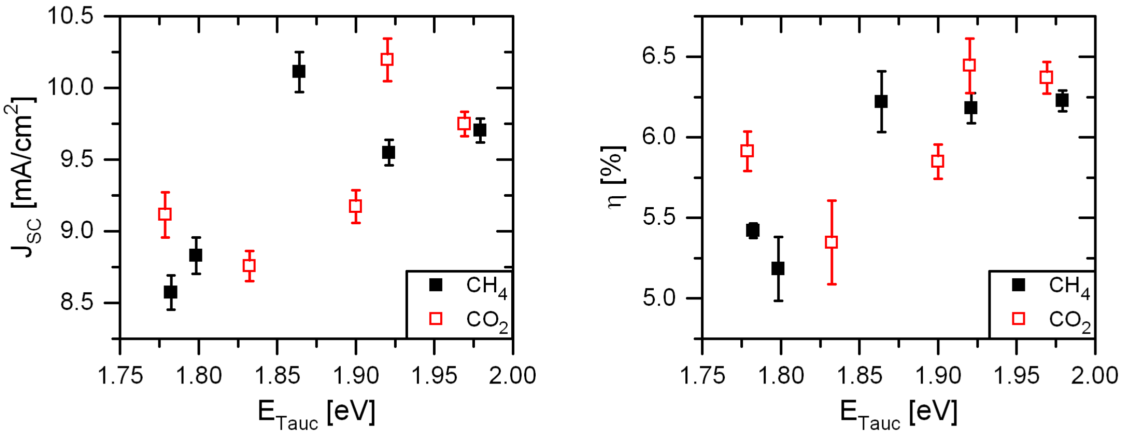

(c) Short circuit current. **(d)** Efficiency.

Figure 5.13: IV parameters of a-Si:H single cells produced with CO_2, CH_4 or N_2O in the p-layer.

can be explained by the trend of the activation energy in figure 5.12f. CH_4 produces a low activation energy, which leads to a low barrier for the holes at the p/i-interface. Consequently, the holes are extracted more easily and the open circuit voltage is reduced compared to the other alloying source gases. The lower activation energy of the p-layers prepared with CH_4 is expected to enhance the fill factor. Yet, as can be seen in figure 5.13b, the fill factors are comparable within the errors for CH_4 and CO_2. The fill factors of the cells prepared with N_2O are quite low. This can be explained by the enhanced activation energy of the respective p-layers and the higher absorber layer thickness. If the activation energy of the p-layer increases the potential barrier at the p/i-interface too much and the absorber layer is too thick, the charge carriers recombine before they can be separated. Moreover, alloying the p-layers with N_2O raises the series resistance

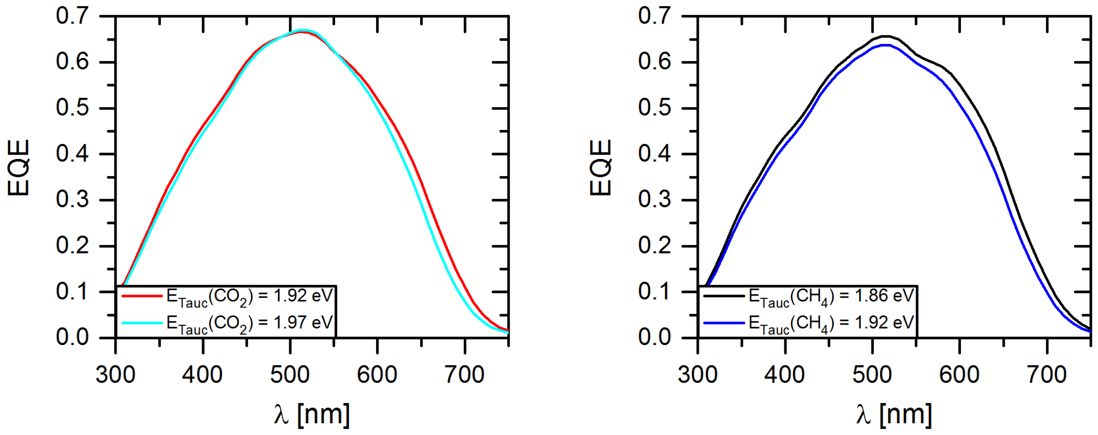

(a) CO_2. **(b)** CH_4.

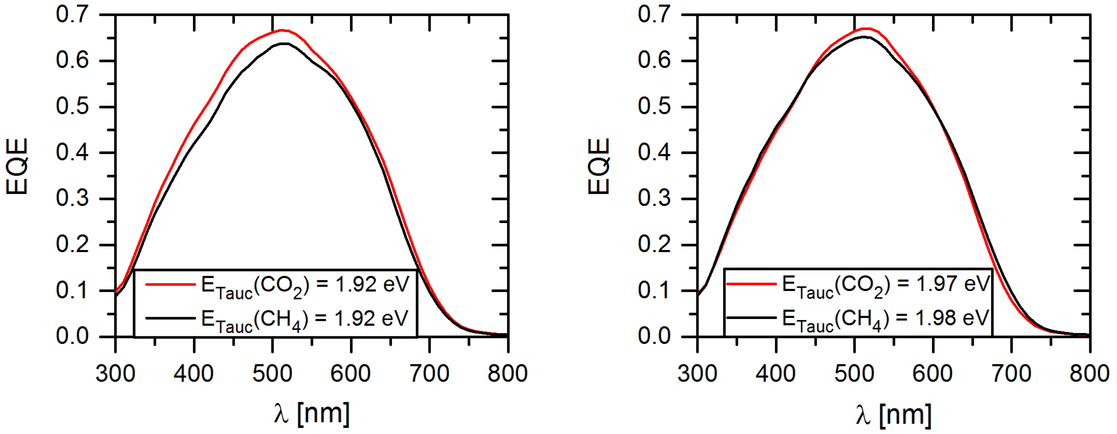

(c) Comparison of CO_2 and CH_4 at a p-layer bandgap of $E_{Tauc} \approx 1.92\,\text{eV}$.

(d) Comparison of CO_2 and CH_4 at a p-layer bandgap of $E_{Tauc} \approx 1.97\,\text{eV}$.

Figure 5.14: EQEs of a-Si:H single cells produced with CO_2 or CH_4 in the p-layer.

of the cells.

The Tauc plots in figures 5.12c and 5.12d predict similar absorption of p-layers produced with CO_2 or CH_4 at equivalent bandgaps. Consequently, the short circuit current in figure 5.13c is comparable for both source gases apart from two outliers.

Figure 5.14 presents the external quantum efficiencies of single cells described in figure 5.13. As demonstrated by figures 5.14a and 5.14b, the EQEs of the outliers at $E_{Tauc}(CO_2) = 1.92\,\text{eV}$ and $E_{Tauc}(CH_4) = 1.86\,\text{eV}$ mainly differ from the EQEs of the cells with the next higher p-layer bandgaps in the red spectral part. This could be an effect of different absorber layer thicknesses or different scattering properties and explain the deviations in the short circuit current. Comparing the EQEs in figure 5.14c, one might conclude that the p-layer prepared with CO_2 is more transparent than the p-layer prepared with CH_4 at equivalent bandgaps. Yet, the EQEs in figure 5.14d are almost the same for CH_4 and CO_2 at a higher comparable p-layer bandgap. Furthermore, figure 5.12c shows the same p-layer absorption for CH_4 and CO_2 also at the lower bandgap of 1.92 eV. So, the difference of the EQEs observed in figure 5.14c and consequently, the difference of the respective short circuit currents in figure 5.13c might be explained by an unintended lower p-layer thickness in the case of CO_2.

As shown in figure 5.13d, the cell efficiency increases by approximately 0.75 % if the p-layer bandgap is raised from 1.78 to 1.98 eV. This enhancement is mainly caused by higher open circuit voltage and higher short circuit current. The open circuit voltage is the only parameter which shows a clear small difference for CH_4 and CO_2. All other relevant parameters are comparable within the errors for both source gases. Since the open circuit voltage is higher for CO_2 than for CH_4, the cell efficiency is also highest in the former case (see figure 5.13d). Judging from the material properties of the p-doped single layers in figure 5.12, CH_4 produces higher dark conductivity and lower activation energy than the remaining source gases at equivalent bandgaps. N_2O performs best with respect to parasitic absorption. Single cells prepared with CO_2 exhibit higher open circuit voltage (see figure 5.13a) and single cell efficiency than cells produced with CH_4 (see figure 5.13d) at equivalent p-layer bandgaps. Nevertheless, CH_4 might still be the better choice if the p-layer bandgap can be raised further, so the activation energy as well as the open circuit voltage are enhanced at even lower parasitic absorption. It remains to be seen if the resulting p-layers produced with CH_4 become as transparent as the p-layers produced with N_2O but with better electrical properties.

5.5 Discussion

The objective of this chapter is to answer the question which kind of amorphous silicon alloy performs best as a high bandgap absorber or a high bandgap p-layer. First of all, high bandgap absorber layers will be discussed.

Other solar cell technologies like III-V, CIGS and perovscites profit from many different atom types forming an ordered crystalline structure. In amorphous silicon, however, other atom types enhance the chemical and structural disorder [42, 79]. So, only hydrogen has a beneficial effect due to defect passivation and network relaxation. Therefore, a high concentration of hydrogen and a low concentration of other impurities is expected to produce better material quality than a lot of impurities and low hydrogen content. Accordingly, Kim et al. [14] report a lower microstructure factor for high hydrogen and

bond lengths [Å]		covalent radii [Å]	
Si−Si	2.35	Si	1.17
C−Si	1.87	C	0.77
N−Si	1.57	N	0.70
O−Si	1.53	O	0.66

Table 5.2: Bond lengths with silicon and covalent radii of silicon, carbon, oxygen and nitrogen [24, 79].

low oxygen content in the amorphous silicon alloys than for the opposite composition at similar bandgaps. Consequently, the best strategy for the production of high bandgap amorphous silicon alloys is to maximise the hydrogen content still leading to good material quality. Then, a small amount of a different kind of impurity can be added to raise the bandgap further. This leads to very small impurity concentrations (see figure 5.1a), which makes the distinction of material properties and, therefore, the comparison of the respective source gases difficult.

In this work, the most remarkable differences are observable in the microstructure factor (see figure 5.6c) and the open circuit voltage (see figures 5.9a and 5.11a) giving CH_4 precedence over CO_2. In contrast to carbon, oxygen and nitrogen have an n-type doping effect by O_3^+ and N_4^+ impurities [12, 86]. Nitrogen produces a higher negatively charged defect density than oxygen at the same impurity content [12]. This might explain why CO_2 yields better single layer and single cell properties than N_2O in figures 5.3 and 5.4. The doping effect of oxygen becomes obvious in figures 5.8b and 5.7a, which show that the use of CO_2 leads to higher photo- and dark conductivity values than alloying with CH_4.

Just like silicon carbon can form a tetrahedral structure with a fourfold coordination [79]. The coordination of nitrogen is threefold in an almost planar way in the alloy [95]. Oxygen is twofold coordinated. It forms an angle of 144° in the Si-O-Si bridge, whereas the tetrahedron angle between two Si-Si bonds is just 109.5° [65]. The covalent radius and the bond length with silicon are larger for carbon than for oxygen or nitrogen and thereby closer to the values of pure silicon (see table 5.2) [24, 79]. Consequently, carbon matches the silicon network better than the other two species. This is demonstrated by the microstructure factor in figure 5.6c, which suggests a denser network of the films prepared with CH_4 instead of CO_2. Carbon introduces less surface defects than oxygen at equivalent concentrations [12]. Moreover, the bonding properties of carbon might allow a more random continuous distribution in the film, while oxygen is often reported to form clusters in a two phase material [65, 96]. This is confirmed by the (Si-O-Si)-O_n stretching modes in figure 5.6a.

With regard to the amorphous high bandgap p-doped layers it is difficult to determine the best alloying source gas. Films prepared with CH_4 exhibit better electrical properties than films prepared with CO_2 and both source gases outperform N_2O (see figures 5.12e and 5.12f). The n-type doping effect of nitrogen and oxygen, explained above, could account for these observations. However, provided that the Tauc bandgap is not underestimated, p-layers prepared with N_2O are more transparent than p-layers produced with CO_2 or CH_4 at equivalent bandgaps (see figure 5.12d).

The open circuit voltage of single cells is higher when using CO_2 in the p-layer instead of CH_4 (see figure 5.13a). The highest open circuit voltage is achieved with N_2O in the p-layer. This can be explained by the activation energy, which mirrors the trend of the open circuit voltage (see figures 5.13a and 5.12f). A higher activation energy increases the potential barrier at the p/i-interface. Consequently, the hole density at the interface is enhanced and the respective quasi Fermi level is lowered leading to a higher open circuit voltage. This strategy only works out if the prolonged residence time of charge carriers in the space charge region does not cause their recombination at defects and the series resistance is not increased. Otherwise, the fill factor drops, as demonstrated by the data associated with N_2O in figure 5.13b. The activation energy of p-doped layers prepared with CH_4 might be enhanced by raising the bandgap further. This would have the benefit of higher open circuit voltage as well as less parasitic absorption. It remains to be seen if the transparency obtained with N_2O can be achieved with CH_4 but at better electrical quality. Consequently, CH_4 could also be the best choice for the development of a p-doped high bandgap amorphous silicon alloy.

All in all, CH_4 performs best, when used for the high bandgap amorphous silicon absorber layer and CO_2 gives the better cell results when used in the p-doped layer. However, CH_4 has the potential to outperform CO_2 in the p-doped layer as well, if the bandgap can be raised further.

5.6 Conclusion

The single layer and single cell performance improves from the use of N_2O, to CO_2 to CH_4 in the production of the intrinsic layer. This can be explained by the n-type doping effect of oxygen and nitrogen. The negatively charged defect density introduced by nitrogen is higher than in the case of oxygen at equivalent concentrations. Moreover, the atomic coordination geometry in form of coordination number, covalent radii, bonding angle and bond length with silicon is closer for carbon and silicon than for oxygen or nitrogen and silicon. Therefore, carbon matches the silicon network better than oxygen or nitrogen, which becomes obvious in the reduced microstructure factor of i-a-SiC:H layers. The superior single layer properties of amorphous silicon carbide lead to a maximum open circuit voltage of 1000 mV at a Tauc bandgap of 1.99 eV and a fill factor of 65 %.

P-layers produced with CH_4 show higher conductivity and lower activation energy than p-layers produced with N_2O or CO_2 at equivalent bandgaps. The reason for this observation could be the n-type doping effect of oxygen and nitrogen as well. Consequently, the bandgap of p-layers prepared with CH_4 can probably be raised to higher values without significant deterioration of the electrical properties.

Taking the previous findings and the simulation results into account, the optimal top cell in a quadruple configuration should be prepared with CH_4 in the p- and the i-layer aiming for bandgaps of 2.33 and 2.08 eV.

6

Conclusion and Outlook

The objective of this work was to clarify the development steps for an optimised top cell by answering the following questions formulated in the introduction:

1. What is the benefit of a high bandgap amorphous silicon absorber alloy compared to a-Si:H? Which maximum top cell absorber layer bandgap still leads to sufficient current in a triple or quadruple cell configuration?
2. How do the parameters of the RF-PECVD process have to be modified to optimise the material quality of high bandgap amorphous silicon alloys?
3. When methane (CH_4) is used for the introduction of carbon and carbon dioxide (CO_2) or nitrous oxide (N_2O) for the introduction of oxygen at the same RF-PECVD setup under similar conditions, which type of source gas is suited best for which functional layer and why?

Using simulation tools, deposition techniques and various measurement equipment the following answers could be gained:

6.1 Optimal Top Cell Bandgap and Potential Estimation

A single top cell was simulated with Sentaurus TCAD employing state of the art optical data and optimal scattering conditions. The upper limit of the absorber layer thickness was determined to be 300 nm. Moreover, the optimal p-layer bandgap was found to exceed the adjacent i-layer bandgap by about 0.25 eV. As a result, the maximum i-layer bandgap of the top cell, which still leads to sufficient current, is 1.91 eV in a triple cell and 2.08 eV in a quadruple cell. The corresponding cell efficiencies are estimated to 19.54 %

for the triple cell and to 19.78 % for the quadruple cell. Since the optimal top cell bandgap for the triple configuration can be achieved with a-Si:H, no further alloying with oxygen or carbon is required. Yet, in a quadruple cell configuration, high bandgap amorphous silicon absorber alloys lead to an efficiency gain of 0.6 %, if the top cell bandgap is raised from 1.90 to 2.05 eV.

6.2 Process Development

For the development of high bandgap absorber layers the standard recipe of amorphous silicon was changed by introducing small flow ratios of CO_2 or CH_4, lowering the heater temperature from 220 to 180 °C and by raising the dilution of silane in hydrogen from 5 to 30. The best material quality was achieved with process parameters leading to low oxygen or carbon content, high hydrogen content and a low growth rate. Consequently, the best strategy for the development of an amorphous silicon based high bandgap absorber is to favour hydrogen incorporation over carbon or oxygen incorporation. In order to raise the hydrogen content, the substrate temperature during the RF-PECVD process has to be lowered. Unfortunately, this also reduces the surface reaction rate of the different species in the plasma and thereby enhances the porosity of the growing film. Since the surface reaction rate competes with the growth rate, lowering the growth rate by choosing low pressure, low power and high hydrogen dilution restores the required film density.

6.3 Comparison of N_2O, CO_2 and CH_4

When developing an optimised top cell, the question arises which alloying source gas, apart from hydrogen, leads to the best layer quality of high bandgap amorphous silicon alloys. To answer this question, single layers and single cells were produced at the same deposition setup under similar conditions using N_2O, CO_2 and CH_4 as alloying source gases.

Single cells produced with CO_2 in the i-layer show higher open circuit voltage and fill factor at equivalent Tauc bandgaps than cells produced with N_2O. The reason for this observation could be an enhanced negatively charged defect density introduced by nitrogen.

The single layer and single cell properties of samples prepared with CH_4 in the intrinsic layer are superior to the properties of samples prepared with CO_2. Thus, the highest open circuit voltage of 1000 mV is achieved with CH_4 at an absorber layer bandgap of ca. 1.99 eV and a fill factor of 65 %. In the case CO_2 the open circuit voltage is lower by 80 mV at an equivalent bandgap. The inferior performance of CO_2 can be explained the n-type doping effect of O_3^+ sites. Moreover, the atomic coordination geometry in form of coordination number, bond lengths and covalent radii is more similar for silicon and carbon than for silicon and oxygen. Consequently, the addition of carbon leads to a denser network than the addition of oxygen.

When CO_2 is used in the production of the p-layer, the single cell performance is slightly better than for CH_4 because of higher open circuit voltage. This can be explained by the higher activation energy of the p-layers produced with CO_2. A higher activation energy can be beneficial for the p-layer, as long as the open circuit voltage is enhanced and the fill factor does not deteriorate. The activation energy of the p-layers produced with CH_4 can probably be raised by increasing the bandgap. This may be achieved with higher CH_4 dilution and has the benefit of decreasing the parasitic absorption of the p-layer further. Thus, CH_4 does not only lead to better material quality than CO_2 in the intrinsic layer, but probably also in the p-doped layer.

6.4 Outlook

The best amorphous silicon alloy single cell prepared with CH_4 in the i-layer shows an initial efficiency of 4.95 % (see figure 5.9). This is achieved at 1.88 eV Tauc bandgap of the i-layer and with about 200 nm absorber thickness. The remaining IV parameters are: V_{OC} = 986 mV, FF = 68 % and J_{SC} = 7.38 mA/cm^2. The highest open circuit voltage of 1000 mV is obtained with CH_4 at an absorber layer bandgap of ca. 1.99 eV and a fill factor of 65 %.

Improvements of the present single cells can be achieved by raising the bandgap of the p-layer beyond the bandgap of the adjacent i-layer. According to the simulation, the p-layer bandgap should exceed the i-layer bandgap by 0.25 eV. CH_4 is likely to increase the p-layer bandgap considerably without too much loss of activation energy and conductivity. So, CH_4 is recommended for the p-layer development, although it remains to be seen if CH_4 can also outperform N_2O in terms of p-layer transparency.

The electrical quality of the interfaces may be tuned with the help of high bandgap buffer layers. There is also further potential for optimising the process conditions of the intrinsic layer using CH_4 and aiming for a bandgap of 2.08 eV. Based on optimised materials for all relevant layers, the next step would be the integration of the high bandgap top cell absorber in the development of a quadruple cell.

Bibliography

[1] J. Tauc, R. Grigorovici and A. Vancu. *Optical Properties and Electronic Structure of Amorphous Germanium*, physica status solidi (b) **15**, 627–637 (1966).

[2] A. Shah, C. Ballif, W. Beyer, F. Finger, H. Schade and N. Wyrsch. Thin-film silicon solar cells. EPFL Press, Lausanne, 1 edition (2010).

[3] H. Sai, T. Matsui, T. Koida, K. Matsubara, M. Kondo, S. Sugiyama, Y. Takeuchi and I. Yoshida. *Triple-junction thin-film silicon solar cell fabricated on periodically textured substrate with a stabilized efficiency of 13.6%*, Applied Physics Letters **106**, 213902 (2015).

[4] M. A. Green, K. Emery, Y. Hishikawa, W. Warta and E. D. Dunlop. *Solar cell efficiency tables (Version 45)*, Progress in Photovoltaics: Research and Applications **23**, 1–9 (2015).

[5] NREL. *Reference Solar Spectral Irradiance: Air Mass 1.5*, http://rredc.nrel.gov/solar/spectra/am1.5/.

[6] C. Feser, J. Lacombe, K. v. Maydell and C. Agert. *A simulation study towards a new concept for realization of thin film triple junction solar cells based on group IV elements*, Progress in Photovoltaics: Research and Applications **20**, 74–81 (2012).

[7] F. Meillaud, a. Shah, C. Droz, E. Vallat-Sauvain and C. Miazza. *Efficiency limits for single-junction and tandem solar cells*, Solar Energy Materials and Solar Cells **90**, 2952–2959 (2006).

[8] I. A. Yunaz, A. Yamada and M. Konagai. *Theoretical Analysis of Amorphous Silicon Alloy Based Triple Junction Solar Cells*, Jpn. J. Appl. Phys. **46**, L1152 (2007).

[9] S. Fujikake, H. Ohta, A. Asano, Y. Ichikawa and H. Sakai. *High Quality a-SiO:H Films and their Application to a-Si Solar Cells*, Mat. Res. Soc. Symp. Proc. **258**, 875–880 (1992).

[10] A. Desalvo, F. Giorgis, C. F. Pirri, E. Tresso, P. Rava, R. Galloni, R. Rizzoli and C. Summonte. *Optoelectronic properties, structure and composition of a-SiC:H films grown in undiluted and H_2 diluted silane-methane plasma*, J. Appl. Phys. **81**, 7973–7980 (1997).

[11] D. Das, S. M. Iftiquar and A. K. Barua. *Wide optical-gap a-SiO:H films prepared by rf glow discharge*, Journal of Non-Crystalline Solids **210**, 148–154 (1997).

[12] T. Shimizu, T. Ishii, M. Kumeda and A. Masuda. *Structural and conductivity change caused by N , O and C incorporation in a-Si:H*, Journal of Non-Crystalline Solids **227-230**, 403–406 (1998).

[13] S. Inthisang, B. Janthong, P. Sichanugrist and M. Konagai. *Fabrication of Novel Structure a-$Si_{1-x}O_x$:H/a-Si:H/μc-Si:H Triple-Junction Solar Cells.* In: 26th European Photovoltaic Solar Energy Conference and Exhibition, 2011.

[14] D. Y. Kim, E. Guijt, R. A. C. M. M. van Swaaij and M. Zeman. *Development of a-SiO_x:H solar cells with very high V_{OC} x FF product*, Progress in Photovoltaics: Research and Applications **23**, 671–684 (2014).

[15] J. Ma, J. Ni, J. Zhang, Q. Liu, X. Chen, D. Zhang, X. Zhang and Y. Zhao. *High open-circuit voltage (1.04V) n-i-p type thin film silicon solar cell by two-phase silicon carbide intrinsic material*, Solar Energy Materials and Solar Cells **130**, 561–566 (2014).

[16] P. Sichanugrist, N. Pingatea and C. Piromjita. *High-Performance, Tandem-Type Amorphous Silicon Solar Cell.* In: MRS Proceedings, 2007.

[17] I. A. Yunaz, H. Nagashima, D. Hamashita, S. Miyajima and M. Konagai. *Wide-gap a-$Si_{1-x}C_x$:H solar cells with high light-induced stability for multijunction structure applications*, Solar Energy Materials and Solar Cells **95**, 107–110 (2011).

[18] K. Sriprapha, A. Hongsingthong, T. Krajangsang, S. Inthisang, S. Jaroensathainchok, A. Limmanee, W. Titiroongruang and J. Sritharathikhun. *Development of thin film a-SiO:H/a-Si:H double-junction solar cells and their temperature dependence*, Thin Solid Films **546**, 398–403 (2013).

[19] F. T. Si, D. Y. Kim, R. Santbergen, H. Tan, R. A. C. M. M. van Swaaij, A. H. M. Smets, O. Isabella and M. Zeman. *Quadruple-junction thin-film silicon-based solar cells with high open-circuit voltage*, Applied Physics Letters **105**, 063902 (2014).

[20] D. Y. Kim, E. Guijt, F. T. Si, R. Santbergen, J. Holovský, O. Isabella, R. a.C.M.M. van Swaaij and M. Zeman. *Fabrication of double- and triple-junction solar cells with hydrogenated amorphous silicon oxide (a-SiO$_x$:H) top cell*, Solar Energy Materials and Solar Cells **141**, 148–153 (2015).

[21] S. Inthisang, T. Krajangsang, P. Sichanugrist, T. Watahiki, S. Miyajima, A. Yamada and M. Konagai. *Effect of Hydrogen Dilution on the Metastability of Hydrogenated Amorphous Silicon Oxide Solar Cells*, Japanese Journal of Applied Physics **50**, 111401 (2011).

[22] G. Bruno, P. Capezzuto and A. Madan. Plasma Deposition of Amorphous Silicon-Based Materials. Plasma-Materials Interactions. Academic Press Inc., San Diego (1995).

[23] A. F. Holleman and E. Wiberg. Lehrbuch der anorganischen Chemie. de Gruyter, Berlin, 102 edition (2007).

[24] J. A. Dean, editor. Lange's Handbook of Chemistry. McGRAW-HILL, INC., New York, 15th edition (1999).

[25] D. Das and A. K. Barua. *Properties of a-SiO:H films prepared by RF glow discharge*, Solar Energy Materials and Solar Cells **60**, 167–179 (2000).

[26] S. M. Iftiquar. *The roles of deposition pressure and rf power in opto-electronic properties of a-SiO:H films*, Journal of Physics D: Applied Physics **31**, 1630 (1998).

[27] Y. Hishikawa, S. Tsuge, N. Nakamura, S. Tsuda, S. Nakano and Y. Kuwano. *Device-quality wide-gap hydrogenated amorphous silicon films deposited by plasma chemical vapor deposition at low substrate temperatures.*, Journal of Applied Physics **69**, 508–510 (1991).

[28] M. Fukawa, S. Suzuki, L. Guo, M. Kondo and A. Matsuda. *High rate growth of microcrystalline silicon using a high-pressure depletion method with VHF plasma*, Solar Energy Materials and Solar Cells **66**, 217–223 (2001).

[29] B. P. Wickboldt, S. J. Jones, F. C. Marques, D. Pang, W. A. Turner, A. E. Wetsel, W. Paul and J. H. Chen. *A study of the properties of hydrogenated amorphous germanium produced by r.f. glow discharge as the electrode gap is varied: the link between microstructure and optoelectronic properties*, Philosophical Magazine Part B **64**, 655–674 (1991).

[30] M. H. Brodsky, M. a. Frisch, J. F. Ziegler and W. a. Lanford. *Quantitative analysis of hydrogen in glow discharge amorphous silicon*, Applied Physics Letters **30**, 561–563 (1977).

[31] G. Ambrosone, D. Basa, U. Coscia and P. Rava. *Correlation between structural and opto-electronic properties of a-*$Si_{1-x}C_x$*:H films deposited by plasma enhanced chemical vapour deposition*, Thin Solid Films **518**, 5871–5874 (2010).

[32] H. Fujiwara. Spectroscopic Ellipsometry: Principles and Applications. John Wiley & Sons, Chichester (2007).

[33] S. K. O'Leary, S. R. Johnson and P. K. Lim. *The relationship between the distribution of electronic states and the optical absorption spectrum of an amorphous semiconductor: An empirical analysis*, Journal of Applied Physics **82**, 3334 (1997).

[34] W. Theiss. *SCOUT technical manual.* Rapport technique 49, W.Theiss Hard- and Software, Aachen, 2012.

[35] M. Vanecek, J. Kocka, J. Stuchlik and A. Triska. *Direct measurement of the gap states and band tail absorption by constant photocurrent method in amorphous silicon*, Solid State Communications **39**, 1199–1202 (1981).

[36] N. Wyrsch, F. Finger, T. McMahon and M. Vanecek. *How to reach more precise interpretation of subgap absorption spectra in terms of deep defect density in a-Si:H*, Journal of Non-Crystalline Solids **137-138**, 347–350 (1991).

[37] K. Pierz, W. Fuhs and H. Mell. *On the mechanism of doping and defect formation in a-Si:H*, Philosophical Magazine B **63**, 123–141 (1991).

[38] M. Cardona. *Vibrational Spectra of Hydrogen in Silicon and Germanium*, phys. stat. sol. (b) **118**, 463–481 (1983).

[39] A. Langford, M. Fleet, B. Nelson, W. Lanford and N. Maley. *Infrared absorption strength and hydrogen content of hydrogenated amorphous silicon.*, Physical review. B, Condensed matter **45**, 13367–13377 (1992).

[40] G. Lucovsky, J. Yang, S. Chao, J. Tyler and W. Czubatyj. *Oxygen-bonding environments in glow-discharge-deposited amorphous silicon-hydrogen alloy films*, Physical Review B **28**, 3225–3233 (1983).

[41] A. H. Mahan, P. Menna and R. Tsu. *Influence of microstructure on the Urbach edge of amorphous SiC:H and amorphous SiGe:H alloys*, Applied Physics Letters **51**, 1167 (1987).

[42] A. H. Mahan, P. Raboisson and R. Tsu. *Influence of microstructure on the photoconductivity of glow discharge deposited amorphous SiC:H and amorphous SiGe:H alloys*, Applied Physics Letters **50**, 335 (1987).

[43] A. H. M. Smets, W. M. M. Kessels and M. C. M. van de Sanden. *Vacancies and voids in hydrogenated amorphous silicon*, Applied Physics Letters **82**, 1547 (2003).

[44] A. H. M. Smets and M. C. M. van de Sanden. *Relation of the Si-H stretching frequency to the nanostructural Si-H bulk environment*, Physical Review B **76**, 073202 (2007).

[45] H. Overhof and W. Beyer. *A model for the electronic transport in hydrogenated amorphous silicon*, Philosophical Magazine B **43**, 433–450 (1981).

[46] W. K. Chu, J. W. Mayer and M. A. Nicolet. Backscattering Spectrometry. Academic Press Inc., New York (1978).

[47] Synopsys. *Sentaurus Device User Guide J-2014.09*. Rapport technique September, Synopsys, Inc., 2014.

[48] J. Krc, F. Smole and M. Topic. *Analysis of light scattering in amorphous Si:H solar cells by a one-dimensional semi-coherent optical model*, Progress in Photovoltaics: Research and Applications **11**, 15–26 (2003).

[49] H. Bennett and J. Porteus. *Relation between surface roughness and specular reflectance at normal incidence*, Journal of the Optical Society of America **51**, 123–129 (1961).

[50] S. Kim, J. W. Chung, H. Lee, J. Park, Y. Heo and H. M. Lee. *Remarkable progress in thin-film silicon solar cells using high-efficiency triple-junction technology*, Solar Energy Materials and Solar Cells **119**, 26–35 (2013).

[51] B. Yan, G. Yue, L. Sivec, J. Yang, S. Guha and C. S. Jiang. *Innovative dual function nc-SiO$_x$:H layer leading to a $>$ 16% efficient multi-junction thin-film silicon solar cell*, Appl. Phys. Lett. **99**, 113512–113513 (2011).

[52] T. Matsui, H. Jia and M. Kondo. *Thin film solar cells incorporating microcrystalline $Si_{1-x}Ge_x$ as efficient infrared absorber: an application to double junction tandem solar cells*, Progress in Photovoltaics: Research and Applications **18**, 48–53 (2010).

[53] T. Matsui, M. Kondo, K. Ogata, T. Ozawa and M. Isomura. *Influence of alloy composition on carrier transport and solar cell properties of hydrogenated microcrystalline silicon-germanium thin films*, Appl. Phys. Lett. **89**, 142113–142115 (2006).

[54] M. Stuckelberger, M. Despeisse, G. Bugnon, J. W. Schüttauf, F. J. Haug and C. Ballif. *Comparison of amorphous silicon absorber materials: Light-induced degradation and solar cell efficiency*, Journal of Applied Physics **114**, 154509 (2013).

[55] O. Isabella, A. H. M. Smets and M. Zeman. *Thin-film silicon-based quadruple junction solar cells approaching 20% conversion efficiency*, Solar Energy Materials and Solar Cells **129**, 82–89 (2014).

[56] S. Hänni, G. Bugnon, G. Parascandolo, M. Boccard, J. Escarré, M. Despeisse, F. Meillaud and C. Ballif. *High-efficiency microcrystalline silicon single-junction solar cells*, Progress in Photovoltaics: Research and Applications **21**, 821–826 (2013).

[57] C. Walder, M. Kellermann, E. Wendler, J. Rensberg, K. von Maydell and C. Agert. *Comparison of silicon oxide and silicon carbide absorber materials in silicon thin-film solar cells*, EPJ Photovoltaics **6**, 65302 (2015).

[58] F. Orapunt and S. K. O'Leary. *Optical transitions and the mobility edge in amorphous semiconductors: A joint density of states analysis*, Journal of Applied Physics **104**, 073513 (2008).

[59] M. Stutzmann. *The defect density in amorphous silicon*, Philosophical Magazine B **60**, 531–546 (1989).

[60] Y. Tawada, K. Tsuge, M. Kondo, H. Okamoto and Y. Hamakawa. *Properties and structure of a-SiC:H for high-efficiency a-Si solar cell*, Journal of Applied Physics **53**, 5274–5281 (1982).

[61] D. L. Staebler and C. R. Wronski. *Reversible conductivity changes in discharge-produced amorphous Si*, Applied Physics Letters **31**, 292–294 (1977).

[62] M. Stuckelberger, A. Billet, Y. Riesen, M. Boccard, M. Despeisse, J. W. Schüttauf, F. J. Haug and C. Ballif. *Comparison of amorphous silicon absorber materials: Kin-*

etics of light-induced degradation. In: Progress in Photovoltaics: Research and Applications, volume 29th EU PVSEC, Amsterdam, 2014.

[63] H. Kakinuma, S. Nishikawa and T. Watanabe. *Thickness Dependence of Staebler-Wronski Effect in a-Si:H*, Journal of Non-Crystalline Solids **59-60**, 421–424 (1983).

[64] R. E. Schropp and M. Zeman. Amorphous and Microcrystalline Silicon Solar Cells: Modeling, Materials and Device Technology. Kluwer Academic Publishers, Massachusetts (1998).

[65] N. Tomozeiu. *Silicon Oxide (SiO$_x$, 0 < x < 2): a Challenging Material for Optoelectronics*. In: P. Predeep, editor, Optoelectronics - Materials and Techniques, chapitre Chapter 3, 55–98. InTech (2011).

[66] D. Das, S. M. Iftiquar, D. Das and A. K. Barua. *Improvement in the optoelectronic properties of a-SiO:H films*, Journal of Materials Science **34**, 1051–1054 (1999).

[67] D. K. Basa. *Correlation between the opto-electronic and structural parameters of amorphous semiconductors*, Thin Solid Films **406**, 75–78 (2002).

[68] R. A. Street. Hydrogenated Amorphous Silicon. Cambridge University Press, Cambridge (1991).

[69] N. Maley and J. Lannin. *Influence of hydrogen on vibrational and optical properties of a-Si$_{1-x}$H$_x$ alloys*, Phys. Rev. B **36**, 1146–1152 (1987).

[70] R. Biron, C. Pahud, F. J. Haug, J. Escarré, K. Soderstrom and C. Ballif. *Window layer with p doped silicon oxide for high V_{OC} thin-film silicon n-i-p solar cells*, J. Appl. Phys. **110**, 124511–124517 (2011).

[71] P. Cuony, D. T. L. Alexander, I. Perez-Wurfl, M. Despeisse, G. Bugnon, M. Boccard, T. Söderström, A. Hessler-Wyser, C. Hébert and C. Ballif. *Silicon Filaments in Silicon Oxide for Next-Generation Photovoltaics*, Advanced Materials **24**, 1182–1186 (2012).

[72] A. Janotta, R. Janssen, M. Schmidt, T. Graf, M. Stutzmann, L. Görgens, A. Bergmaier, G. Dollinger, C. Hammerl, S. Schreiber and B. Stritzker. *Doping and its efficiency in a-SiO$_x$:H*, Phys. Rev. B **69**, 115206 (2004).

[73] S. Inthisang, T. Krajangsang, I. A. Yunaz, A. Yamada, M. Konagai and C. R. Wronski. *Fabrication of high open-circuit voltage a-Si$_{1-x}$O$_x$:H solar cells by using p-a-Si$_{1-x}$O$_x$:H as window layer*, Physica Status Solidi (C) **8**, 2990–2993 (2011).

[74] K. Yoon, Y. Kim, J. Park, C. H. Shin, S. Baek, J. Jang, S. M. Iftiquar and J. Yi. *Preparation and characterization of p-type hydrogenated amorphous silicon oxide film and its application to solar cell*, Journal of Non-Crystalline Solids **357**, 2826–2832 (2011).

[75] I. A. Yunaz, K. Hashizume, S. Miyajima, A. Yamada and M. Konagai. *Fabrication of amorphous silicon carbide films using VHF-PECVD for triple-junction thin-film solar cell applications*, Solar Energy Materials and Solar Cells **93**, 1056–1061 (2009).

[76] K. Haga, K. Yamamoto, M. Kumano and H. Watanabe. *Wide Optical-Gap a-Si:O:H Films Prepared from* SiH_4-CO_2 *Gas Mixture*, Japanese Journal of Applied Physics **25**, L39–L41 (1986).

[77] S. Knief and W. von Niessen. *Disorder, defects, and optical absorption in a-Si and a-Si:H*, Phys. Rev. B **59**, 12940–12946 (1999).

[78] A. Singh and E. Davis. *The* SiO_x:H_y *thin film system. II. Optical bandgap behavior*, Journal of Non-Crystalline Solids **122**, 233–240 (1990).

[79] J. Bullot and M. Schmidt. *Physics of Amorphous Silicon-Carbon Alloys*, phys. stat. sol. (b) **143**, 345 (1987).

[80] T. Jana, S. Ghosh and S. Ray. *Silicon oxide thin films prepared by a photo-chemical vapour deposition technique*, Journal of Materials Science **32**, 4895–4900 (1997).

[81] D. Kuhman, S. Grammatica and F. Jansen. *Properties of hydrogenated amorphous silicon carbide films prepared by plasma-enhanced chemical vapor deposition*, Thin Solid Films **177**, 253–262 (1989).

[82] A. Samanta and D. Das. *Studies on the structural properties of SiO:H films prepared from* (SiH_4+CO_2+He) *plasma in RF-PECVD*, Solar Energy Materials and Solar Cells **93**, 588–596 (2009).

[83] N. Beck, N. Wyrsch, C. Hof and A. Shah. *Mobility lifetime product - A tool for correlating a-Si:H film properties and solar cell performances*, Journal of Applied Physics **79**, 9361–9368 (1996).

[84] S. Wang, V. Smirnov, T. Chen, B. Holländer, X. Zhang, S. Xiong, Y. Zhao and F. Finger. *Effects of oxygen incorporation in solar cells with a-*SiO_x*:H absorber layer*, Japanese Journal of Applied Physics **54**, 011401 (2015).

[85] S. Inthisang, K. Sripapha, A. Yamada and M. Konagai. *Characterization of wide bandgap a-SiO:H films and their application to thin film solar cells.* In: Photovoltaic Specialists Conference 2008 (PVSEC 2008), 33rd IEEE, 1–4, 2008.

[86] A. Morimoto, M. Matsumoto, M. Yoshita, M. Kumeda and T. Shimizu. *Doping effect of oxygen or nitrogen impurity in hydrogenated amorphous silicon films*, Applied Physics Letters **59**, 2130 (1991).

[87] M. Losurdo, M. Giangregorio, P. Capezzuto, G. Bruno and F. Giorgis. *Structural and optical investigation of plasma deposited silicon carbon alloys: Insights on Si-C bond configuration using spectroscopic ellipsometry*, J. Appl. Phys. **97**, 103504–103506 (2005).

[88] F. Demichelis, C. F. Pirri and E. Tresso. *Influence of doping on the structural and optoelectronic properties of amorphous and microcrystalline silicon carbide*, Journal of Applied Physics **72**, 1327 (1992).

[89] H. K. Tsai, W. L. Lin, W. J. Sah and S. C. Lee. *The characteristics of amorphous silicon carbide hydrogen alloy*, Journal of Applied Physics **64**, 1910 (1988).

[90] R. Janssen, A. Janotta, D. Dimova-Malinovska and M. Stutzmann. *Optical and electrical properties of doped amorphous silicon suboxides*, Phys. Rev. B **60**, 13561–13572 (1999).

[91] P. Cuony, M. Marending, D. T. L. Alexander, M. Boccard, G. Bugnon, M. Despeisse and C. Ballif. *Mixed-phase p-type silicon oxide containing silicon nanocrystals and its role in thin-film silicon solar cells*, Applied Physics Letters **97**, 213502 (2010).

[92] Y. Matsumoto, F. Meléndez and R. Asomoza. *Performance of p-type silicon-oxide windows in amorphous silicon solar cell*, Solar Energy Materials and Solar Cells **66**, 163–170 (2001).

[93] C. Walder, A. Neumüller, O. Sergeev, M. Kellermann, K. Von Maydell and C. Agert. *Amorphous silicon oxinitride in silicon thin-film solar cells*, Energy Procedia **44**, 203–208 (2014).

[94] J. Robertson. *The electronic and atomic structure of hydrogenated amorphous Si-C alloys*, Philosophical Magazine Part B **66**, 615–638 (1992).

[95] J. Robertson. *Electronic structure of silicon nitride*, Philosophical Magazine Part B **63**, 47–77 (1991).

[96] S. M. Iftiquar. *Structural Studies on Semiconducting Hydrogenated Amorphous Silicon Oxide Films*, High temperature Material Processes **6**, 35 (2002).

Erklärung

Hiermit erkläre ich, dass ich diese Arbeit selbständig verfasst sowie nur die angegebenen Quellen und Hilfsmittel verwendet habe.

Oldenburg, den 25.09.2015

Danksagung

Viele Menschen in meinem Umfeld haben durch ihre Unterstützung zum Gelingen dieser Arbeit beigetragen. Daher danke ich insbesondere:

- Prof. Dr. Carsten Agert für die Betreuung und Begutachtung der Arbeit sowie für die Möglichkeit zur Durchführung dieser Promotion bei NEXT ENERGY.
- Prof. Dr. Jürgen Parisi für die Übernahme des Zweitgutachtens.
- Prof. Dr. Manuela Schiek für die Übernahme der dritten Prüfungsrolle bei der Disputation.
- Dr. Karsten von Maydell für die intensive Betreuung der Arbeit und die hilfreichen Ermutigungen.
- Dr. Martin Vehse für das Interesse an der Arbeit und die Unterstützung bei NEXT ENERGY.

Weiterhin gilt mein herzlicher Dank:

- Prof. Dr. Elke Wendler, Jura Rensberg und Ulrich Barth von der Friedrich-Schiller-Universität Jena für die Ermöglichung und Betreuung von EBS Messungen.
- Dr. Sven Holinski vom Fraunhofer ISE in Gelsenkirchen für CPM- und Leitfähigkeitsmessungen.
- Martin Kellermann von NEXT ENERGY für die Unterstützung bei der Substratpräparation sowie bei PECVD- und Elektronenstrahlabscheidungen.
- Ortwin Siepmann, Martin Kellermann, Antje Schweitzer und Kristina Borzutzki von NEXT ENERGY für Laserstrukturierungen.
- Tim Möller und Ulrike Kochan von NEXT ENERGY für UV-VIS, Profilometer, Ellipsometer und EQE Messungen.
- Dr. Stefan Geißendörfer und Volker Steenhoff von NEXT ENERGY für intensive Diskussionen und Beratungen zur Simulation.

- Alex Neumüller von NEXT ENERGY für die Bereitstellung seiner Ergebnisse zur Entwicklung der p-Schicht mit N_2O.
- Dr. Karsten von Maydell, Volker Steenhoff, Nies Reininghaus, Alex Neumüller, Dr. Ben Hanke und Dr. Peter Klement von NEXT ENERGY für das Korrekturlesen der Arbeit.
- Anna Winkelmann von der Universität Oldenburg für die sprachliche Korrektur der Arbeit.
- dem gesamten Team von NEXT ENERGY, die meine Promotionszeit nicht nur durch wertvolle Diskussionen, sondern auch durch ihre Liebenswürdigkeit und Freundschaft bereichert haben!
- meiner Familie und meiner WG für das fürsorgliche Dasein und Zuhören sowie für ihre Unterstützung während meiner gesamten Studienzeit!

List of Publications

Printed Publications

Related to this Work:

1) C. Walder, A. Neumüller, O. Sergeev, M. Kellermann, K. von Maydell, C. Agert. *Amorphous silicon oxinitride in silicon thin-film solar cells.* Energy Procedia **44**, 203-208 (2014)

2) C. Walder, M. Kellermann, E. Wendler, J. Rensberg, K. von Maydell, C. Agert. *Comparison of silicon oxide and silicon carbide absorber materials in silicon thin-film solar cells.* EPJ Photovoltaics **6**, 65302 (2015)

Other:

1) C. Walder, J. Lacombe, K. von Maydell, C. Agert. *Optical modeling of thin film silicon solar cells by combination of the Transfer-Matrix-Method and the Raytracer algorithm.* Proceedings of the SPIE Photonics Europe 2012 in Brussels, 84290K (2012)

2) C. Walder, J. Lacombe, K. von Maydell, C. Agert. *Optical modeling of thin-film silicon solar cells by combination of the transfer-matrix method and the raytracer algorithm.* Optical Engineering **51**(7), 073801 (2012)

3) S. Geissendoerfer, C. Walder, O. Sergeev, K. von Maydell, C. Agert. *Simulation of single-junction thin-film silicon solar cells with varying intrinsic layer thickness.* Proceedings of the Photovoltaic Specialists Conference (PVSC), 38th IEEE in Austin, 367-370 (2012)

Conference Contributions

Related to this Work:

1) C. Walder, A. Neumüller, O. Sergeev, M. Kellermann, K. von Maydell, C. Agert. *Amorphous silicon oxinitride in silicon thin-film solar cells.* **Poster**, EMRS Spring Meeting, Strasbourg, France (2013)

2) C. Walder, M. Kellermann, E. Wendler, J. Rensberg, K. von Maydell, C. Agert. *Comparison of silicon oxide and silicon carbide absorber materials in silicon thin-film solar cells.* **Poster and Flash Talk**, Photovoltaic Technical Conference (PVTC), Aix en Provence, France (2014)

Other:

1) C. Walder, J. Lacombe, K. von Maydell, C. Agert. *Semi-coherent optical modelling of thin film silicon solar cells.* **Poster**, DPG Frühjahrstagung, Dresden, Germany (2011)

2) C. Walder, J. Lacombe, K. von Maydell, C. Agert. *Efficient optical modelling of silicon thin-film solar cells - Combination of Transfer-Matrix-Method and Raytracer based on the integral haze.* **Poster**, International Workshop on Modeling of Thin-Film Silicon Solar Cells, NEXT ENERGY, Oldenburg, Germany (2012)

3) C. Walder, J. Lacombe, K. von Maydell, C. Agert. *Optical Modeling of Thin-Film Silicon Solar Cells by Combination of the Transfer-Matrix-Method and the Raytracer Algorithm.* **Talk**, SPIE Photonics Europe, Brussels, Belgium (2012)

Curriculum Vitae

Cordula Walder (Physicist)

Personal Information

Date of Birth	03/07/1986
Place of Birth	Vechta
Denomination	Roman Catholic
Nationality	German
Civil Status	Single

Education

11/2011 - 11/2015	**Doctoral Studies in Physics** Carl von Ossietzky Universität Oldenburg Doctoral Thesis: *Development of a High Voltage Top Cell for Silicon Thin-Film Solar Cells.* NEXT ENERGY · EWE Research Centre for Energy Technology at the University of Oldenburg
10/2009 - 11/2011	**Master of Science in Physics (Grade: 1.07)** Carl von Ossietzky Universität Oldenburg Master Thesis: *Effiziente optische Simulation von Silizium-Dünnschichtsolarzellen. Kombination von Transfer-Matrix-Methode und Strahlverfolgungsalgorithmus basierend auf dem integralen Haze.* NEXT ENERGY · EWE Research Centre for Energy Technology at the University of Oldenburg
10/2006 - 09/2009	**Bachelor of Science in Physics (Grade: 1.24)** University of Bremen Bachelor Thesis: *Zeitabhängige Störungen eines Zwei-Niveau-Systems.* Institute of Theoretical Physics at the University of Bremen
1997 - 2006	Secondary School: Liebfrauenschule Vechta Abitur (Grade: 1.0)
1993 - 1997	Primary School: Overbergschule Vechta

Internships, Student Assistant Jobs and Lecturing

10/2013 - 02/2014	Tutor for the Advanced Lab in Physics B.Sc. at the Carl von Ossietzky Universität Oldenburg
05/2012 - 01/2013	Tutor for the Solar Cell Lab of the International *Postgraduate Programme Renewable Energy* at the Carl von Ossietzky Universität Oldenburg
10/2010 - 10/2011	Student Assistant at NEXT ENERGY · EWE Research Centre for Energy Technology at the University of Oldenburg
09-10/2008	Internship at the DLR National Aeronautics and Space Research Centre of the Federal Republic of Germany in Bremen

International Experience

08/2003-12/2003	Student Exchange at Regina High School, Cleveland, USA

General Skills

Languages	English (Business Fluent), French (Good), Spanish (Basic)
Software Skills	MS Office, Latex, Origin, Matlab, Fortran, Java, TCL, Sentaurus TCAD
Driving Licence	Class B in Germany
Hobbies	Wing Tsun (Martial Arts), Piano, Guitar, Choir, Dancing, Jogging